Master of Science Thesis

Enhancing the mechanical properties of fused filament fabricated parts by elevating the print room temperature

D. van Veen BSc

Faculty of Mechanical, Maritime & Materials Engineering · Delft University of Technology

TU Delft Delft University of Technology

TNO innovation for life

Challenge the future

Enhancing the mechanical properties of fused filament fabricated parts by elevating the print room temperature

Master of Science Thesis

For obtaining the degree of Master of Science in Materials Science & Engineering at Delft University of Technology

D. van Veen BSc

May 24, 2019

Faculty of Mechanical, Maritime & Materials Engineering · Delft University of Technology

An electronic version of this dissertation is available at
http://repository.tudelft.nl/.

Delft University of Technology
Department of
Materials Science & Engineering

The undersigned hereby certify that they have read and recommend to the Faculty of Mechanical, Maritime and Materials Engineering for acceptence a thesis entitled "**Enhancing the mechanical properties of fused filament fabricated parts by elevating the print room temperature**" by **D. van Veen BSc** in partial fulfillment of the requirements for the degree of **Master of Science**.

Dated: May 24, 2019

Committee:

Prof. dr. I.M. Richardson

Dr. I. Fernandez Villegas

M.A. Bessa Phd

J. Berens MSc

Abstract

Additive manufacturing (AM) is currently making a transition from mainly being used for prototyping to an alternative for conventional production methods. AM provides more freedom in design geometry combined with the possibility to produce (complex) products in low quantities. As a result, the need arises for printed parts with consistent mechanical properties that rival those of conventionally produced parts. Currently, the layer-by-layer process used by AM introduces weaknesses at the interlayer (weld) bonds. Polymer science suggests that raising weld bonds to temperatures above the glass transition temperature (T_g) can improve their mechanical properties up to bulk strength.

This research aims to verify if fused filament fabrication (FFF) printing at elevated print room temperatures (T_{env}) raises interlayer temperatures above T_g and as a result enhances mechanical properties. In order to measure the increase in interlayer properties double cantilevered beam (DCB) testing is used. Additionally, tensile testing is used to evaluate the effect of elevating T_{env} on general mechanical properties.

DCB and tensile testing of samples printed at elevated T_{env} values has shown an increase of 109 % in interlayer energy release rate (G_{1c}), up to 50 % in ultimate tensile strength and 106 % in tensile toughness. This has been determined by comparing samples printed at elevated T_{env} with samples printed at room temperature (23 °C). To further understand the mechanisms behind the enhanced properties, the temperature history during printing has been determined. This has been done by running simulations and using IR imaging. The temperature history of printed parts has been related to data obtained from mechanical testing. This showed that mechanical properties increased for samples in which the interlayer bonds resided above T_g for prolonged periods of time.

In addition, optical microscopy and micro CT has been used to monitor the meso-structure of printed samples. This showed that voids in the sample caused by printing defects contributed to an increased spread in measured values. Mechanical properties corrected for effective surface areas showed a roughly 10 % increase for average values. While significant this is not in the same order of magnitude as the increase in mechanical values reported for printing at higher T_{env} values. Combining these results it has been found that elevating T_{env} does not significantly affect the meso-structure, but it does cause bonds to spend an increased amount of time above T_g. Therefore, it has been concluded that the enhanced mechanical properties are caused by weld bond healing due to the part residing above T_g.

Keywords: AM, FFF, thermoplastic, 3D-printing, entanglements, reptation time, glass transition temperature, polymer welding, interlayer bonding, energy release rate, DCB, tensile testing, PETG, micro CT, infrared, Digimat AM

Acknowledgements

First of all I would like to thank my supervisor at TNO Julius Berens for introducing me to the topic of Additive Manufacturing, the many fun discussions both on and off topic and for bringing me along on many interesting meetings both at TNO and other companies. I would also like to express my gratitude towards Julius, Ian Richardson, Irene Fernandez Villegas and Miguel Bessa for providing me with valuable feedback on my research.

I would also like to thank Luuk Lubbers, Hugo Dijkers, Frederic Creusen, Amber van Hauwermeiren and other members of the 3D-printing team for the many fun discussions both on and off topic. This helped to make every day at TNO a pleasure.

Many thanks also to all the other colleagues at the EBP, EM and BMC departments for the discussions on *a.o.* 3D-printing, polymer science and fracture mechanics. Additionally I would like to thank Elise Reinton and Ton Riemslag for the valuable advice and help regarding the mechanical testing.

Finally I would like to thank my parents, brother, friends and roommates for putting up with my endless talk on 3D-printing and the intricate workings of thermoplastic polymers. A special thanks goes out to my girlfriend Nicky who had to put up with this the most and still remained enthusiastic through it all.

To anyone I might have forgot, know that your contribution is still very much appreciated.

Rijswijk, The Netherlands — D. van Veen BSc
May 24, 2019

List of Figures

List of Tables

Contents

Nomenclature

List of abbreviations

ABS	Acrylonitrile Butadiene Styrene
AM	Additive Manufacturing
ASTM	American Society for Testing and Materials
CAD	Computer Aided Design
CT	Computed Tomography
DCB	Double Cantilever Beam
DSC	Differential Scanning Calorimetry
FDM	Fused Deposition Modeling
FEM	Finite Element Method
FFF	Fused Filament Fabrication
FRP	Fiber Reinforced Polymer
IR	Infrared
ISO	International Organization for Standardisation
MBT	Modified Beam Theory
MoD	Ministry of Defense
PA	Polyamide
PETG	Polyethylene Terephtalate Glycol modified
PLA	Polylactic Acid
RVE	Representative Volume Element
SENB	Single Edge Notch Bend
SLM	Selective Laser Melting
SLS	Selective Laser Sintering
STL	Standard Triangle Language

TNO	Nederlandse Organisatie voor Toegepast Natuurwetenschappelijk Onderzoek, Netherlands Organisation for Applied Scientific Research
TP	Thermoplastic
TS	Thermoset
UD	Unidirectional
UHMWPE	Ultra High Molecular Weight Polyethylene
UTS	Ultimate Tensile Strength

List of symbols

α	Linear expansion coefficient $[1/K]$
Δ	Additional crack length $[m]$
δ	Stretch between atoms $[m]$
δ	Vertical displacement of beam in bending $[m]$
η	Effective surface area percentage [-]
γ	Interfacial energy $[J/m^2]$
σ	Stress $[Pa]$
σ_u	Ultimate tensile stress $[Pa]$
σ_{th}	Theoretical maximum stress $[Pa]$
τ	time spent at a certain temperature above T_g divided by the respective reptation time [-]
θ	Tangent of vertical displacement and beam length [-]
a	Interatomic distance $[m]$
a	beam length $[m]$
a	crack half-length $[m]$
a_0	Initial interatomic distance $[m]$
A_1	Factor for reaction frequency [-]
B	constant characterizing hole size succesfull chain movement [-]
b	Beam width $[m]$
C	Compliance $[1/Pa]$
E	elasticity modulus $[Pa]$
F	Force acting on atomic bond $[N]$
f	Fractional free volume [-]

f(a/w)	geometry dependend dimensionless quantity [-]
f_g	Fractional free volume at T_g [-]
F_{max}	Load for atomic bond breaking $[N]$
G	Energy release rate $[J/m^2]$
G_{1c}	Critical mode 1 energy release rate $[J/m^2]$
I	Second moment of area of beam cross section $[m^4]$
K_{1c}	Stress intensity factor $[Pa\sqrt{m}]$
L_p	Top printed layer
L_{p-n}	n^{th} previous printed interlayer
L_{p-n}	n^{th} previous printed layer
M	Bending moment on beam $[Nm]$
M_m	Molar mass $[g/mol]$
M_p	Generic mechanical property [-]
N	Number of chain segments [-]
P	Load $[N]$
R	Resistance against crack growth $[J/m^2]$
R_e	End-to-end distance [Å]
S	Stiffness of an atomic bond $[N/m]$
T_g	Glass transition temperature $[°C]$
T_m	Melt temperature $[°C]$
T_{part}	Part temperature $[°C]$
t_{rep}	reptation time $[s]$
t_{weld}	weld time $[s]$
U_{cr}	Energy available for crack propagation $[J]$
U_{el}	Elastic energy $[J]$
U_T	Tensile toughness $[J/m^3]$
W_{p-1}	Top printed interlayer
X	Interpenetration depth $[m]$

Chapter 1

Introduction

Over the past few years the Dutch Ministry of Defence (MoD) has expressed an interest in Additive Manufacturing (AM) and have asked TNO to conduct research in this area. The research TNO conducts into AM can be roughly divided into two areas. Firstly, the 3D-printing of spare parts with the ambition of expanding this to printing complete end products. Secondly, the 3D-printing of energetic materials [30]. Improving and more clearly defining the mechanical properties of AM parts, is expected to allow for a future in which using AM for functional and critical load bearing components can become more common.

The focus of this report lies on an experimental set up with the goal of improving the interlayer adhesion in 3D-printed parts made using Fused Filament Fabrication (FFF). In order to achieve this, samples are printed in a printer with elevated print room temperature temperatures. This is expected to raise the temperature in top layers above the material's glass transition temperature (T_g) during printing. This is based in part on previous research by van Veen *et al.* [20][94] which suggests that 3D-printed parts with lower glass transition temperatures (T_g) show better interlayer mechanical properties.

By keeping interlayer bonds at this elevated temperature, a change in the microstructure of the polymers is expected to lead to improved bonding between the layers. Printed parts commonly fail in between printed layers [28][79]. Therefore, improving interlayer adhesion is expected to lead to improved mechanical properties of the printed samples. This leads to formulation of the following hypothesis: "FFF printing at elevated print room temperatures increases mechanical properties due to interlayer surfaces residing above T_g for longer periods of time."

Currently high end printers often have enclosed printing chambers, sometimes with controlled chamber temperatures. However, this is mostly done in order to prevent warping of parts due to residual stresses. These are caused by the large temperature gradients throughout parts during printing. If the method proposed in this research proves to be effective in improving the mechanical properties of FFF parts, it can be implemented in these machines with relative ease.

This report starts with an overview in chapter 2 of the AM production methods currently used. The FFF process, which is the 3D-printing method used during this research is discussed in detail. Additionally a brief overview is given of possible safety concerns related to the, FFF, 3D-printing process.

Secondly a literature review is presented in chapter 3, which discusses both the fundamental polymer science based upon which the hypothesis was formulated and relates this to FFF.

Additionally previous research into the effects of temperature related parameters in the production of AM specimens and annealing of printed samples is discussed. The literature study also elaborates on previous research into the testing of interlayer strength of FFF produced specimens.

In chapter 4 the hypothesis and research questions are presented which are at the center of this report.

In chapter 5 the testing methods are described. This starts with the materials used for printing, continues with a description of the test methods and test samples used and subsequently elaborates on the production of the test samples. This is discussed both for double cantilevered beam (DCB) samples and tensile samples. DCB samples are used to determine the degree of interlayer bonding of the 3D-printed parts. The tensile test sample serve as a sanity check for this testing method and are used to quickly determine a number of other relevant mechanical properties. Additionally the methods used for analyzing the test samples are discussed. This chapter concludes with a test matrix which indicates the number of samples tested and the conditions under which they are produced.

Chapter 6 contains the results obtained during this research. Along with data obtained from the DCB and tensile tests, results obtained from differential scanning calorimetry (DSC), optical microscopy, micro computed tomography (CT), FEM temperature simulations and infrared imaging (IR) are presented. These results are discussed and related to each other and theory discussed in chapter 3.

Finally a conclusion and recommendations for further research are presented.

Chapter 2

The Additive Manufacturing Process

This chapter contains the fundamentals of AM production methods with a strong emphasis on FFF. Also a short section is devoted to the possible safety aspects associated with 3D-printing.

2.1 Additive Manufacturing Techniques

In the following section the working principles of 3D-printing processes are described. Subsequently, information is presented on on a variety of 3D-printers available. Finally, the Fused Filament Fabrication method (FFF), is elaborated upon. This is the AM method used throughout this report.

2.1.1 An introduction to 3D-printing processes

3D-printing, also referred to as AM, is the collective name for manufacturing technologies based on the following principles [19]: Firstly a 3D file is needed which can be made with either a Computer Aided Design (CAD) program or 3D scanning technology. This file is then converted into a format that can be used in the printing preparation stage. This can *e.g.* be a Standard Triangle Language (STL) file which describes the object using triangles (or polygons). This file is loaded into slicer software which converts the geometry into a set of printing parameters the printer understands. This slicer software divides the 3D geometry into layers. The operator decides the settings for printing parameters such as infill shape and percentage, the number of wall-, roof- and floor layers of the part and many more [19]. The software then converts this information into a command language which enables the printer to make parts. An example of such a command language is G-code, which is commonly used in most extrusion based printers. This code contains data such as x, y and z coordinates as well as accelerations and temperatures.

2.1.2 AM methods currently available

In this paragraph the most commonly used 3D-printing methods are mentioned and briefly explained. This serves to give the reader an impression of current options available with AM and provide a frame of reference. A more detailed explanation is presented for the FFF printing method. This is the 3D-printing method used during this research.

Firstly, there are two powder bed fusion methods; selective laser sintering (SLS) and selective laser melting (SLM) [8][19]. SLS is used mostly for polymers, SLM is generally used for metals. After a thin layer of powder is deposited, a laser is used to locally heat up the material. This way it is either melted or sintered to the material in the layer below. This process is repeated layer by layer, in order to achieve a 3D structure. Generally speaking sintering requires a lower temperature than melting and has a different effect on the material, still these methods are generally considered to be relatively similar. TWith a tolerance of $\pm 0,3$ mm for SLS and $\pm 0,1$ mm for SLM [19] these methods give relatively accurate results. An additional benefit for SLS of polymers is the fact that no support structures are needed.

In Vat-polymerization, which is a type of stereo lithography, a UV-light source is used to solidify a resin material [8][19]. Subsequently, similar to most 3D-printing methods, the bed is is then moved vertically, after which the process is repeated. This method generally gives a very smooth surface roughness. A downside is that mechanical properties of parts printed with this method tend decrease when exposed to sunlight [19].

Material Jetting also uses exposure of light to cure material. However in this case the material is jetted upon a build plate in the form of droplets [8][19]. This method allows for the combination of many different material types in a single print. This facilitates *e.g.* the printing of *e.g.* support structures that can be dissolved and multicolor prints. While this method is accurate, with a layer height of $0,1$ mm and no warping (a concept explained in section 5.3.4) is achievable, the materials used is expensive and mechanical properties of resulting parts are relatively low [19].

2.1.3 The Fused Filament Fabrication method

Fused Filament Fabrication (FFF), also to as Fused Deposition Modeling (FDM), is currently the most widespread AM method. In this research the term FFF is used, as is the standard at TNO. This is done because FDM is a trademarked term introduced by Stratasys Inc. [4]. In FFF a spool of filament is fed into an extruder. This extruder is moved across the bed according to a pattern specified by G-code, see section 2.1.1, depositing material as it moves. This material is commonly a thermoplastic polymer as these can be reshaped and fused with addition of heat [19][82]. The deposited lines are referred to as roads throughout this report. Once a layer is completed, the print bed moves down and a new layer is deposited on the previous one. This process is illustrated in figure 2.1.

FFF is widespread mainly due to two reason. Firstly the filament material, and the printers themselves are inexpensive. Additionally, FFF printers are operated with relative ease. Also operating the printers is relatively simple. This leads to FFF being the preferred 3D-printing method for most consumers [19][95]. In industry it is often used for materials which need a short lead time or low production volume [4][19]. Additionally there is a large variety of materials that can be used in combination with FFF printers [9][19][69][95].

To give the reader an impression of some of the available thermoplastics used in FFF, figure 2.2 was made. In this figure information obtained from several sources is combined to provide a clear overview [9][19][95]. Some material types may require slight modifications of the printer. For example abrasive filaments are printed, a nozzle with high hardness may be required. For more extensive lists and the most recent additions the reader is advised to consult the following sources [69][95] as new materials are introduced on a frequent basis.

Using FFF parts presents some challenges that need to be considered when designing and printing these parts. For example, a signature feature of FFF is the strong an-isotropic nature

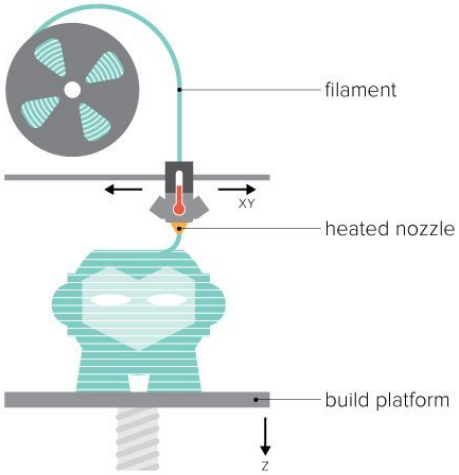

Figure 2.1: Illustration of the FFF printing process [8]

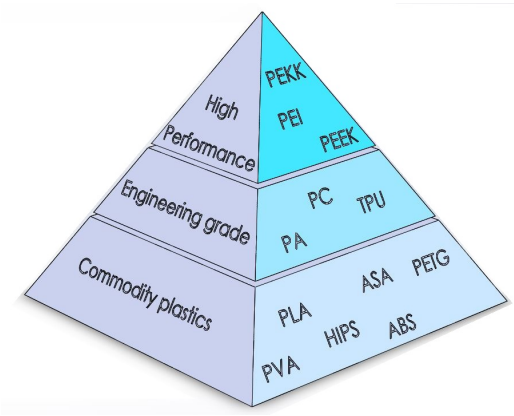

Figure 2.2: A selection of polymers used for 3D-printing, ranging from commonly used plastics up to high performance materials.[19][95][9].

of the properties of printed parts [28][66][86][79]. Designers of 3D-printed parts should consider this an-isotropic nature during the design process as well as when choosing the orientation of the part in the printing process. Additionally, FFF makes it possible to produce parts with an infill of less than 100 %, even going as low as 10% for parts that do not need structural strength or 0 % when only a shell is needed. It has been shown by Alvarez *et al.* [13] and Fernandez-Vicente *et al.* [34] to significantly influence the mechanical properties if a lower infill is chosen. Lower infill for example results in lower tensile strength and less impact resistance. It has also been shown that a higher density of the printed part generally results in improved mechanical properties [90]. However when lesser mechanical properties are acceptable and it is preferred to have a shorter printing time or achieve weight reduction, lower infill percentages may be an interesting option.

It should be added that these properties can actually be viewed as an additional feature instead of simply a trade off between production speed and mechanical properties. Because of how 3D-printing works, it is possible to make parts with intricate interior designs. This gives additional possibilities which are not as easily available with conventional production methods. Examples can be found for example in the field of meta-materials [77][41]. The possibility

of printing hollow structures also allows for alternatives such as filling these parts with other materials which may, for example, exhibit better mechanical properties but are not as easily printable (*i.e.* epoxy's) [18] or using them as molds [43][17]. However, as this topic is beyond the scope of this research it is not discussed further.

Currently the previously mentioned an-isotropic nature of the parts is the main limitation of FFF. Especially as mechanical properties are shown to decrease in certain directions with respect to bulk material properties [66][86]. This is mainly caused by the material being oriented in the printing direction and the fact that the adhesion between layers is not as strong as mechanical properties in the filament itself [28][79]. The FFF process can be seen as a large number of welds stacked on top of each other [85]. In order to achieve a healed weld bond, *i.e.* with good layer adhesion which shows material properties similar to bulk material, it is necessary to control the time-temperature history of the process [27][36][97]. The nature of this healed polymer weld bond and it's relation to layer adhesion in FFF is elaborated upon further in chapter 3, as it is the focal point of this research.

2.2 Safety aspects concerned with working with FFF

FFF and other AM production methods are new to industrial environments. As a result, not much research has yet been conducted regarding the safety aspects of this production method. In order to safely produce samples during this research, an effort has been made to find relevant information on safety concerning FFF (and FDM) processes. This is briefly discussed in this section. This information is used to take desired precautions.

During FFF production, depending on the thermoplastic polymer used, material can be heated to upwards of 450 °C. This can lead to pyrolysis of the material. Pyrolysis indicates possible formation of toxic gases. This has been described by Nielsen *et al.* [75] and Braun [21]. Research by Braun states that LC_{50} values of the thermal degradation products for polymers used in 3D printing range from 10.8 mgL^{-1} to 61.9 mgL^{-1} [21]. LC_{50} is the concentration at which 50 % of a population exposed to a specific toxin dies [78]. This value only gives information on acute toxicity and does not consider long term exposures. Values reported by Braun do not represent immediate health concerns. However, because long term effects are unknown, excessive exposure is not desirable.

When looking beyond the example of nylon and at FFF filament materials in general no consensus has yet been reached in the literature. However, it is generally accepted to be advisable to keep the 3D-printer in a well ventilated room [16][88]. This is mostly due to the measured release of ultrafine particles.

It should be noted that no direct relation between 3D-printing and toxicity has been found. However, it is advised to place printers in a well ventilated room and not spend more time than necessary in the same room as the printer while printing. If available it is recommended to to place the 3D-printer in a fume hood during printing.

Chapter 3

Literature review

In this chapter the relevant literature pertaining to this research is discussed. Firstly in section 3.1 the fundamental physics with regards to polymer science are discussed. This starts with discussing thermoplastic polymers in general. This is followed by how these polymers attain their mechanical properties and how this is relevant when considering a temperature based production method such as FFF. Subsequently, based upon the polymer science described thus far and additional literature, a comparison between polymer welding and FFF is made. Section 3.2 deals with the notion that full healing of this interface does not directly mean that the AM part has mechanical properties that are equal to conventional production methods. Section 3.3 discusses previous research into the effects of heat on 3D-printed objects. This is followed by reviewing a testing method previously used for quantifying the interlayer bond strength in section 3.4. Finally a summary of this literature study is provided in section 3.5.

3.1 Fundamental polymer science

This section elaborates on the fundamental physics that form the foundation of this research. Firstly the principles of how polymers attain mechanical strength are discussed. In the case of FFF the most prevalent mechanism is that of entanglements [82][83], which is described in detail further on in this section. This can be understood by comparing FFF to polymer welding processes [27][32][36][97]. To put this in context, this section first deals with the concept of entanglements in combination with time-temperature related parameters in polymer welding. This is followed by describing the relationship between polymer welding and FFF in more detail. Additionally, difficulties related to achieving fully healed weld bonds in FFF are described. The principles described in this section are used as a basis for the hypothesis and research methodology described in chapter 4.

3.1.1 Amorphous and semi-crystalline microstructures

Polymer literally translates to "many parts" [83], which refers to the way this material is build up on a microstructure level. Polymers consist of long molecule chains build up from repeating smaller parts (called monomers, or "one part"). The amount of monomers present in a polymer molecule is called the degree of polymerization which directly relates to it's molar mass (M_m) [54][83]. Both the chemical nature of the monomers and the degree of polymerization contribute significantly to the properties of the resulting polymer.

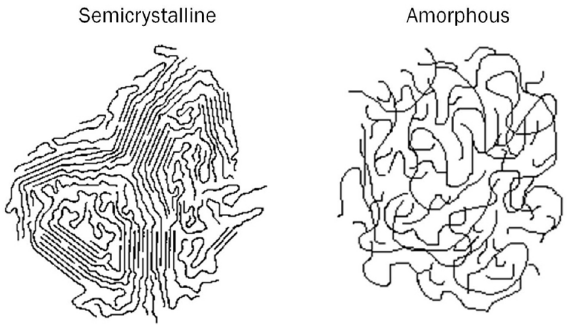

Figure 3.1: Schematic representation of a semi-crystalline and amorphous microstructure for polymers [54].

Many types of polymers exist and they exhibit different kinds of behavior under load and thus different mechanical properties [82]. For this research the focus is on thermoplastic (TP) polymer solids. As mentioned in section 2.1.3 TP polymers are the main material type used in FFF printing. Polymer solids are obtained by cooling a polymer melt below it's melting temperature (T_m). Polymer solids can exhibit a multiphase nature in which they consist of both crystalline regions and amorphous regions. Crystalline regions are also called spherulites or lamellae [82][83] as the sections of chains within these regions are packed parallel to each other. The amorphous regions exist in between these crystalline regions and are by definition unstructured bunches of polymer chains [54][83]. The resulting material is called semi-crystalline. A schematic representation of this microstructure is included in figure 3.1.

Besides the semi-crystalline structure, figure 3.1 also shows a fully amorphous polymer microstructure. In amorphous polymers the molecule chains are structured such that no crystal lamellae can be formed. Thus an amorphous structure is obtained. This can be both due to the size of polymer molecules as well as the chemical nature of the monomers. In most cases it can be stated that a polymer is neither fully crystalline or amorphous. Therefore it needs to be mentioned that there is no clear point at which a polymer goes from amorphous to semi-crystalline. Polymers labelled as amorphous might still contain a certain percentage of lammellae and a polymer labelled semi-crystalline can still have a degree of crystallinity within a wide range.

Commonly the distinction is made that amorphous polymers do not display a real T_m but only a glass transition temperature (T_g). Above T_g a material generally becomes tougher and more deformable [82]. The reason for this is that above this threshold the polymer chains get more room to move around. As a result molecular chains become more mobile [96], a process described in more detail further on in this section. This mobility causes a sharp decline in modulus (as chains suddenly move with relative ease with respect to one another). semi-crystalline materials instead show a more steady decline in modulus with increasing temperature above T_g [54]. Following this several methods can be defined to determine the type of microstructure of a thermoplastic polymer. Two of which are described here; a measurement showing the modulus as a function of temperature and Differential Scanning Calorimetry (DSC).

Measuring the modulus as a function of temperature [54] results in figures such as can be seen in figure 3.2. As described above, the amorphous polymer shows a sharp decline (at roughly $120°C$). The semi-crystalline shows an initial drop at T_g followed by a steady decline in modulus up to T_m at which a second drop in modulus can be observed. DSC measurements can be used to determine if, and at which temperature, the material shows a T_g and/or T_m [54][92]. As this is the method used this research it is described in more detail.

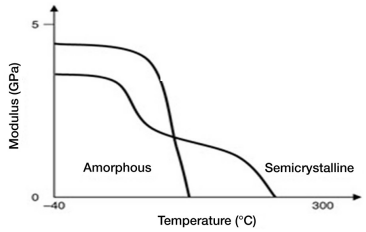

Figure 3.2: Schematic representation of a modulus versus temperature plot for a semi-crystalline and amorphous polymer [54].

In DSC the temperature of a sample is raised at a constant rate and the amount of energy needed to maintain this rate is monitored very precisely. A Schematic representation of a DSC is shown in figure 3.3. The energy needed to maintain the temperature rate is measured as a difference between a sample of the material of interest and a reference sample [31]. At a phase change a sudden change in the energy input is required, which occurs at certain temperatures (or over certain temperature ranges). The reason for this phenomenon is the release of energy (exothermic) or a need for extra energy (endothermic) to maintain the prescribed rate [31].

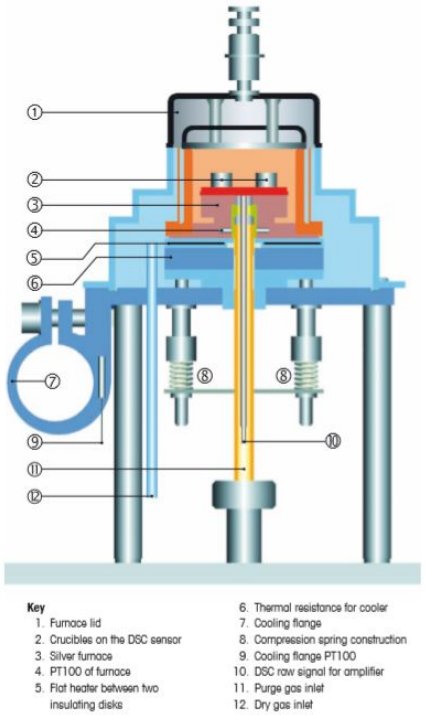

Figure 3.3: Schematic visualization of a DSC such as used for the measurement of T_g in this research [31].

A schematic representation of a DSC curve for a generic TP material is shown in figure 3.4. This shows how to recognize three phase transitions commonly found in TP materials. Firstly a slightly endothermic process can be seen as S-shaped drop in heat flow, indicating a transition to a more loosely organised phase. This commonly indicates the T_g [1][92][7][92]. Moving further to the right a positive peak can be seen which means an exothermic process takes place. This often indicates crystallization of the TP material [1][7][92] as the polymer chains align in crystalline structures [83] leading to a situation with lower internal energy.

Polymer crystallization that takes place upon heating a material between T_g and T_m is often reffered to as cold crystallization [92][80]. Crystallization can also occur when cooling a polymer from the melt, a process sometimes referred to as hot crystallization [80]. Finally a negative peak (or well) can be seen indicating an endothermic phase transition. Such a negative peak is associated with the TP material melting [1][7][92]. Combining the data obtained from the DSC with expertise and prior knowledge about the material these phase change temperatures can be specified to be *e.g.* T_g and T_m.

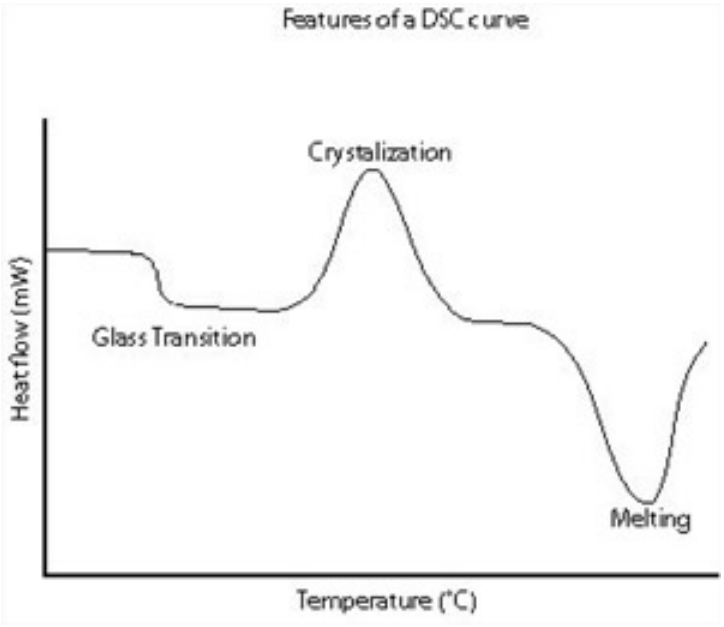

Figure 3.4: Schematic representation of DSC curve for a generic thermoplastic material showing how to recognize three important parameters. [1]

3.1.2 Entanglements in polymer materials

Polymers mainly get their strength from two different mechanisms. These mechanisms are cross-links and entanglements [82][83]. After a brief review of the concept of cross-links an in depth review is presented on the concept of entanglements. This section serves to explain why entanglements are of interest when considering the thermoplastic materials generally used in FFF. It also introduces the mechanisms on a microstructure level concerned with increasing mechanical properties in FFF parts. These are of importance concerning the methods used in this research with the goal of enhancing layer adhesion in FFF produced samples.

Cross-links is the name for covalent bonds between molecule chains in a polymer. In order for the polymer to deform, these covalent bonds now have to be broken. This generally increases mechanical properties, but limits options for reshaping the material once it is formed. Recycling polymers containing cross-links generally requires requires chemical processing [82][83]. As a result, recycling becomes more time, energy and money consuming and thus less viable. Generally, this is viewed as a downside of these types of materials [50][82]. When relating this property to 3D-printing, it limits the available AM methods (see section 2.1.2). Typically polymers in which cross-links are the dominant form of strengthening are called thermosets (TS) [82].

Entanglement are topological constraints a polymer chain can impose on another polymer

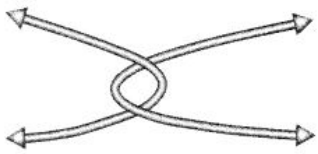

Figure 3.5: Visualization of two chains forming a topological constraint known as an entanglement [83].

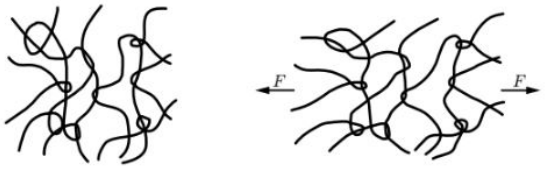

Figure 3.6: Visualization of Polymer chains with entanglements straightening under an imposed load [82].

chain [82]. This occurs because two molecule chains cannot pass through one other. Figure 3.5 shows a schematic representation of such a topological constraint. These entanglements add to the mechanical properties of polymers and are an important aspect when considering the mechanical behavior of polymers [82]. The previously described temperature dependence of molecule chain behavior leads to polymers responding differently to loads at different temperatures. Depending on the temperature the failure mode of an amorphous TP polymer is either dominated by Van der Waals forces between the chains or the covalent bonds between monomers [22][23][82].

As polymer chains can become very long this makes it improbable that they all end up arranged in a perfectly regular parallel structure. It has been mentioned in section 3.1.1 this makes it so that a polymer being fully crystalline is highly unlikely. Statistically, it is far more likely that molecule chains are twisted and entangled with other molecules [82], leading to the amorphous structure as mentioned in section 3.1.1. This results in an, amorphous, polymer containing many such entanglements.

The degree to which a polymer shows semi-crystalline or amorphous behavior can be modified by adding different side groups. Generally side groups raise the so called glass transition temperature (T_g) of a material. This temperature specifies the temperature at which molecule chains have enough room to slide past each other. Additionally the type of side group can either make a material more likely to stay amorphous or form crystalline structures [82].

In the case of loads imposed on a polymer at low temperatures (*i.e.* below T_g), Van der Waals forces are relatively high and chains cannot slip past one another [23][82]. The high friction forces required for the chains to slip past one another lead to the covalent bonds within a chain being loaded. If stresses in these covalent bonds are sufficiently high the bonds in between monomers can break resulting in brittle failure of the material [23][82]. An extreme case of mainly loading the covalent bonds in polymer chains can be seen in the case of highly oriented polymers such as Ultra High Molecular Weight Polyethylene (UHMWPE) fibers which as a result show high Young's moduli and tensile strength [24]).

Commonly at higher temperatures Van der Waals forces are not as strong allowing the molecular chains more room to move around [22][23]. After a load is placed on a TP polymer, the molecular chains are straightened between entanglement points as seen in figure 3.6 [82][83]. At higher temperatures chains can now slip along one another. The molecular chains, if given sufficient time or kept at sufficiently high temperatures, can slip out of the entanglements leading to disentanglement and resulting in local plastic deformation [23][82]. For most thermoplastic polymers this process first starts to occur at roughly 75% to 80% of the T_g and becomes increasingly easy for higher temperatures [23][82].

At T_g the free space within a polymer increases and molecule chains become more mobile [82][96], which makes it easier for the molecular chains to move. The mechanism leading to this behavior is described in section 3.1.3. A molecular chain constrained by entanglements

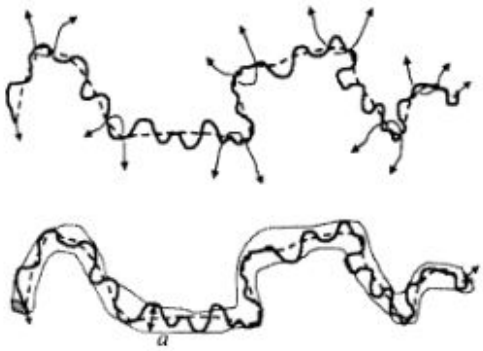

Figure 3.7: The movement of a polymer chain constrained by entanglements modelled as a tube [83].

can be modeled as a tube. This is presented in figure 3.7. This tube model was first suggested by Edwards [32]. Using this model the constraining effects on a chain can be modeled. The movement of the molecular chain through this tube is easier at higher temperatures. For thermoplastic polymers, which are visco-elastic materials [82][83], temperature and time are related to each other as is discussed further in section 3.1.3.

This relation results in similar behavior being observed when considering different time scales at one temperature and considering different temperatures at a single time scale. As a result the disentanglement described in this section for elevated temperatures may also occur when a consistent load is imposed on a polymer for prolonged time, a phenomenon known as creep [82][83]. This research focuses on the behavior of material at different temperatures therefore the time scale for loading conditions is considered constant. The effect of loading a polymer for prolonged periods of time is beyond the scope of this research.

3.1.3 Entanglements in polymer welding

Entanglements are the strengthening phenomena which dominate the welding of (TP) polymers [36][97]. In order for polymer parts to form a proper weld bond, it is necessary to regain a new equilibrium situation equal to the bulk properties at the interface[97]. Whether this is achieved depends on the degree of re-entanglement.

Wool *et al.* have extensively researched the strength of polymer interfaces in the context of weld bonds [97]. The strength of the interface has been considered in multiple stages; from initial tacking of the interfaces to a fully healed weld bond. This means from the stickiness upon initial contact up to the point where the material properties at the interface are equal to those in the bulk material. Wool focused mostly on symmetric interfaces of amorphous polymers. In this context the adjective symmetric is used to indicate the polymers are of the same chemical composition. Attention was paid to polymer welding in which the weld strength develops by surface rearrangement, wetting and diffusion of mobile molecules near the surfaces. This mobility is induced by introducing energy into the system, *e.g.* in the form of heat as was mentioned in section 3.1.2.

As previously described a polymer chain can be modelled to be confined to a tube which describes the topological constraints. Only the ends of the chain are free to move out of the tube through brownian motion [27]. Brownian motion is the name given to the stochastic irregular movement of a part suspended in a liquid due to collisions with other molecules [33][58]. As the chain ends move further and further away from the tube one could say it starts to forget

it's original position. Finally it will have fully "escaped" from the initial tube [36]. The time it takes for the polymer chains to fully move out of the original tube is called the reptation time (t_{rep}); this process is illustrated by figure 3.8. The concept of reptation was first introduced by Pierre-Gilles de Gennes who described it as *"a snake-like motion by which chains of monomers move in the melt"* [27]. This description gives a better feeling of how the molecular chains diffuse within the polymer system.

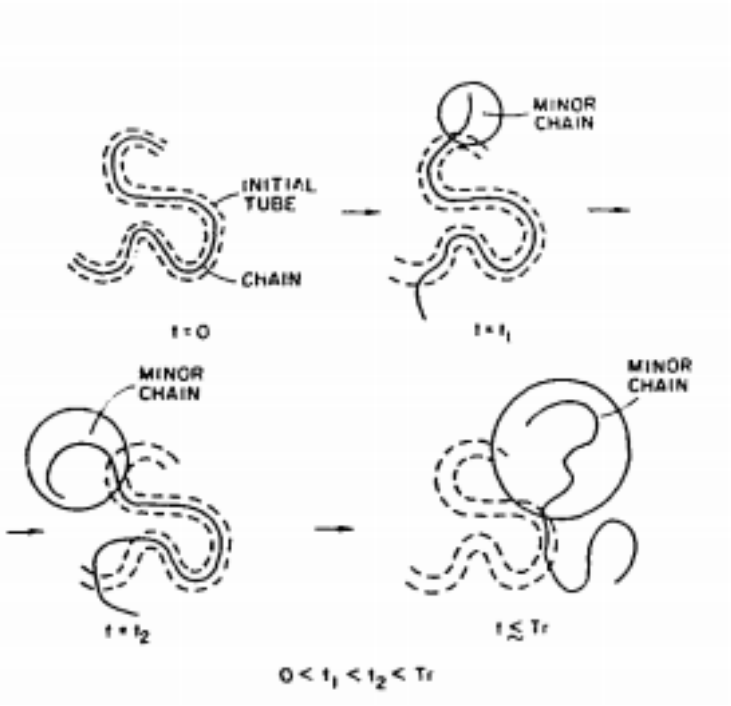

Figure 3.8: Visualization of a polymer moving out of it's initial entanglement tube through Brownian motion until eventually escaping it at it's reptation time [97].

Reptation is an important concept as it closely relates to the amount of healing that has occurred after a certain amount of time. Wool [97] and Anderson [14] state that reptation time is equal to the welding time as is shown in equation 3.1. In this equation t_{rep} is the reptation time, R_e^2 is the end-to-end distance squared, D is the self diffusion coefficient and t_{weld} is the weld time

$$t_{rep} = \frac{R^2}{3\pi^2 D} = t_{weld}. \tag{3.1}$$

The end-to-end distance squared is a way to model a molecular chain, which is initially considered to be a random walk of monomers [83] resulting in $R_e^2 = 0$. Molecules however tend to repel one another [35][83]. By imposing a repulsion between monomers, the end-to-end distance will generally speaking increase. A stronger repulsion will lead to a "stiffer" polymer chain. This will increase the end-to-end distance, which in turn influences the behavior of the molecular chain with respect to entanglements. The self diffusion coefficient is a measure of how easily a material interpenetrates itself after two interfaces of the same material are placed in contact [42][83]. Considering a slab A and B of material with the same chemical composition the self diffusion coefficient would thus be a measure for how fast the concentration of A in B (and vice versa) would increase.

What needs to be considered is that Anderson *et al.* make certain assumptions in their

model which would indeed lead to the reptation time being equal to the welding time. These include assuming instantaneous and complete wetting. It has been mentioned by Wool that a minimum amount of pressure is required during polymer welding to ensure intimate contact and wetting of polymer surfaces [97] (although additional pressure did not further increase interface fracture energy). Anderson also mentions that including these factors can contribute to the actual time needed for achieving a fully healed weld zone being longer than would be expected by looking solely at the reptation time.

This relation between polymer welding and reptation time had already been mentioned by de Gennes [27]. De Gennes considers the work of Jud *et al.* on the fracture mechanics of crack healing and welding of polymers [57] and relates this to the reptation time. From this he concludes that the fracture energy release rate (G_{1c}) reaches a maximum plateau value ($G_{1c\infty}$) after a welding time equal to the reptation time. This can be illustrated in the form of equation 3.8 in which t is the time spend at at a temperature above T_g with a certain t_{rep}. Wool specifies the quantities specified in equation 3.2 through 3.8 to evaluate the degree of healing in a weld bond.

The validity of this equation can be understood by considering the work of Wool [97]. Wool describes similar relations for the the interpenetration depth of segments of the inter-diffusing chains, ultimate tensile strength of samples and stress intensity factor. These are interrelated and all subsequent relations, including the one described in equation 3.8, can be derived from the relation between weld time and interpenetration depth of chains. This is described in more detail in the work of de Gennes [27] and Wool [97]. For the sake of presenting a complete picture the resulting relations are shown in equations 3.2, in which X is the interpenetration depth, 3.4 where σ_u is the ultimate tensile strength, 3.6 where K_{1c} is the critical stress intensity factor and equation 3.8 where G_{1c} is the critical energy release rate. First the relation between weld time and interpenetration depth of chains is presented

$$X(t) = X_\infty \left(\frac{t}{t_{rep}} \right)^{1/4}. \tag{3.2}$$

As has been described in section 3.1.2, considering the stress a single chain experiences both chain pull out and chain fracture can lead to the weld failing. If a chain has further penetrated into an adjacent polymer interface disentanglement will cost more energy due to the friction exerted on the chain increasing. Thus a higher stress is necessary for the chain to pull out. If the strain energy imposed on a chain exceeds a critical value this will lead to the chain breaking. Depending on the chemical nature of the molecular chain it either disentangles or breaks. However, either way a certain maximum value is attained after the chain has diffused a significant amount. Wool [97] showed that

$$\sigma_u(X) = \sigma_{u\infty} \left(\frac{X}{X_\infty} \right). \tag{3.3}$$

Thus from equation 3.2 and 3.3 it follows that

$$\sigma_u(t) = \sigma_{u\infty} \left(\frac{t}{t_{rep}} \right)^{1/4}. \tag{3.4}$$

Considering the relation between stress intensity factor and stress imposed on a part as seen in equation 3.5 [55] where $f(a/w)$ is a geometry dependend dimensionless quantity and $2a$ is the crack length

$$K_c = f(a/w)\sigma\sqrt{2\pi a} \tag{3.5}$$

It follows from equation 3.4 and 3.5 that

$$K(t)_{1c} = K_{1c}\infty \left(\frac{t}{t_{rep}}\right)^{1/4}. \tag{3.6}$$

Likewise due to the relation between stress intensity factor and energy release rate as shown in equation 3.7 [55]

$$G_{1c} = \left(\frac{K_{1c}^2}{E}\right) \tag{3.7}$$

It follows that

$$G_{1c}(t) = G_{1c\infty} \left(\frac{t}{t_{rep}}\right)^{1/2}. \tag{3.8}$$

A trend can be seen in which mechanical properties are related to the time spent welding and reptation time at the specified welding temperature according to equation 3.9. In equation 3.9 general mechanical properties are indicated with $M_p(t)$

$$M_p(t) \sim \left(\frac{t}{t_{rep}}\right)^{1/n}. \tag{3.9}$$

That leaves the question of how this reptation of polymer chains leads to the healing of a polymer-polymer interface. This can be understood by considering figure 3.9 obtained from the work of Sun *et al.* on the effect of processing parameters on the bonding quality of FFF [89]. Figure 3.9 shows a section of two adjacent filament roads. As can be seen in this figure, initially there is a clear interface at which the surfaces of both roads touch. After both roads are pushed together it may seem, on a macroscopic scale, like they have joined. However when considering the molecular chains on a nano scale there is still a clear divide. Only after molecular diffusion has taken place will polymer chains have migrated from one road to the other. This diffusion occurs by reptation of the chains. After the reptation time each polymer chain has moved to a new fully random configuration [14][48][97]. As a result the chains at the interface have formed new entanglements with chains from both roads and a new equilibrium is reached. Once the material at the interface is indistinguishable from the bulk material full healing is achieved.

As previously mentioned it is necessary to introduce energy into the system in order for the chains to start moving and molecular diffusion to occur. In the context of this research this energy is introduced through heat. When looking back at equation 3.1 this energy component can be found in the diffusion coefficient D. The diffusion coefficient has been shown to vary with temperature [36][67]. Fleischer explains this temperature dependence by using polymer free volume theory [36] as introduced by Doolittle [29] and Fujita [40]. He does this by considering the tube model which has been described above. He models the reptation time t_{rep} as the time it takes for the center of mass of the chain to displace over the chain end-to-end distance (which is taken as the root of the mean square end-to-end distance $\sqrt{R_e^2}$, where R_e^2 is the dot product of the end-to-end vectors). Fleischer describes the self diffusion coefficient in equation 3.1 in terms of the influence of free volume on the mobility. This is illustrated in equation 3.10

$$D = A_1 exp\left(\frac{-B}{f(M,T)}\right) N^{-2}. \tag{3.10}$$

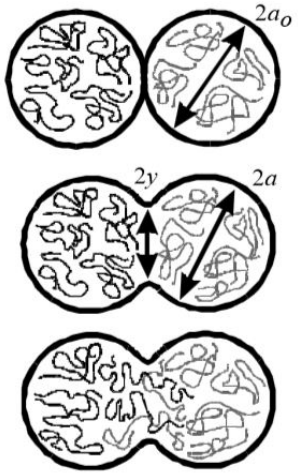

Figure 3.9: Visualization of reptation leading to healing of polymer-polymer interface [89]

In this equation D is the self diffusion coefficient; A_1 is an empiric pre-exponential factor describing the frequency at which reactions occur for a specific material-temperature combination; B is a constant characterizing the hole size needed for a successful movement of a chain segment; f is the fractional free volume as a function of the molar mass (M_m) and temperature (T); N is the number of segments in the chain. The fractional free volume is described by equation 3.11

$$f = f_g + \Delta\alpha(T - T_g(M_m)). \tag{3.11}$$

In equation 3.11, $f_g = 0.025$ is the fractional free volume at T_g. It has been shown that this number can be assumed to be the same for most polymers [96]. $\Delta\alpha$ is the linear expansion coefficient. When A_1 and B are assumed to be constant over small temperature intervals the scaling of the reptation time with temperature can be determined. Combining equations 3.1, 3.10 and 3.11 it is seen that t_{rep} scales with T according to equation 3.12.

$$t_{rep} \sim \frac{C_1}{exp\left(\frac{-B}{C_2 + \Delta\alpha T}\right)} = C_1 e^{\frac{B}{C_2 + \Delta\alpha T}}, \tag{3.12}$$

in which

$$C_1 = \frac{R^2}{3\pi^2 A_1 N^{-2}} \tag{3.13}$$

and

$$C_2 = f_g - \Delta\alpha T_g. \tag{3.14}$$

As seen in equation 3.11, T_g is related to the molar mass of the polymer chains. Equation 3.11 also shows that the free volume expands as temperatures rise above T_g. As a result the polymer chains can move more freely and molecular diffusion (by way of reptation) occurs more readily, leading to the reptation time decreasing. At this point it is interesting to note that polymers build from monomers with the same chemical compositions and thus the same name, *e.g.* Acrylonitrile Butadiene Styrene (ABS) or Polylactic Acid (PLA), can have a broad range of T_g values due to differences in molar masss.

In order to understand why the free volume has this effect on the reptation time it is

important to know what is meant with the free volume. In polymer science free volume is defined as the space in a polymer (solid or liquid) that is not occupied by polymer molecules [100]. For example, in a liquid there are relatively high amounts of free volume when compared to a solid. As a result molecules can rearrange more easily as there is more unoccupied space to which they can move. As stated the reptation time is a significant component of the time required for full healing of polymer welds. Thus it can be stated that predictions can be made about polymer weld time considering polymer interface temperature in relation to T_g. From equation 3.12 it is expected that the reptation time decreases exponentially with increasing temperature (from an onset at T_g) and bulk material properties are obtained faster.

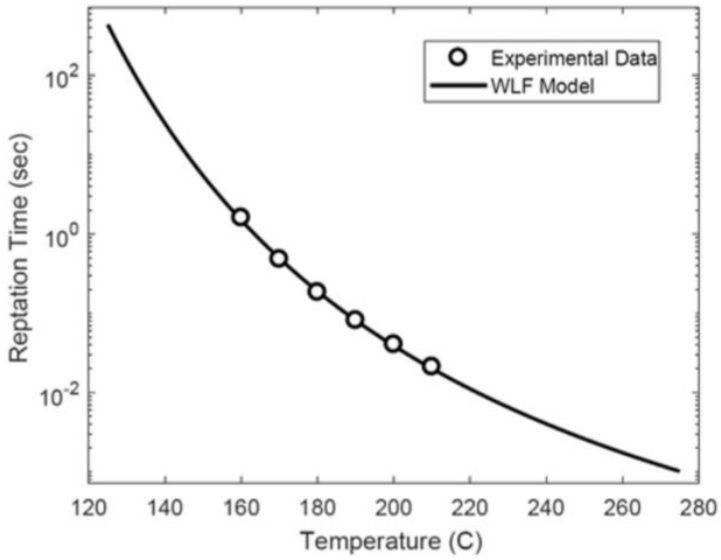

Figure 3.10: Graph showing the reptation time at specific temperatures for ABS as presented by Hart *et al.* [49]

Indeed this exponential decrease in reptation time with increasing temperature, offset by T_g, can be shown in a graph by plotting temperature against the respective reptation time. Such a graph can be made by first obtaining a master curve of the storage- and loss modulus of a specific polymer as a function of frequency at a reference temperature. By taking the inverse of the frequency at which the storage modulus first crosses the loss modulus the reptation time at this temperature can be determined [83]. This data is then combined with the shift factor of a material plotted against temperature, which can be obtained using the William-Landel-Ferry (or WLF) method [96]. This will provide a curve showing the reptation time for specific temperatures. An example of this for ABS is included in figure 3.10.

3.1.4 Polymer welding in FFF

The polymer welding concept can be related to FFF by considering the processes occurring during printing [71]. Each printing layer is in a semi molten (amorphous) phase and pressed slightly into the previous layer. As a result the previous layer, which generally speaking is not completely cooled down yet, is again heated up. This is illustrated in figure 3.11. This combination of heat and pressure results in a situation similar to polymer welding. As previously stated the interface between the layers is required to be above T_g in order for the polymer chains to diffuse [36][71] and a weld bond to be made. Seppala et al. measured the degree to which this occurs during the printing of ABS in an open FFF printer with a heated plate (set to 110

°C) using infrared thermography [85]. The results of these measurements are shown in figure 3.11.

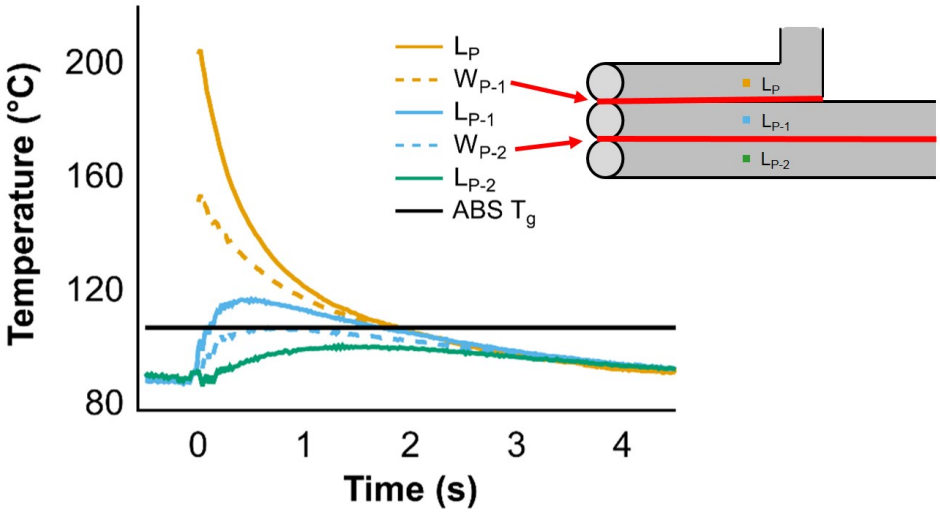

Figure 3.11: Graph showing the temperature-time distribution of sequential layers of printed polymer material (specifically ABS). L_p is the top layer, L_{p-1} the previous layer, $W_{P,P-1}$ the weld line between these layers etc. T_g is shown as a horizontal black line. [85]

Looking at this figure it can clearly be seen that the interface between the layers is only above T_g at W_{p-1}. This results in the interface between layers residing above T_g for 2 seconds. Also the ΔT with which the interface resides above T_g decreases rapidly. As was shown in equation 3.12 this also rapidly increases the reptation time. It is interesting to considering figure 3.10 in combination with figure 3.11, which both consider ABS used for FFF. Reptation time at 160 °C is roughly 2 seconds and interlayer temperatures drop exponentially to below T_g within 2 seconds. As a result it can be assumed that full healing by way of molecular diffusion does not occur during FFF under the conditions as described in the work of Seppala [85]. FFF printing using printers without enclosed chambers is currently the industry standard for polymer FFF 3D-printing.

As suggested above, McIlroy [71] also states that the reduced mechanical strength at the interface (or weld) is due to the low degree of entanglement. Besides the short time that the interface resides above T_g, McIlroy also focusses on other aspects of the FFF process. Simulations made by McIlroy state that the FFF extrusion process causes disentanglement of the polymer during deposition [71][72], mostly at the outer rim of the filament. This effect is illustrated in figure 3.12. Because of the high viscosity of the filament combined with high shear stress rates placed on the polymer during extrusion through the nozzle, a plug flow is obtained, as seen in figure 3.12(b). The high shear stresses at the walls of the nozzle strain the polymer chains, causing them to stretch and orient in the printing direction as is illustrated in figure 3.12(a). This stretching and orienting of the entanglements has two notable effects. Firstly it adds to the an-isotropic nature of the material. Secondly this disentangling effect makes it more difficult for the material to re-entangle. This stretching of the polymer chains is a process which is actively used in other polymer industries in order to make parts stronger in certain directions [24][47].

As seen in figure 3.12(c) this effect is very significant. Entanglement concentration at the outer perimeter of the extruded profile are decreased to a level where they are practically non existent. During printing the interface of two layers consists mostly of these entanglement-

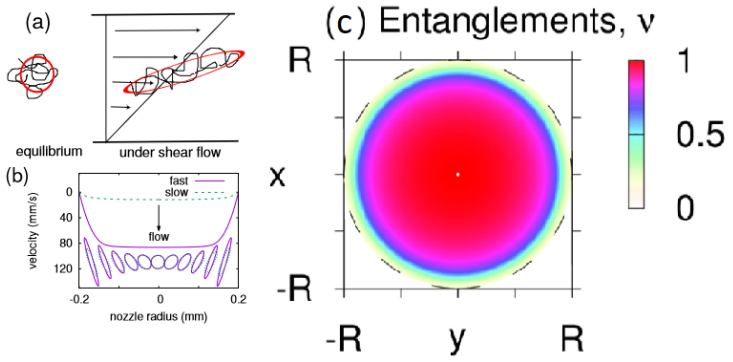

Figure 3.12: (a) Visual representation of polymer chain orientation under shear flow, (b) illustration of flow as shown to be present in FFF printing nozzles, (c) visualization of Entanglement distribution across printing nozzle [72].

free zones. This is likely to increase the time needed to achieve full re-entanglement. In this situation chains start out stressed and will first need to fully escape their tube (as was shown in figure 3.7) in order to obtain a relaxed equilibrium state. In practice this means that chains will need to diffuse further. According to McIlroy this means that the chain must diffuse its full end-to-end distance instead of it's radius of gyration [71] which is a factor $\sqrt{6}$ more [71][83]. This seems to contradict the earlier work of Wool et al. who stated that reptation time (which was stated by Wool to be equal to weld time) was dependend on the end-to-end distance to begin with. Either way this time required for the polymer to relax from it's stressed state adds significantly to the weld time.

The radius of gyration of a polymer is a more inclusive means of determining the size of a polymer chain, but fundamentally different to end-to-end distance, as it considers the distance of all monomers relative to the polymer center of mass in stead of solely the end-to-end distance of the chain extremities. When considering for example branched of circular polymer chains it becomes apparent why this would sometimes be convenient. Physically the radius of gyration thus allows to consider the polymer as a point mass with equivalent inertia to the original chain.

3.2 Aspects influencing mechanical properties of FFF parts

When considering the loss of material properties after printing, as compared to conventionally produced objects, multiple aspects need to be considered. As described in section 3.1.4 it appears to be necessary for the material to form fully healed weld bonds in order to attain similar strength at the layer interface as compared to the bulk material. This however is not the only parameter related to the printing process causing the decreased mechanical properties.

The FFF process is sensitive to multiple causes for obtaining an end product with reduced mechanical properties compared to the virgin material and conventionally produced products using the same material. In order to determine the effect of one of these it is important to know the other parameters and make sure these are constant for all samples tested. First the void phenomenon will be discussed, followed by the effect of humidity on the material properties and prints. Finally the potential for chemical reactions with oxygen or other contaminants at high print temperatures will be discussed.

3.2.1 The effect of voids in FFF parts

The FFF process is inherently sensitive to forming voids [89][101]. As the deposited filaments are cylindrical in shape stacking these will often lead to a structure containing triangular voids. Voids is the name for air gaps in the print where the extruded filament roads do not touch. This has been represented schematically in figure 3.13(a) and an SEM image of a fracture surface is shown in figure 3.13(b), which illustrates this phenomenon in a real life sample. It can be understood that these directly influence the mechanical properties by decreasing the effective cross-section area of the samples [101]. When viewing these filaments as fibers this becomes apparent. The existence of individual fibers creates many points at which failure can initiate. As a single fiber fails this decreases the surface of the sample and thus increases the stress. As a result other fibers experiencing this stress also start breaking thus initiating crack growth. In case of a $+45°/-45°$ or $90°$ print raster orientation samples are shown to generally fail along these print orientations, *i.e.* along the voids and interlayer bonds [20][61][34][94]. As a result it seems that decreasing the amount and size of voids present in the printed parts is beneficial to the strength.

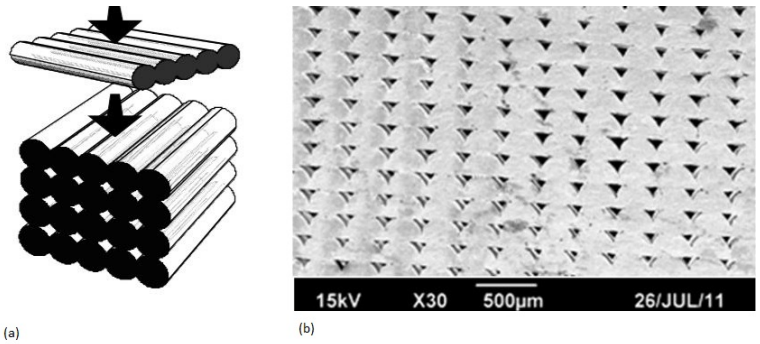

Figure 3.13: (a) Schematic representation of voids in FFF samples [89], (b) SEM image of voids in FFF samples [101].

3.2.2 Humidity effects related to FFF

Humidity has been shown to have a significant, negative, effect when printing a large selection of thermoplastic polymers. This is caused by the hygroscopic nature of many of these materials [76]. A hygroscopic material absorbs moisture from the air and as a result the moisture content of the material increases. This leads to a decrease in print quality in terms of surface roughness and accuracy [20][94], as well as mechanical properties in general [10][56][60]. As water in the polymer evaporates during printing, due to high temperatures in the printing nozzle, voids are created. This effect can clearly be seen in figure 3.14. Besides resulting in parts with lower mechanical properties, the decrease in accuracy and surface quality can also lead to parts failing. For example it may occur that prints fail due to layers warping or not properly adhering to previously deposited layers [20][94].

Another significant effect of the increased moisture content of the material is the negative impact this has on the bulk material properties of most hygroscopic thermoplastic materials [10][56][60][67]. Because of this significant impact the effect of moisture before, during and after printing needs to be considered when quantitatively comparing material properties to those reported by other sources. For example those presented by data-sheets and other studies. Also, within a single research it is beneficial to limit the range of humidity values a material is

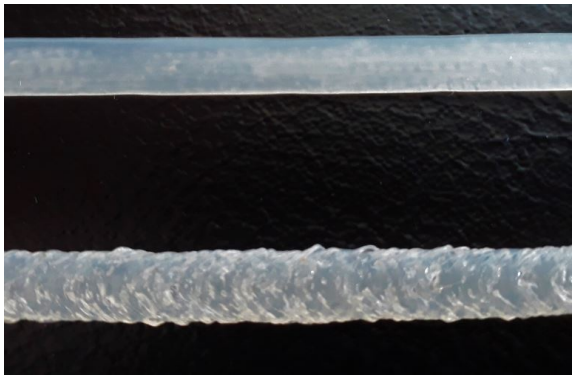

Figure 3.14: Purgelines of dry (top) and wet (bottom) nylon PA6 material created with the Markforged mark Two printer [20][94].

exposed to. For certain materials the effect of humidity is so significant that comparing results to those from other sources, or under significantly different ambient conditions, can become meaningless if this is not accounted for. For example both Alger and Kim *et. al* report a residual tensile strength of 30 % to 45 % after longer term exposure of thermoplastic polymers to moisture [10][60].

3.2.3 Oxidation and other types of contamination in FFF

One can imagine that due to the high temperatures the polymer is exposed to when passing through the extruder, the reaction rate there is greatly enhanced. Especially in open systems containing ample supplies of air flowing over the print bed it is likely that oxidation starts to occur. It has been shown by Lederle *et al.* that the exclusion of oxygen was shown to improve mechanical properties of printed parts using ABS and nylon filaments [62]. For nylon an increase of the tensile strength of roughly 40 % was shown when printing in a nitrogen atmosphere compared to air. PLA and ABS showed less drastic effects but still a strength increase of 10 % was achieved [62].

Besides the oxygen supplied by air it may also carry other (solid) contaminants. When these are incorporated in the sample they can become sites at which stress concentrations arise. These can become crack initiation points from which a crack can propagate within the part. This may then lead to failure of the part [26][37].

3.2.4 The effect of temperature on structural integrity

It can be imagined that the most effective method of homogenizing the polymer microstructure is to elevate the part temperature far above T_g for all the material in the part. This ensures that the material is fully re-entangled. However this defeats the purpose of 3D-printing as it would destroy the (3D) geometry of the part through loss of structural integrity. While this is rather obvious in the case of heating above the melting temperature, a loss of structural integrity would also be noticed by heating the entire sample to a temperature too far above T_g. At a certain point the sample will simply collapse under it's own weight. It is difficult to tie one specific temperature to this phenomenon, as it is a combination of the temperature and force applied. The heat deflection temperature of a material could provide a good indication for this [59].

3.3 Previously researched heating effects in FFF 3D-printing

This section will discuss previous research which focuses on heat treatment of printed parts in order to improve the mechanical properties of these parts. Firstly the work of Sun *et al.* will be described which looks at the effect of increasing the envelope temperature during printing on the decrease of voids, and consequential increase of strength, in AM parts [89]. The work of Hart *et al.* will be discussed next. This research focuses on the post printing isothermal annealing of samples and how this affects the fracture toughness [49]. Finally the work of Aliheidari *et al.* considers the effect of increased nozzle and bed temperatures on the interlayer fracture toughness of AM parts [11][12]. Besides showing how this improves mechanical properties, Aliheidari also introduces a method for evaluating the quality of interlayer bonds in FFF produced parts This is elaborated upon more thoroughly in section 3.4..

3.3.1 The effect of increasing envelope temperature on "neck" voids

As described in section 3.1.3, the strength in polymer welds can be increased by re-entanglement at the interlayer boundary. Re-entanglement can be achieved through diffusion of the molecule chains, which is a process that works (significantly faster) at higher temperatures. To be more precise: both layers are required to reside at a temperature above T_g. It was established in section 3.1.4 that these temperatures are not reached for most materials using a printing set-up according to the current industry standard. In order to consistently produce stronger parts, it is expected that it is beneficial to control the temperature of the printing environment (from now on referred to as the envelope temperature or T_{env}). This way the temperature of the boundaries between printed layers may be raised above T_g.

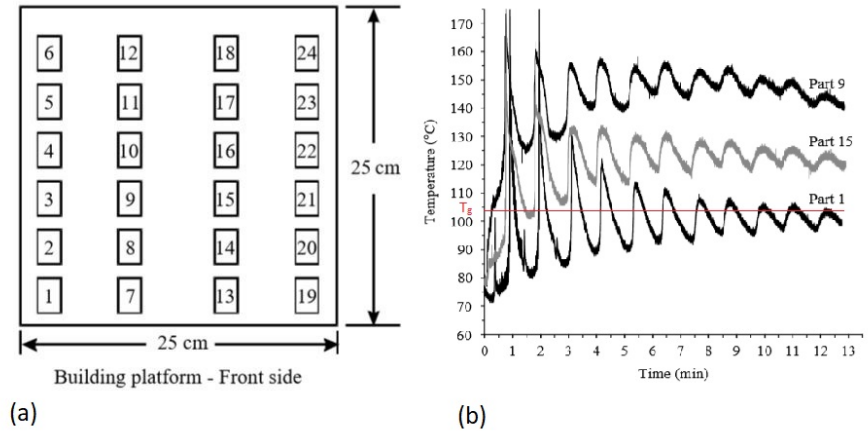

Figure 3.15: (a) Location of tested parts on build platform, (b) Temperature profiles of Part 9, 15 and 1 [89].

When looking at the literature, examples can be found where keeping prints at elevated temperatures is shown to increase mechanical properties of the material. For example in results from the work of Sun [89]. These seem to suggest an increase of average failure load of a little over 25 % when printing with part temperatures of $T_g + 50$ °C (part nine in figure 3.15) compared to a part temperature just below T_g (part 1 in figure 3.15). Figure 3.15 shows more information on the temperature profile and how the parts were placed on the building platform. For more information on why the location influences the part temperature the reader is referred to Sun's work [89].

Although these results are promising, Sun looked mostly at how an increase in temperature leads to a decrease in void size leading to improved strength. The choice of envelope temperature was mostly determined by the maximum temperature achievable in the 3D-printer instead of having a basis in the T_g of the material. Additionally, only one material type was considered and therefore the results only show an influence of increasing temperature in the case of ABS, but not the precise nature of this influence. Sun does suggest in the conclusion that increasing temperatures above T_g may lead to molecular diffusion having an influence on the bond strength. However, this was not discussed in more detail.

3.3.2 Increasing fracture toughness by post printing isothermal annealing

Looking at the effect of heat treatments on AM parts in a broader sense, the work of Hart using post printing annealing shows interesting results [49]. This research considered the post production annealing of printed parts. These annealed samples were then tested with regards to their (increased) fracture toughness. Single Edge Notch Bend (SENB) specimens were printed using a Lulzbot desktop printer and placed in an aluminum fixture and heated up to set temperatures for several hours. Using Differential Scanning Calorimetry (DSC) the critical transition temperatures were determined (such as T_g). With this data in mind the annealing temperatures were set to avoid these temperatures which resulted in 5 temperatures tested. Two of these set below the T_g (with one simply being the virgin part) and three set above T_g at 125 °C, 135 °C and 175 °C or roughly $T_g + 20$ °C, $T_g + 30$ °C and $T_g + 70$ °C respectively. The samples were, loosely, tightened within the fixture during annealing.

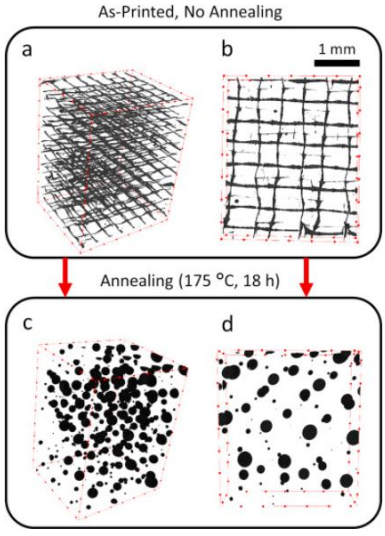

Figure 3.16: X-ray tomography showing as-printed voids and coalesced voids after annealing [49].

Hart considered the effects of annealing quantitatively by determining strain energy release rate using three-point bending of SENB samples. Additionally samples were inspected qualitatively through X-ray micro-computed tomography. For the annealing temperature-time combinations a maximum increase of fracture toughness was found of slightly over 2700 %. This is a very significant increase in mechanical properties and according to Hart, the extreme cases showed a higher fracture toughness than injection molded samples of the same material. X-ray tomography showed that before annealing, voids were oriented in a clear raster like shape

according to printing directions. After annealing the voids had grouped becoming spherical in shape at somewhat regular intervals. It was suggested that void coalescence occurred resulting from a trade off between viscous forces and surface tension. This is illustrated in figure 3.16.

The change of void geometry did not only result in increased wetting and better bonding of the layers. The formation of rounded holes in the material has an additional effect leading to an increase in the fracture toughness [55][98][99]. Janssen states in his book that considering failure by way of stress induced cracks the radius of the crack tip has a significant effect on the stress at this tip [55]. Indeed if the radius goes to zero, the stress will approach infinity. This becomes apparent when looking at equation 3.15 in which σ is the stress at the crack tip, K is the stress intensity factor, r is the radius and f is a dimensionless parameter specifying the geometry of the specimen and crack. Thus, once a crack reaches one of these voids, this radius will become significantly larger and as a result stresses at the tip will drop. Unless imposed loads are very high this will result in the crack returning to a stable status and a certain threshold will need to be overcome to make it unstable again.

$$\sigma_{ij} = \frac{K}{\sqrt{2\pi r}} f_{ij}(\theta) \tag{3.15}$$

This concept is actually also used to increase the service life of materials by increasing the residual strength [99]. Applying this principle to a structure containing dispersed voids such as shown in figure 3.16, it becomes apparent how a fracture toughness can be achieved with values that even surpass injection molded samples. It is important to consider this phenomenon when looking at the 2700 % increase in fracture toughness and therefore additional tests of other mechanical properties are recommended. By also testing for other mechanical properties in annealed samples the contribution of annealing to inter-layer bonding can be discussed in more detail.

The reported scale of the time required for achieving maximum strength with annealing is up to four orders of magnitude larger when comparing it to that of the reptation time at similar temperatures [49]. Therefore Hart suggests that for isothermal annealing this is not the only effect in play and indeed not the most significant effect for the healing rate of annealed samples. According to Hart, increased wetting leading to more intimate contact is the limiting factor for increased fracture toughness through isothermal annealing. At the same time it is stated by Hart that during the FFF deposition process reptation is indeed the limiting factor for strength development. This is due to high temperatures being maintained for periods of time in the same order of magnitude as reptation time [65][84][89].

Apart from these findings considering the annealing in an aluminum fixture, one printed sample was also annealed unconstrained as a kind of case study. This sample showed significant warping and distortion of the initial rectangular shape. This likely occurred as a result of internal stresses trapped in the sample during the printing process (as described in section 5.3.4). Also visco-elastic creep could contribute as it started to deflect under it's own weight [59] with the whole part being at a temperature roughly 70 °C above T_g. For illustrative purposes this test has been repeated and the results are shown in figure 3.17. One apparent downside of post printing isothermal annealing using a fixture is the fact that this eliminates one of the main advantages of 3D-printing, which is the design freedom regarding geometry.

Figure 3.17: An as printed vase (left) and a similar vase after 30 minutes at $T_g + 30°C$.

3.3.3 Improved fracture toughness for printing with higher nozzle and bed temperatures

In a recent paper [11] the impact of raising the nozzle and bed temperatures on the interlayer fracture toughness was considered. Aliheidari focused on using a method to quantitatively and qualitatively investigate the effect of increasing the temperature of the nozzle and bed [12]. This method will be elaborated upon further on in this report.

The research of Aliheidari [11] mostly focused on how decreasing void content led to higher ratios of intact surface. The resulting increase of surface area directly leads to higher fracture toughness (along with other mechanical properties). Besides varying the nozzle and bed temperature Aliheidari also varied layer height and width. For all these different parameters the effective surface area and fracture toughness where measured. From these measurements a direct relation was found between decreasing the void content and increasing the fracture toughness. Through the variation of these parameters the combination leading to the lowest void content resulted in the best mechanical properties.

In the case of higher temperatures this has been attributed to the higher temperature at interlayer boundaries when depositing new layers. These result in localized re-melting of the material. This way the molecular diffusion process described in section 3.1.3 occurs more readily. Also through the same principle it seems the print layers distribute better across the previously deposited layer because of the lower viscosity at higher temperature.

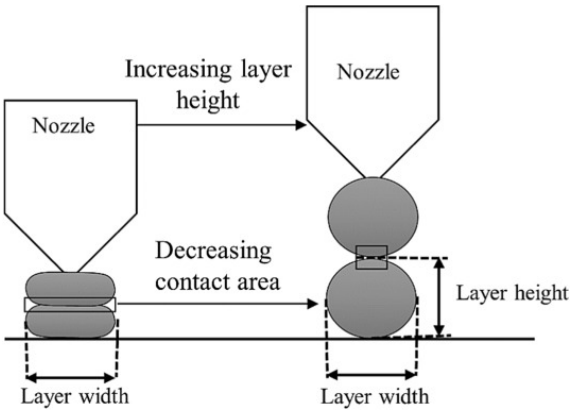

Figure 3.18: Visualization of the effect of layer heigth and width on the size and quantity of the voids in a FFF produced part [11].

When discussing the layer height and width it is usefull to consider figure 3.18 [11]. In this

figure it is clear that with a lower height over width ratio the voids not only become smaller but also more widely spread in the horizontal direction. It is indeed seen in the research of Aliheidari that this leads to an increase in the effective surface area and fracture toughness. Thus it can be stated that changing these printing parameters in the slicer program can have a significant effect on the mechanical properties of the printed part.

By considering the effective surface area, Aliheidari split the increase in fracture toughness into a contribution due to the increase in area and other effects. These other effects were mostly attributed to inter molecular diffusion of the layers caused by the parts having temperatures above T_g for an unfortunately unspecified amount of time. Although no clear relationship was shown between the time-temperature combination with relation to T_g and the related increase in mechanical properties this does seem to have a significant effect on the resulting properties of the part.

3.4 Interlayer adhesion testing of FFF parts

As mentioned in section 2.1.3, one of the limiting factors in the strength of FFF parts is the bonding between filaments. Thus, in order to determine how certain parameters affect the mechanical properties of an FFF produced part, the inter layer properties are a good place to start. No standards specifically made for FFF produced parts are yet available. The National Institute of Standards and Technology (NIST) has presented a document which advises existing standards that might be used as substitutes for the time being [39]. As a result of this lack of testing standards an effort has to be made to determine proper methods for testing the desired material properties. In this section a method for this is presented as developed by Aliheidari *et al.* [11][12]. This method is largely based upon ASTM D5528 [15], a standard for the determination of interlayer properties in fiber reinforced polymers. The theory behind this standard is discussed as well. The section concludes with presenting the theoretical maximum strength of amorphous thermoplastic polymers and how the failure modes in this material lead to actual values being significantly lower.

3.4.1 Previous work using double cantilevered beam samples

Aliheidari et al. developed such a method. This method aims to determine the interlayer fracture toughness of FFF produced samples [11][12]. A Double Cantilevered Beam (DCB) specimen was printed with the horizontal layers in the direction of the pre-crack. The design of the DCB specimen, shown in figure 3.19, was based on the ASTM D5528 standard [15]. This standard is normally used for the determination of the interlaminar fracture toughness of unidirectional (UD) fiber-reinforced polymer matrix (FRP) composites.

It should be noted that this is not one of the options suggested by NIST [39] for the direct determination of the fracture toughness of 3D-printed objects. However, they do state that it could potentially be a useful tool for evaluating, what they call, the fusion zone. This fusion zone is referred to in this report as the weld zone. Additionally they state it could provide a tool for evaluating the meso-structure. Considering the an-isotropic nature of FFF, as presented in section 2.1.3, the comparison of FFF and UD FRP materials makes sense due to both showing strong directionality of fibers (or filament) resulting in an-isotropic behavior. Both materials are stronger when loaded in the direction of the fiber/filament.

Dimensions of the test specimens were altered by Aliheidari in order to enable crack propagation without the beams undergoing plastic deformation. This way the calculation of the

energy involved with interlayer fracture propagation remains straightforward. As a measure of this interlayer fracture toughness, ASTM D5528 suggests determining the mode 1 interlayer energy release rate (G_1), which is measured in J/m^2 [15]. Mode 1 is a load condition where a stress is applied normal to the crack plane. For more information on the definition of mode 1, 2 and 3 the reader is referred to the work of Janssen *et al.* [55].

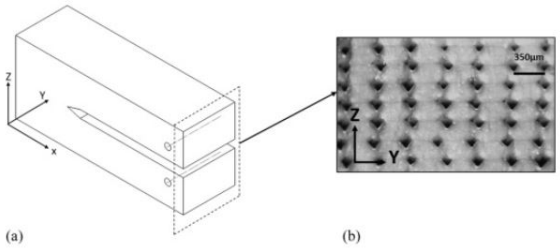

Figure 3.19: Visualization of the orientation of DCB specimens during printing and how this facilitates measuring the void content [11].

3.4.2 Determining interlayer energy release rate

For determining the interlayer energy release rate ASTM D5528-01 [15] gives a total of three methods to obtain G_{Ic} values from the measured data obtained with Double Cantilevered Beam (DCB) testing. These data reduction methods have been shown to differ by no more than 3.1 % and none was considered clearly superior to the other. As the modified beam theory (MBT) method presented the most conservative values for G_{Ic} it is the recommended method according to ASTM D5528-01.

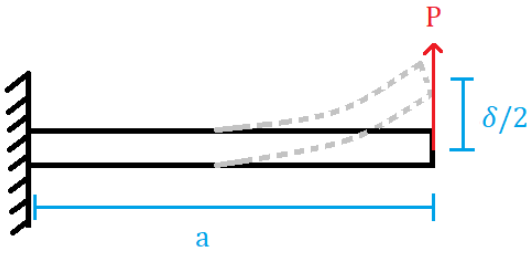

Figure 3.20: Schematic drawing of clamped beam under point load

For a perfectly built-in DCB specimen beam theory states the expression for the energy release rate can be determined by first finding the elastic energy stored in a beam clamped at one side. First the general equation for storing energy in a beam loaded in bending is considered in equation 3.16. Here θ is the angle measured as the tangent of vertical displacement $\delta/2$ over beam length a which are illustrated in figure 3.20. M is the moment applied to the beam by point load P at beam length a.

$$U_{el} = \frac{1}{2}\theta M \tag{3.16}$$

The angle θ can be written in terms of M, a, E and I for a clamped beam. E is the elastic modulus of the beam material and I is the second moment of area of the beam cross section.

$$\theta = \frac{Ma}{EI} \tag{3.17}$$

By substituting equation 3.17 into equation 3.16 and rewriting the moment M using $M = Pa$, equation 3.18 is obtained.

$$U_{el} = \frac{P^2 a^3}{2EI} \tag{3.18}$$

For a clamped beam under point load the load P can be written in terms of E, I, a and δ as shown in equation 3.19.

$$P = \frac{3EI}{a^3}\delta \tag{3.19}$$

Rewriting equation 3.19 so EI, which in principle is a constant value, becomes a function of P and δ gives equation 3.20.

$$EI = \frac{Pa^3}{3\delta} \tag{3.20}$$

Substituting equation 3.20 into equation 3.18 eventually gives equation 3.21.

$$U_{el} = \frac{3P\delta}{2} \tag{3.21}$$

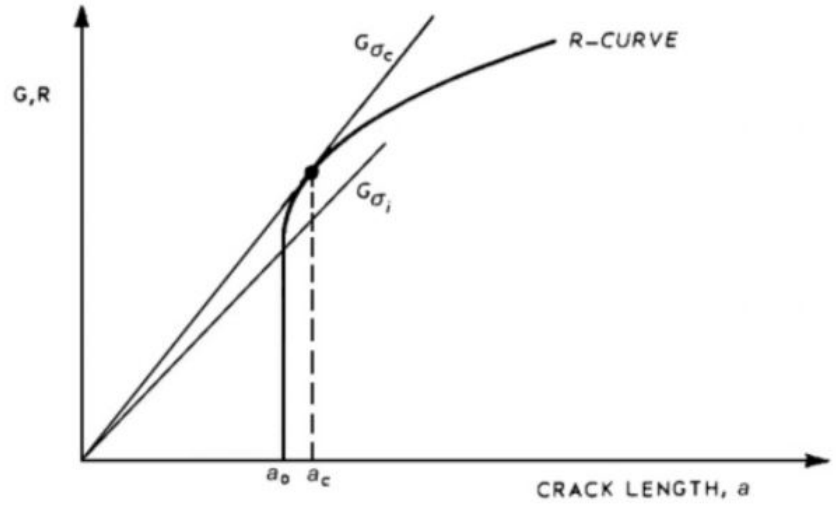

Figure 3.21: Schematic of rising crack resistance (R-curve) and energy release rate (G) [55].

In equation 3.21 the elastic energy in the beam is described as a function of the load (P) and displacement (δ). When considering the DCB specimen from a fracture mechanics point of view this energy is the stored energy within the arms at a certain pre-crack length. The pre-crack length is also assigned the symbol a and for this example is equal to beam length a used in equations 3.16 to 3.20.

In figure 3.21 a schematic representation is shown considering the resistance against cracking, R, of a certain specimen. This is shown as the R-curve, and the energy release rate (or crack driving force) G [55]. In figure 3.21 a_0 is the initial crack length and a_c is the critical crack length. The initial crack length is the point at which the crack first starts to propagate and $G > R$. However, unlike in brittle failure, when stable crack growth occurs the R curve rises. The resistance to failure thus rises and the crack starts to propagate in a stable manner. Once $\frac{\delta G}{\delta a} > \frac{\delta R}{\delta a}$ is reached in addition to $G = R$ the energy release rate rises faster than the crack

resistance and critical failure occurs.

The crack driving force in the DCB specimen is the elastic energy stored in the beams. Thus assuming no plasticity occurs in the arms it can be stated the energy available for crack propagation U_{cr} is equal to U_{el} when the crack starts to propagate. In order to obtain the energy release rate, U_{cr} needs to be divided by the crack surface area $A = ab$. Here b is the width of the specimen. This then gives the expression seen in equation 3.22.

$$G_1 = \frac{3P\delta}{2ba} \tag{3.22}$$

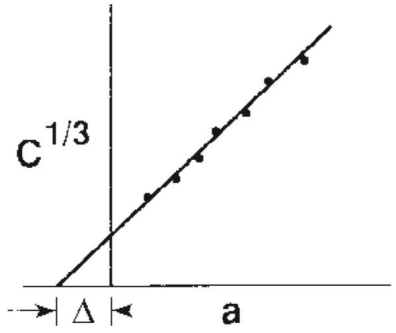

Figure 3.22: Example of least squares plot generation and subsequent Δ determination [15].

The derivation presented thus far assumes the DCB samples act as perfectly clamped beams. This however is not the case and as a result rotation may occur at the delamination front. ASTM D5528-01 [15] states this can be corrected for by treating the specimen as though it has a longer crack length, which is denoted as $a + |\Delta|$. Determining Δ can be done experimentally by generating a least squares plot of the cubic root of the compliance ($C^{1/3}$) where $C = \frac{\delta}{P}$. This is illustrated in figure 3.22. The exponent in $C^{1/3}$ can be understood by considering equation 3.20 and the definition given for the compliance. rewriting equation 3.20 as $a = f(C)$ gives equation 3.23

$$\frac{a^3}{3EI} = \frac{\delta}{P} = C. \tag{3.23}$$

It then follows that a scales with $C^{1/3}$.

Implementing Δ into equation 3.22 leads to equation 3.24 which gives the strain energy release rate determined using modified beam theory.

$$G_1 = \frac{3P\delta}{2b(a + |\Delta|)} \tag{3.24}$$

At this point it is relevant to make a distinction between the energy release rate (G_1) and the critical energy release rate (G_{1c}). G_1 is the available energy for mode 1 crack growth (for information on the distinction between mode 1, mode 2 and mode 3 loading see [55]). The critical energy release rate is the energy release rate measured when a crack starts to propagate. This means that at this point the available energy equals the energy needed for the crack to propagate. As previously stated G_{1c} is measured after a pre-crack has been made and the sample is loaded again. That is to say G_{1c} is measured for a crack with a theoretically infinitesimally small crack tip and thus infinitely high stress state [55]. For information on the relevance of infinitesimally small crack tips the reader is referred to section 3.3.2.

In ASTM D5528-01 [15] a total of 3 methods is described to determine P and δ for calculating G_{1c} from the load-displacement curve obtained with the DCB test. An example of such a load-displacement curve can be seen in figure 3.23. For the sake of consistency a choice has been made for the 5 % offset/Maximum load method (5%/max). This method leads to a single value that is not open to interpretation, unlike the Visual Observation (VIS) and Deviation from Linearity (NL) methods. Using this method a G_{1c} value is to be determined from measurement data obtained at the intersection of the load-displacement curve and a line drawn from the origin offset. This line is drawn as a 5 % increase in compliance compared with the original linear section of the load-displacement curve.

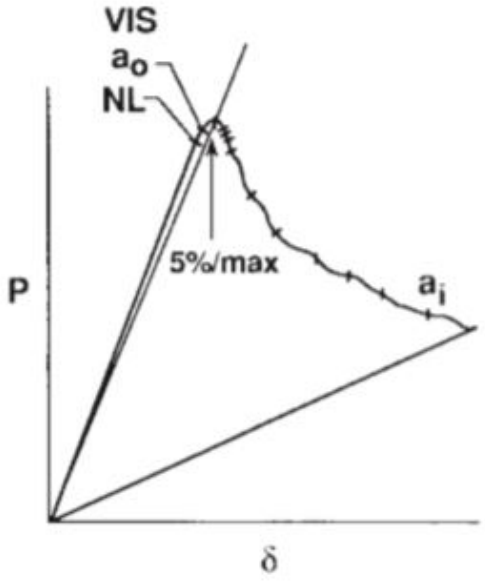

Figure 3.23: Schematic representation of DCB load-displacement curve and how data needed for determining the critical energy release rate (G_{1c}) can be gained from this curve [15]

Aliheidari deviated from the standard by employing the following method: Failure loads were obtained by visual inspectation of the samples during loading in a tensile testing machine. The load was noted at crack onset and subsequently used in an FE analysis from which the J-integral method was used to determine the energy release values. The values obtained at this stage were labeled as apparent fracture resistance, as they did not account for a possible change in surface area due to the different printing conditions. In order to be able to easily determine the percentage of voids present in the printed specimens the prints were oriented in the x-direction as indicated in figure 3.19. The interlayer fracture resistance was obtained by dividing the apparent fracture resistance by the surface intact ratio.

It should be noted that ASTM D5228 specifically expresses the need for a stable crack growth in the specimen. This is not elaborated upon in the work of Aliheidari and indeed trial runs with samples with dimensions as described by Aliheidari all showed critical failure instead of stable crack growth. It is expected that this was chosen as stable crack growth requires significantly larger specimens (up to four times the length specified by Aliheidari) and as a result significantly longer printing times.

3.4.3 Failure modes in amorphous thermoplastic polymers

As stated in section 3.1.2 the mechanical properties of a TP polymer depend largely on the dominant failure mode. For low Van der Waals forces as is the case in temperatures above T_g, disentanglement leads to plastic deformation. In extreme cases this may lead to chains being fully disentangled and no chain fracture occurring. If temperatures are far below T_g and Van der Waals forces on a polymer are very strong then stresses placed on a polymer may exceed the bond strength between monomers before chain pull out occurs. In extreme cases this can lead to fully brittle materials which fail instantaneously once a crack is formed. In thermoplastic polymers failure often occurs as a consequence of a combination of these failure modes.

At this point it is interesting to discuss the concept of theoretical maximum strength. Two different methods can be considered when determining this theoretical maximum. Although they do not present exactly similar values, they do suggest maximum values in the same order of magnitude. Both assume a perfect crystal in which atomic bonds are loaded in the direction of the inter atomic bond. Firstly using a method proposed by Griffith one can consider the amount of surface energy required to make two new surfaces when a single cube of material is split exactly in half [22]. This results in the theoretical maximum strength equaling

$$\sigma_{th} = \sqrt{\frac{\gamma E}{a}}. \tag{3.25}$$

In which σ_{th} is the theoretical strength, γ is the interfacial energy, E is the elasticity modulus and a is the interatomic distance at break.

A second method has been proposed in literature, which considers the stress-strain curve for a single atomic bond [23][22]. Again the model assumes that all atomic bonds are loaded simultaneously and in the direction of the inter atomic bond. This model considers that a stretched atomic bond is broken if it is stretched to about 10 % of its original length. This is illustrated in figure 3.24 which shows the stress-strain curve and a maximum force at 10 % strain after which bond failure occurs and stress decreases. Assuming S as the stiffness of a single atomic bond and a_0 for the initial bond length one can state that

$$S = \frac{P}{\delta}. \tag{3.26}$$

Here P is the load placed on the spring and δ is the stretch between the atoms, considering 10% strain at break, we get a maximum force (F_{max}) of

$$F_{max} \approx \frac{Sa_0}{10}. \tag{3.27}$$

From equation 3.26, equation 3.25 and figure 3.24 it follows that the theoretical maximum tensile strength for a solid should be roughly

$$\sigma_{th} \approx \frac{F_{max}}{a_0^2} = \frac{S}{10a_0}. \tag{3.28}$$

Finally, stating that a strain can be imposed on an atomic bond acting as a "spring" between two atoms, with $\epsilon = \delta/a_0$ and substituting this in equation 3.26 results in

$$\sigma = E\epsilon = \frac{S}{a_0}\epsilon. \tag{3.29}$$

It can than be stated that a maximum theoretical strength can be determined with

$$\sigma_{th} \approx \frac{E}{10} \tag{3.30}$$

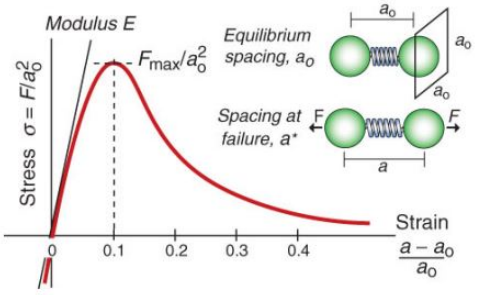

Figure 3.24: Stress-strain curve for a single atomic bond indicating failure at 10% strain [23].

Amorphous thermoplastic polymers, and in fact all material types [22][23][82], have ultimate tensile strenght values that are orders of magnitude below the values suggested by equation 3.28 and 3.30. This is due to materials never consisting of perfect crystals being loaded exactly in the direction of the inter atomic bonds. These type of values can only be approached for crystalline materials on a very small scale in the form of so called whiskers [82].

In the case of amorphous thermoplastic polymers strength values far below these theoretical maximum values are measured. This is in part due to the near complete absence of crystals, as has been described in section 3.1.1. Additionally the entanglements described in section 3.1.2 may allow for the large molecule chains to disentangle as Van der Waals forces decrease at temperatures above the material's T_g.

When a polymer is being loaded, molecule chains stretch and slip between these entanglements to a certain degree. This creates micro voids in the material bridged by polymer fibrils as can be seen in figure 3.25. These cracks with fibril bridges are called "crazes" and can be observed by the polymer whitening as the crazes scatter light. If stretching is continued upon crazing the covalent bonds in the fibrils are loaded. Once these fail a crack propagates and the sample eventually fractures. Crazing thus limits the ductility of an amorphous polymer in tension [23].

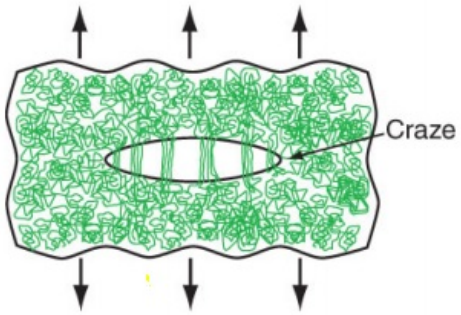

Figure 3.25: Crazing in a polymer under tension with fibrils stretching across a micro void within the material [23].

3.5 Literature summary

In section 3.1 it is specified how the microstructure of thermoplastic polymers affects the mechanical properties in the context of fused filament fabrication (FFF) production methods.

Firstly in section 3.1.1 the difference between amorphous and crystalline structures in thermoplastic (TP) polymers was discussed. The behavior of amorphous and semi-crystalline TP under elevated temperatures, which is a point of interest during this research, is elaborated upon. Subsequently in section 3.1.2 the types of strengthening mechanisms in polymers have been discussed. Mainly, the concept of entanglements has been elaborated upon as it is the most relevant in amorphous TP materials commonly used in FFF.

After the basic principles of the entanglements have been discussed, their relevance with respect to polymer welding has been addressed in section 3.1.3. Emphasis has been put on the reptation mechanisms which allows for molecular chains to move within amorphous TP's kept above their glass transition temperature. This mechanism allows polymer-polymer interfaces to achieve bulk properties, a concept referred to as a "full healing of the weld bond". The relevance of the presence of polymer welds in FFF has been discussed in section 3.1.4 by showing that an FFF part consists of stacks of polymer welds. Additionally it has been shown that a fully healed weld bond is likely not reached when using current industry standard processing parameters.

The concepts described above, which form the foundation of the research conducted in this report, are not the only parameters affecting the mechanical properties of FFF parts. In this literature study other mechanisms influencing the performance of FFF produced parts are also elaborated upon in section 3.2. Firstly in section 3.2.1 the concept of voids in printed parts is considered, which introduces an obvious decrease in mechanical properties due to decreased effective surface areas. Secondly, in section 3.2.2, it is described humidity adversely affects many thermoplastic polymers. Furthermore, as discussed in section 3.2.3, the production process generally does not take place in a controlled environment. As a result oxidation and contamination can play a significant role in the produced parts properties. Possible negative aspects related to elevated temperatures are also discussed in section 3.2.4.

Previous research into the effects of heating on FFF produced specimens has been discussed in section 3.3. The work of Sun *et al.*, discussed in section 3.3.1 focused on increasing envelope temperatures (to temperatures well below the glass transition temperature) in order to determine the effect this had on the size of voids within printed specimens and the effect of these voids on mechanical properties. Sun suggests further research into the effects of molecular diffusion on bond strength by increasing printed part temperatures above the glass transition temperature.

The work of Hart *et al.* discussed in section 3.3.2 focused on post-print annealing by subjecting test specimens to temperatures above the material's glass transition temperature. This increased the fracture toughness of the material up to 2700 % compared to printed specimens without any post-print annealing. It should be noted that this increase in fracture toughness was also due to a change in meso-structure caused by void coalescence. In order to ensure dimensional stability, the annealing process used by Hart required the printed specimens to be fixated in a clamp during the annealing process. The need for this fixation greatly reduces the design freedom which is one of the main strengths of (FFF) 3D-printing.

The work of Aliheidari discussed in section 3.3.3 focused on the effect of raising nozzle and bed temperatures on the interlayer fracture toughness of FFF produced specimens. This research also considered the effect of the increased temperature on a decrease in void content. Results obtained were corrected for the effective surface area of the tested specimens. This

presented a method to only consider the effect on the interlayer strength, i.e. the strength increase due to temperature influences on the polymer microstructure. Increasing bed and nozzle temperatures showed an increase in interlayer bond strength both before and after correction for the change in effective surface area.

Aliheidari's research not only showed interesting results with respect to printing at increased temperatures. As discussed in section 3.4.1 it also presented a testing method specifically for evaluating the interlayer bond strength of FFF specimens. Aliheidari *et al.* modifield double cantilevered beam (DCB) specimens, adapting a test standard normally used for unidirectional fiber reinforced specimens (ASTM D5528-01) for the determination of interlayer properties in FFF parts. Both the similarities and differences with respect to ASTM D5528 are described. The method for, and theory behind, determining interlayer bond strength with ASTM D5528 has been elaborated upon. Finally the different failure modes that can be observed in amorphous thermoplastic polymers are discussed. This is related to how mechanical properties in these materials differ from the theoretically maximum achievable properties due to the material microstructure.

Chapter 4

Hypothesis and research questions

In this chapter the knowledge gap in the current state of the art is described, followed by the formulation of the hypothesis which is the focal point of this research. In order to verify this hypothesis, several research questions are formulated. Finally the research approach set out to answer these research questions is described.

4.1 Current state of the art

Currently, a considerable amount of experimental research is done into the mechanical properties of FFF produced parts. These mainly focus on the printing orientation and infill of these parts [28][34][61][66][86][79][101]. Some of the experimental research on mechanical properties of FFF parts also considers the effect of thermal parameters, however these mostly try to correlate these to subsequent changes in the meso-structure of samples [49][89]. A significant number of articles on the effect of changing (*i.e.* elevating) thermal parameters partly attribute the achieved increase in mechanical properties to increased inter-molecular diffusion [11][12][49][89]. However, this is often not considered the determining factor, nor is it discussed in more detail. Research based in simulations has indicated that the increase in entanglement obtained by elevating part temperature, and thus reducing reptation time, contributes significantly to the mechanical properties of polymer welds [48]. This has also been related to the interlayer (weld bond) strength of FFF 3D-printed parts [71][72].

This research aims to build upon the research previously done in this field. Based upon this previous research a method for improving the mechanical properties of FFF produced parts is presented in the form of raising the temperature in the printing chamber. Firstly, part temperature during printing needs to be determined after increasing the envelope temperature (T_{env}). This then needs to be related to T_g in order to determine if reptation and subsequent inter-diffusion of molecular chains can occur. Additionally a testing method needs to be developed, which allows for consistent determination of interlayer properties in FFF parts. Due to the absence of testing standards for the mechanical properties of AM parts [39], it is important to properly define this testing method and the accompanying sample dimensions. Finally the difference in measured interlayer properties needs to be interpreted and related to the theory on polymer weld bond caused by increased molecular chain reptation.

4.2 Hypothesis

Based upon the knowledge gap defined in section 4.1 the following hypothesis has been formulated:

> "3D-printing Fused Filament Fabricated (FFF) parts at elevated print room temperatures increases mechanical properties by increased inter-molecular diffusion at interlayer weld bonds due to weld bonds residing above the glass transition temperature for prolonged periods of time."

4.3 Research questions

In order to verify this hypothesis a number of research questions has been formulated. These research questions are formulated as follows:

> "Does elevating the print room temperature (T_{env}) significantly prolong the time a part resides above the glass transition temperature (T_g)?"

> "How can the interlayer properties in fused filament fabricated (FFF) parts be tested in a consistent and reproducible manner?"

> "Does elevating print room temperatures (T_{env}) during printing enhance the mechanical (interlayer) properties of fused filament fabricated (FFF) parts?"

> "Is inter-molecular diffusion the dominant mechanism by which mechanical properties in Fused Filament Fabricated (FFF) parts are enhanced when printing at elevated print room temperatures (T_{env})?"

4.4 Research methodology

To answer the research questions stated in section 4.3, a research methodology needs to be defined. The methodology described blow aims to define the steps necessary to answer the research questions and subsequently verify or reject the proposed hypothesis.

Firstly a filament material that is to be used during the research needs to be defined. The T_g of this material needs to be determined in order to define print room temperatures (T_{env}).

Subsequently, a testing method needs to be defined which allows for the evaluation of interlayer properties in FFF produced samples. As no testing standard is readily available, methods currently used throughout literature are to be critically reviewed. Trial runs need to be run on samples as suggested in literature and, if relevant, adjustments need to be made to these samples in order to obtain valid, consistent and reproducible results.

Furthermore, samples upon which to perform the mechanical testing need to be printed using relevant printer settings. Most importantly this means that the samples need to be produced at T_{env} values, as these are specified based upon the determined T_g.

Additionally, the temperature history within the samples during printing needs to be determined. This is in order to verify that the part indeed resides longer periods of time above T_g. This is expected to lead to further healing of the weld bond.

Finally it is important to verify if any measured changes in the mechanical properties are indeed due to the healing of the weld bonds. This is done by inspecting the meso-structure and relating its impact to the overall change in mechanical properties.

Chapter 5

Materials, Experimental Methods, Equipment and Procedures

In this chapter the materials, experimental methods, equipment and procedures used in this research are described. This includes the production of the test samples and descriptions of the testing methods and how to analyse the results obtained using these tests.

First the process of determining which materials are to be used during this research is discussed. Secondly, the testing methods and equipment used to measure the interlayer bonding are described. Subsequently the sample dimensions and production methods are presented. Additionally the software used to determine the temperature history of printed samples is discussed, as well as the IR imaging equipment used for the validation of these simulations. Furthermore the meso structure is inspected of specimens printed at different temperatures. The chapter is concluded with a test matrix specifying the quantities of samples produced, tested and analyzed.

5.1 Materials used for printing test samples

In the following section the choice concerned with the material used during this research is discussed. Firstly, the desired material properties are presented. Secondly, the process of determining the T_g of the materials used for sample production is described. Finally, the materials that best match the properties presented and which have a T_g within the desired temperature range are selected.

5.1.1 Desired material properties for test samples

The materials used for sample production need to be (largely amorphous) thermoplastics in order for entanglements to be the dominant strengthening mechanism. This amorphous nature leads to a significant effect of the glass transition temperature and subsequent diffusion and re-entanglement as described in section 3.1.3. By using an amorphous polymer, the effect that crystallization has on the mechanical properties of a material can be kept out of the scope of this research.

Furthermore it is important that the material used for DCB testing is relatively brittle. This ensures that a clean crack can propagate through the material and no additional plasticity effects come in to play. As a result data obtained using brittle materials can be interpreted more readily [15].

It is a requirement that the filament material used during this research is readily available as 3D-printing filament that is compatible with the available FFF printers. This prevents the additional step of fabricating filament from virgin material, which is not a trivial task and requires additional equipment and expertise. Besides this, producing filament takes additional time.

The temperatures which the printer bed, nozzle and (most notably) the chamber can be kept at are very significant for choosing the material. The nozzle temperature should be capable of achieving temperatures high enough to extrude the filament. Additionally the controlled chamber temperature should be high enough to keep the part above T_g in order to be able to provide an answer to the hypothesis of this research as stated in section 4.2. Following the same logic, a material needs to be selected with a T_g which is sufficiently close to the temperature that can be reached in the printing room of the printer used during this research.

As the T_g of the material is a key parameter in this research, it is also an important parameter when choosing what material to use. These T_g values were first obtained from literature to gain an indication of the spread of T_g values. A Differential Scanning Calorimetry machine (DSC) has been used to verify the T_g values presented by literature for the actual spools of filament acquired for this research. The procedure followed for this is described in the next paragraph. For additional information on the workings of DSC machines and how data obtained with a DSC is processed, section 3.1.1 can be reviewed.

5.1.2 Determining T_g of filament materials using DSC

Prior to determining T_g and other relevant temperatures of the printing filaments the spools have been placed in a vacuum oven. They have been conditioned in this oven, under vacuum, for 18 hours at 60 °C. This had been done in order to ensure consistent (low) moisture content of the printing materials to prevent a change in humidity influencing test results as described in section 3.2.2. The temperature used was based upon T_g values obtained in literature. The value of 60 °C left a ΔT of 10 °C up to the lowest T_g among the selected materials. While no standard exists for the amount of time spools need to be placed in an oven, generally a minimum of 4 to 6 hours is advised [70]. It is suggested that longer drying times are considered to give better results [70].

It was observed that due to the vacuum in the oven temperatures, exceeded the set target temperature. Eventually the oven reached a temperature of 76 °C. The effects of this increase in temperature were only considered of importance for PLA. PLA is likely to have crystalized as a result of the time spent above T_g. Indeed when looking at the DSC image of PLA in figure B.2, no crystallization peak is seen where it would be expected in a semi-crystalline material such as PLA [44][49][71]. This indicates that this process has already occurred. The vacuum oven is a Gallenkamp vacuum oven, the DSC used a Mettler Toledo DSC3+. For information on the determination of T_g using DSC the reader is referred to section 3.1.1. The $T_g's$ values determined for all other materials tested have been measured to be well above the 76 °C reached in the oven. These values have been reported in table 6.1.

Before printing the initial tensile samples, care was taken to repeat this conditioning process of the spools before printing the samples to ensure that T_g during printing was equal to the

T_g determined with the DSC. That is to say, to minimize the impact of humidity and moisture absorption on the properties of the polymers. In this way, precise information could be obtained regarding the effect of T_g and T_{env} combinations on printing quality. Unfortunately when the eventual production of DCB samples and higher temperature tensile specimens required a new spool of filament the vacuum ovens were unavailable. Therefore after unpacking the spool it was placed in a pelican case with silica packets for the duration of the printing. This way the effect of moisture could still be minimized.

The DSC used for testing was linked to an intracooler to enable rapid controlled cooling of samples. In order to fit into the 40 μL aluminum standard cups, small specimens were cut from the conditioned filament. For each material three samples were measured. Each sample was tested using air as a purge gas flowing at 50 mL/min. Air was chosen instead of nitrogen as this better simulates the conditions during the printing process.

Two temperature profiles were used, one for PLA and one for all other materials. The initial heating cycle has the goal of removing internal stresses from the material by heating them past their T_g. Therefore it only needs to heat up to a temperature above T_g, preferably avoiding other relevant temperature regions.

The PLA profile starts at 25 °C, heats up to 100 °C, then cools back down to 25 °C and finally heats up to 350 °C. The profile used for ABS, PETG and nylon 12 (STYX) starts at 25 °C, heats up to 130 °C, then cools back down to 25 °C and finally heats up to 350 °C. Both heating and cooling was performed at 20 °C/min. The results of these measurements are included in section 6.1. All curves obtained with DSC measurements performed during this research have been included in appendix B.

5.1.3 Material used during this research

It has been decided to only include amorphous polymers, the reasons for which have been described in section 5.1.1. Thus the semi-crystalline PLA and nylon PA12 were not suited.

Combining all the parameters mentioned in section 5.1.1, the choice was made to use Glycol modified PolyEthylene Terephthalate (PETG). The PETG material used during this research was the HD Glass filament by Formfutura [5] in the color blinded saphire grey. This material meets (most of) the requirements described in the paragraphs above. It is, largely, amorphous due to the modified glycol side group as is stated in literature [12][46][49][71] and has indeed later been confirmed by DSC measurements presented in figure 6.1. Although being very brittle [38], ABS was omitted due to the available printer not being capable of reaching sufficiently high envelope temperatures. While not being inherently brittle with an elongation at break of 120 %, trial runs with PETG samples showed that FFF printed PETG tensile and DCB samples showed brittle failure (see section 6.4 and 6.5.1). As a result DCB testing was considered suitable. Additionally PETG is commonly used in (FFF) 3D-printing.

5.2 Testing methods for the evaluation of interlayer bonding

This section first introduces which testing methods are used for determining the strength of the interlayer bonding. Subsequently, the design of the double cantilevered beam (DCB) samples, based on ASTM D5528-01 [15], is shown. Along with this the accompanying test method is described. Finally the tensile testing samples and testing method are presented.

5.2.1 Testing methods used for evaluating interlayer properties

As stated in section 3.4, standardized testing methods specifically designed for evaluating mechanical properties of 3D-printed parts have not yet been defined [39]. It has therefore been necessary to determine a relevant test methods during this research. A choice was made to use two testing methods. These have been used to evaluate if an increase in interlayer strength has been obtained. The testing methods used are both based upon existing test standards for similar materials.

Firstly Double Cantilevered Beam (DCB) samples have been tested in order to measure the degree of interlayer adhesion within printed samples. This is defined as the amount of energy needed to create additional surface area through stable crack growth. For these samples, ASTM D5528-01 [15] was used as a starting point [11][12]. ASTM D5528-01 was developed for testing the interlaminar fracture toughness of unidirectional (UD) fiber reinforced polymer (FRP) matrix composites. The high degree of directionality in FFF produced parts and the an-isotropic behavior considering in and out of plane loading [61][66][101] compare well to UD FRP composites. Because of this ASTM D5528-01 was considered a good starting point for testing the interlayer adhesion in FFF parts.

Secondly standard tensile tests based on ISO 527 [52][53] have been used; this testing method was developed for extruded thermoplastic polymers. As FFF produced samples are also a type of extruded thermoplastic polymers, see section 2.1.3 for more information, this was considered a good starting point. Initially tensile tests were included in order to quickly determine at which temperatures the most interesting results can be seen. DCB testing was expected to be very time consuming and this would allow the minimization of the number of DCB tests. Tensile tests can be used to evaluate a number of mechanical material properties. An improved interlayer adhesion in tensile samples, especially those printed in the Z-direction, is expected to lead to higher strength values measured in the tensile tests. It should be noted that eventually both tensile and DCB samples have been tested across the complete T_{env} range.

5.2.2 DCB sample dimensions and testing method

As previously stated, the goal of this research is to determine the influence of printing parts at elevated print-room temperatures (T_{env}) on the degree of healing of the interlayer weld bond. Thus, it is necessary to use a testing method that looks specifically at the interlayer bond strength. Improving interlayer bonding by increasing T_{env} is expected to also improve mechanical properties in other directions than those tested in this research, however this needs to be evaluated separately. This is considered to be outside the scope of this research.

Literature study on testing methods for determining interlayer bonding suggests using Double Cantilevered Beam (DCB) samples as described in ASTM D5528-01 [15]. The work of Aliheidari [11][12] stands out as this specifically focused on evaluating the interlayer bonding in 3D-printed samples. The work of Aliheidari has been discussed in depth in sections 3.3.3 and 3.4.1.

The dimensions of the DCB samples used in this research can be seen in figure 5.1. These dimensions have been determined by using the work presented by Aliheidari [11][12] and ASTM D5528-01 [15] as a starting point and performing additional iterations to the design process.

Initially samples with dimensions as described by Aliheidari had been tested in a trial run. This showed that no stable crack growth occurred in any of the samples. This was expected to be due to the samples a/w ratio, or pre-crack (a) over sample length (w) ratio. A high a/w is likely to induce critical failure before stable crack growth can occur [55]. Indeed ASTM D5528

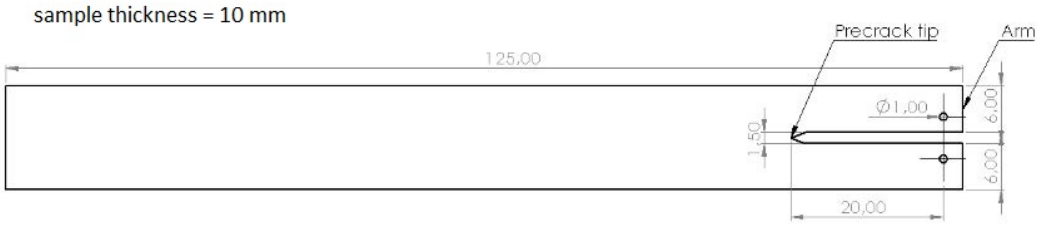

Figure 5.1: Dimensions of DCB test samples used, based on ASTM D5528-01 [15] and the work previously done by Aliheidari [12] (all dimensions in mm).

[15] suggests the use of significantly longer samples. A sample length of at least 125 mm is suggested, with a pre-crack length which is determined to have a maximum value according to equation 5.1. This equation relates the pre-crack length (a_o) to the sample thickness (h), E-modulus in the print direction, which in the standard is referred to as the fiber direction, (E_{11}) and an estimated value for the critical energy release rate (G_{Ic}).

$$a_0 \leq 0.042\sqrt{\frac{h^3 E_{11}}{G_{Ic}}} \tag{5.1}$$

For PETG the E-modulus was given to be 1940 MPa [5]. No data was provided by the filament manufacturer on the energy release rate of the material and thus literature was consulted. A maximum value for G_{1c} of 3800 J/m^2 was found [68]. Inserting these values in equation 5.1 it was found for PETG $a_0 \leq 47$ mm.

As the values found for a_o represent maximum values for the pre-crack, and both G_{1c} values and E-moduli were not measured independently for this specific material and direction, a pre-crack length of 20 mm was chosen for the DCB samples. This way if the actual E_{11} would turn out slightly lower, or the G_{1c} would turn out higher, resulting in a lower maximum pre-crack length, it would likely still provide a valid sample. It was verified in trial runs that the design shown in figure 5.1 indeed resulted in stable crack growth. Additionally printed samples showed no plasticity in the arms of the DCB samples, which is needed to ensure consistent and valid results [15].

DCB testing works by first loading a sample perpendicular to the arms, indicated on the right in figure 5.1 [15]. In order to facilitate this a hole has been printed in each sample through which a steel rod can be passed. This rod is used to fixate the specimen to a specially made aluminium clamp insert. These inserts are placed in a tensile testing machine that can pull apart the arms at a constant displacement rate while registering the force required to do so. The insert design is presented in figure 5.2, including all relevant dimensions. The test set-up, including a clamped specimen, is presented in figure 5.3.

According to ASTM D5528 it is advisable to test a minimum of 5 samples for each specific test case. Therefore 5 samples are printed and tested for each T_{env} value. Before testing sample dimensions are checked using Mitutoyo digital calipers. These are subsequently noted down and entered into the TestXpert software ASTM D5528 test program. The samples are tested using a Zwick/Roel 10 kN materials testing machine [6]. Samples are mounted in the clamps of the testing machine using specially made fixtures. An example of this is shown in figure 5.3. The fixtures are positioned using a spirit level. Tests have been performed using a displacement rate of the crosshead of 2 mm/min.

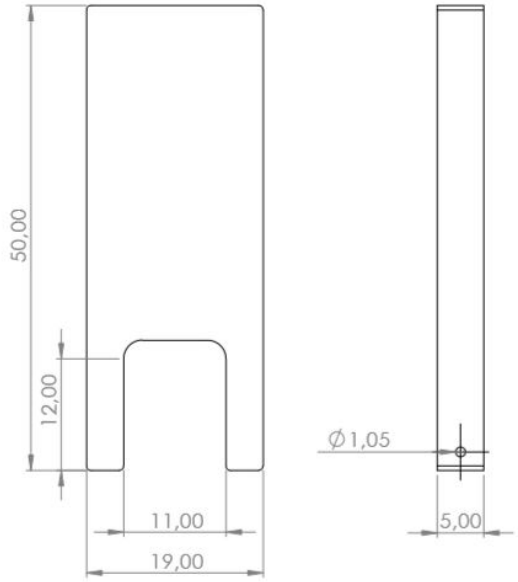

Figure 5.2: Dimensions of DCB test clamp made (all dimensions in mm).

During DCB testing it is important to constantly monitor the sample and stop the test as soon as a noticeable crack occurs at the pre-crack tip. The sample is then unloaded, after which markings are made on the sample at 1 mm and 5 mm intervals according to ASTM D5528-01 [15] to help monitor the crack growth. Subsequently the sample is loaded again. When the crack starts to propagate again, stable crack growth is expected to occur. The propagation of the stable crack growth is measured against the load and displacement measured on the tensile testing machine. This is done by making measurements as the crack passes the markings made on the sample.

In order to facilitate this inspection and produce more precise results a magnifying glass is used. The load-displacement curves thus obtained allow for the determination of interlayer energy release rate (G_{1c}). The method by which this can be done, as well as the theory upon which the method is based, has been described in section 3.4.2 and ASTM D5528 [15].

5.2.3 Tensile sample dimensions and testing method

As this research focuses on the interlayer strength in the direction perpendicular to the print bed (*i.e.* the z-direction), samples have been printed in this direction. This upright printing position can be seen in figure 5.4, which shows the slicer interface. This has mainly been done to ensure loading perpendicular to the interlayer bonding. Sample design is based on ISO 527 [52][53]. This standard prescribes so called dog-bone samples according to specified dimensions. Type 1A samples were used, the dimensions of which can be seen in figure 5.6.

Due to the difficulties related to printing a high and thin specimen using FFF, two tensile specimens are printed simultaneously in one part. This way a support structure can be printed in between the specimens, giving the part more stability during printing. This support structure is not offered as an option in simplify3D (the slicer used during this research) and therefore needs to be designed using CAD (for which SolidWorks has been used). A choice has been made for a thin walled support structure connecting the tensile test samples. This was found to provide a consistent print path across all printed layers and, as a result, have minimal and

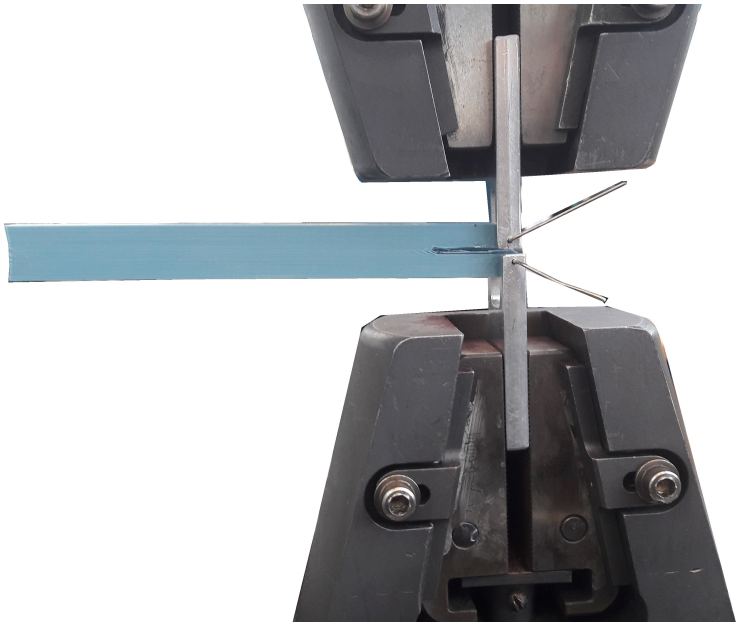

Figure 5.3: Test setup used for the evaluation of DCB samples using the Zwick/Roell testing machine together with the additional fixtures.

influence on part meso-structure throughout the sample. As can be seen in figure 5.5 the specimens printed as such maintain structural integrity during printing. Additionally, figure 5.4 and figure 5.5 show the inclusion of a brim (the enlarged footprint). The function of such a brim is elaborated upon further in section 5.3.4.

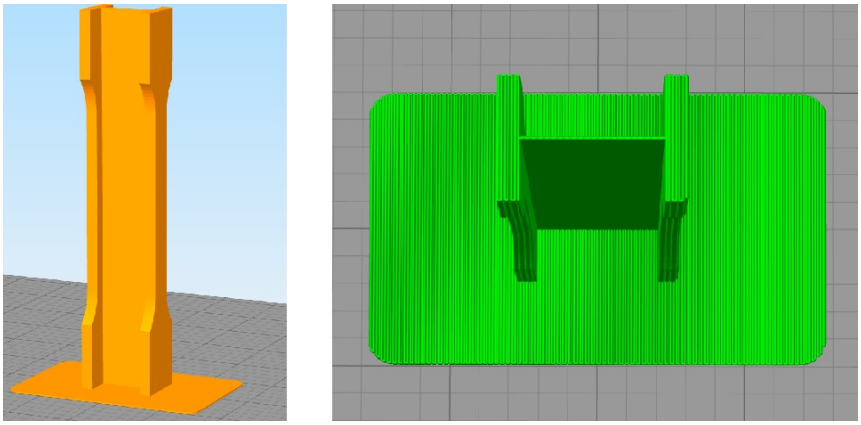

Figure 5.4: Tensile sample in Simplify3D showing the thin walled support structure and orientation of print direction in the part.

Samples have been produced two at a time with a support structure in between to ensure stability during printing. This can be seen in figure 5.5. Support structures were removed before testing using a sharp knife.

The tensile test samples are tested on the same Zwick/Roel 10 kN materials testing machine. As this type of sample can directly be placed in the clamps of the testing machine, no additional fixtures are needed. The TestXpert software also has a ISO 527-2 testing program. Thus after using the Mitutoyo digital calipers to measure the dimensions of the test samples this data could be noted down and entered into the testing program. Tests have been performed using a displacement rate of the crosshead of 2 mm/min. ISO 527 also specifies that it is required

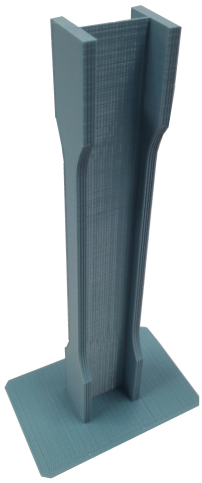

Figure 5.5: Set of two vertically printed tensile specimens

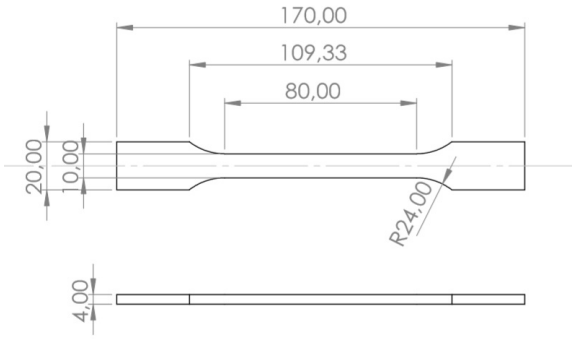

Figure 5.6: Dimensions of tensile test specimens according to ISO 527 [52][53] (all dimensions in mm).

to test at least 5 samples for each test case. Due to the tensile samples being printed two at a time the choice was made to test all 6 samples produced. This also prevents any discrepancies in the test results due to choosing either one additional left or right sample in a sample set.

Results obtained using tensile tests according to ISO 527 are presented as a stress-strain curve from which the E-modulus (the slope of the initial linear stress-strain relation), yield strength (σ_y), ultimate tensile strength (UTS) and elongation at break (ϵ_f) can be determined. Additionally the tensile toughness (U_T) of a material can be obtained by calculating the integral of the stress strain curve until fracture. This is a measure for the energy a tensile sample can obtain before fracture. A schematic representation of the stress-strain curve obtained by a tensile test is illustrated in figure 5.7.

The stress strain curved obtained from most tensile testing machines shows engineering stress-strain curves instead of a true stress strain curve. There is a very significant difference, however for most applications engineering stress and - strain are sufficient. During this research when stress and strain are mentioned, this should be considered to be the engineering stress and strain. For more information on the distinction between the two the reader is referred to [45].

Besides using a stress strain curve to obtain quantitative data on mechanical properties of

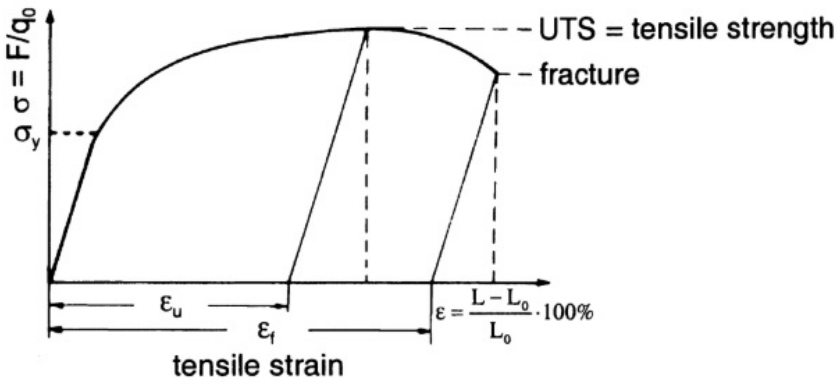

Figure 5.7: Schematic representation of engineering stress-strain curve and how important mechanical properties can be determined from this curve [45]

the material the shape of the curve can also be used to make qualitative statements regarding the material. Such a curve can, for example, be used to make statements about the brittleness or ductility of a specific material. A brittle material would only show a linear curve without a significant change in the rate of elongation. In ductile materials this change in rate is present and as a result a clear distinction between yield strength and UTS is possible.

5.3 Production of test samples

In this section the printing process used for the production of the test samples is described. Subsequently the range of temperatures at which samples are produced is defined. Finally the printer used for sample production is presented.

5.3.1 Printing parameters used for production of test samples

In order to give the reader a complete overview and to aid in further research, the critical print settings are documented and discussed in this section. All print settings, including those not discussed in this section, have been included in Appendix A.

Besides the temperature of the printing room, which is at the core of this research, some other settings have also been found to be of importance. These are the layer height, printing orientation, additional printed features such as support structures and the types of layers the part should be built with.

5.3.2 Layer height

Starting off with the layer height, a choice was made for 0,1 *mm* layers. Looking at the available literature on the effect of layer height on mechanical properties data sometimes contradicts [63][64][87][93]. However, a high absolute strength of the test specimens is not the main focus of this research. Therefore the choice for a 0,1 *mm* layer height was mainly based on another effect of the layer height; in order to obtain consistent results a high accuracy of the printed samples is desired. A lower layer height increases the dimensional accuracy of FFF produced parts. As stated by Milde *et al.* [73] this is especially relevant in the case of sharp edges required for the functionality of the part. This is indeed the case for the DCB samples. The same layer height was chosen for tensile specimens for the sake of consistency.

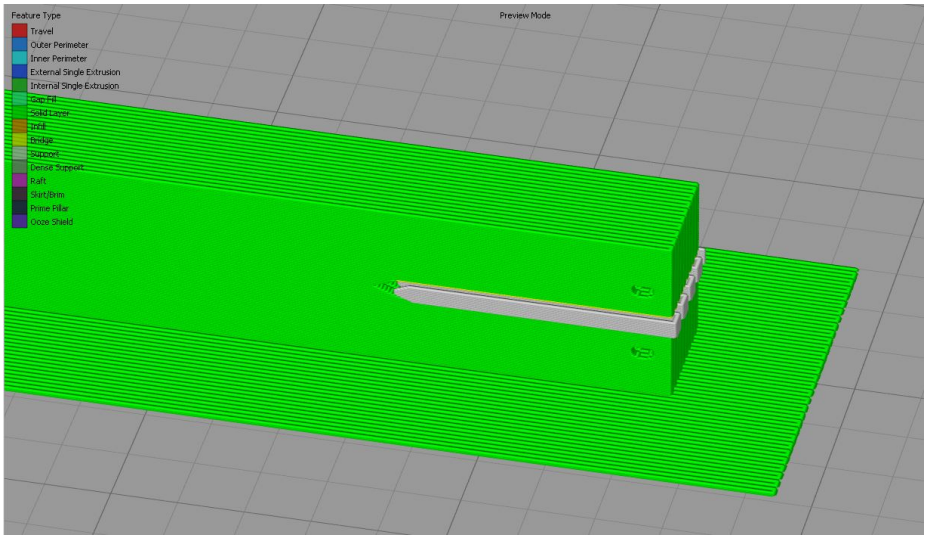

Figure 5.8: DCB sample in Simplify3D showing print orientation. Print consists fully of solid layers (green) except for support in the pre-crack (grey).

5.3.3 Printing orientation

Printed roads have been oriented along the length of the DCB specimens. By using this printing orientation, the crack is expected to propagate along the roads in the print orientation resulting in a straight crack between two layers. This is due to the crack following the path of least resistance, *i.e.* the weaker part of the sample fails first which is expected to be the interlayer interface, at least until full healing is achieved. Additionally the stress is highest at the crack front due to the crack tip having an infinitesimally small radius as described in section 3.3.2. As a result the measured quantities are expected to represent the interlayer bond strength, as is desired. Because of the desired printing layer orientation as presented in figure 5.8, it is necessary to include support in the pre-crack of the DCB samples. This needs to be removed after printing using a sharp (thin) knife (*i.e.* a boxcutter).

As has been shown in figures 5.4 and 5.5 tensile samples are printed standing upright with two samples being printed in one part. The samples are connected with a thin support feature. Again this support needs to be removed after printing using a sharp knife. Figure 5.4 also shows tensile specimens are printed with roads predominantly oriented in the longest direction of the samples, the z-direction not withstanding. This direction was selected mainly due to two reasons. It significantly speeds up the printing process compared with other methods, but also requires less manoeuvring of the print head. This results in less jerky print head movements and cleaner prints with better surface quality. A reduced chance for printing errors is expected to increase the accuracy and reproducibility of test results.

5.3.4 Adhesion to the print bed

During FFF printing samples may be affected by warping [8][19][95]. Warping is the name given to distortion in printed parts due to a difference in contraction between subsequently deposited layers upon cooling. The effect of this process is illustrated in figure 5.9. To prevent this it is important to ensure proper bed adhesion of the part. This can be done by adding a brim to the part [19]. Brim is the name given to an addition at the bottom of the print used to improve bed adhesion. An example of a brim can be seen in both figure 5.4 and 5.8. This feature enlarges

the surface area of the footprint of the part without additional layers above pulling at the first layers as a result of thermal stresses. Thus the part sticks better to the print bed. A brim is especially important at high infill percentages because in this case the residual thermal stresses are higher, which became apparent during the printing of the trial samples presented in figure 5.9.

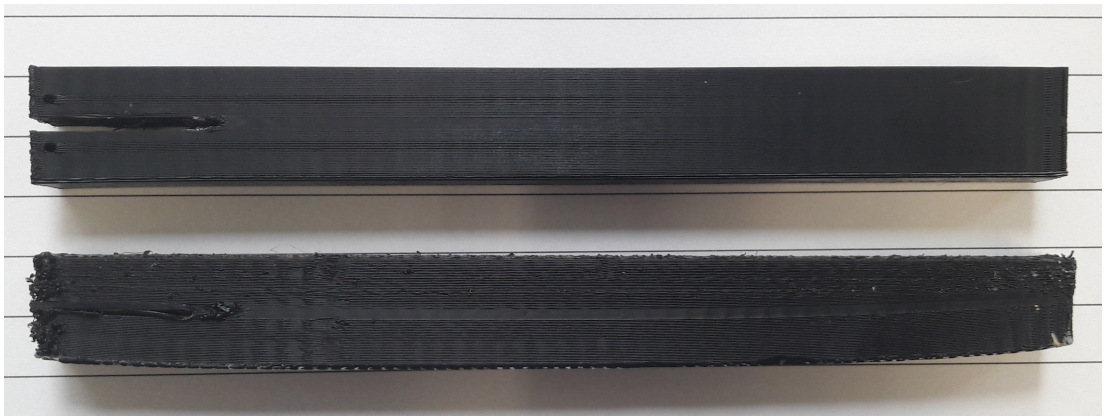

Figure 5.9: Illustration of the effect of warping on printed parts. Both samples have been printed using the same settings (see appendix A) however the top sample was printed using Dimafix, the bottom sample using painter's tape.

Additionally adhesives or different types of printing surfaces can be used in order to improve the bed adhesion of the print. Usually this is either an adhesive or a type of tape to which the printed material adheres more readily than to the (*e.g.* glas) surface of the printbed [19][95]. For this research an adhesive specifically developed for use with 3D-printing was used. This adhesive, called Dimafix, ensures strong bonding at elevated bed temperatures (>95 °C) and releases when the bed cools down after printing (<50 °C) [2]. Combining the brim and adhesive prevented all visible warping.

5.3.5 Printing solid and unidirectional parts using FFF

In order to obtain significant results from the DCB it is desired to obtain a solid part. This will ensure stiffness in the sample preventing additional torsion effects during testing. This added stiffness is especially relevant due to the absence of wall and top layers which normally provide this stiffness. Additionally in normal prints 0° and 90° layer orientations are printed alternately, which again provides stiffness. However as described in the previous paragraph this is also not the case when printing the DCB test samples. Besides the beneficial stiffness a completely solid part will also increases the surface area and provide a more homogeneous sample. When looking back at equation 3.24 it becomes apparent that a clearly defined surface area is beneficial when determining the energy release rate. Thus a fully solid part provides the most significant results).

Printing a sample to be completely solid is not trivial when using Simplify 3D slicer software. When standard infill parameters are selected, even when selecting a 100 % infill no solid parts are obtained. This becomes especially apparent when the infill is forced to be unidirectional in all layers. When printed as such without top and bottom layers under different angles it can be seen that layers parallel to each other in the x or y plane are not properly stuck to each other. As a result a harmonica-like (or book-like) structure is obtained which offers no stiffness against torsion. In order to obtain samples that are completely solid it is necessary to force the

software to build solely bottom layers (which do print as solid layers) by setting the amount of bottom layers to 9999. The result obtained by this can be seen in figure 5.8 in which solid layers are indicated as green whereas infill would be defined with orange.

Additionally a choice has been made to not include perimeter layers to facilitate interpretation of test results. While perimeter layers reduce the overall surface roughness of printed parts, they also introduce new parameters and layers printed in different direction. For both tensile test samples and DCB samples, bottom layers are set to 9999 and perimeter layers to 0 in order to make printed parts solid and facilitate interpretation of the results.

5.3.6 Temperature settings during printing

Temperature settings are based on the T_g of the printed materials. An estimation of part temperatures at elevated T_{env} has been made using the work of Sun *et al.* [89]. Sun showed that at nozzle temperatures of 270 °C and T_{env} ranging between 50 °C and 70 °C led to a part temperature at T_{env} + 25 °C. It was also shown that increasing or decreasing the nozzle temperature (at least for a ΔT of 10 °C) did not significantly affect part temperature.

With this information an initial estimate has been made for a set of T_{env} temperatures and the respective part temperatures directly after printing. These are shown in table 5.1. After an initial reference sample printed with T_{env} at room temperature a range of T_{env} values are selected. These are expected to provide a data set for the part residing at a range of temperatures below and above T_g during the print.

After printing, samples were removed from the bed, support and brim material were removed from the part as previously described and subsequently stored in zip-lock bags with a packet of silica gel. This storage method was used to ensure minimal environmental influences on the mechanical properties of the prints.

The difference between the number of printed parts and the eventual test samples observed in table 5.1 is caused by the fact that two tensile samples are printed in a single part. This has been discussed in depth earlier in this section. Temperature settings were limited to a maximum T_{env} value of T_g − 15 °C due to the available FFF printer.

Table 5.1: Temperature settings and the respective number of samples tested for DCB and Tensile test specimens.

PETG (T_g = 84 °C)

	T_{part} (≈)	50 °C	T_g − 20 °C	T_g − 10 °C	T_g	T_g + 10 °C	
	T_{env}	25 °C	T_g − 45 °C	T_g − 35 °C	T_g − 25 °C	T_g − 15 °C	
Testing method	**DCB**	5	5	5	5	5	25
	Tensile	3	3	3	3	3	15
							40 **parts**
							55 **samples**

5.3.7 Printer used for the production of test samples

For this research the DDDROP Leader Twin was used to produce the test samples. Due to its enclosed print chamber it is stated to have the capability to control the room temperature up to 70 °C. This is not high enough to print up to $T_{env} > T_g$, but instead only up to $T_{env} = T_g - 15$ °C. This was thus set as the maximum T_{env} value for this research.

In situ measurements of T_{env} were made during the printing of test samples using an external thermocouple. The thermocouple was consistently located roughly 5 *cm* in front of fan located in the print head as presented in figure 5.10. This was considered to provide a representative T_{env} value during printing. When printing the benchmark samples at room temperature with

an open printing chamber the thermocouple indeed showed a consistent temperature of 23°C at this location.

These in situ measurements using the external thermocouple indeed showed that the stock printer was not able to reach the desired temperatures with the bed temperature at 80°C (the desired bed temperature for PETG). Raising the bed temperature up to the point where $T_{env} \approx 70$ °C meant setting the bed temperature at 120°C. This resulted in a loss of structural integrity due to material starting to collapse at the bottom of the sample under the weight of previously deposited material. Due to the bed being the only heat source in the printer, no other method of raising T_{env} was readily available.

It was decided to make an effort to raise T_{env} by insulating the DDDROP printer using radiator foil and polystyrene insulation foam. Additionally the fan speed of the two fans placed at the rear of the printer, which pull air into the printer to cool the part, were set to lower speeds and the air intake was blocked using tape as can be seen in figure 5.10. Combining this with raising the bed temperature to 90 °C resulted in T_{env} values up to 70 °C while maintaining structural integrity of the printed specimens. An image showing the DDDROP before and after insulating is included in figure 5.10 for reference. The external thermocouple can also be seen in this figure.

Figure 5.10: Photograph showing stock DDDROP set up (left) and the insulated DDDROP printer (right) capable of reaching controlled T_{env} up to 70 °C and the external thermocouple.

5.4 Additional methods used for analyzing test samples

Besides testing the mechanical properties of printed samples, additional methods for analyzing the samples are used. These serve the goal of explaining differences in mechanical properties measured for samples printed at different T_{env} values. This section describes the different methods used to simulate the printing process and inspect the samples during and after printing.

Firstly, the reasoning behind using simulations in stead of in-situ measurements is discussed. Subsequently, the process of obtaining simulations of time-temperature plots within the printed samples is discussed. IR imaging is used to monitor the part temperature during printing, in order to verify results obtained with simulations. Optical microscopy and micro Computed Tomography (CT) are used in order to evaluate the meso-structure of samples printed at different T_{env} values.

5.4.1 Simulation instead of in-situ measurements

In order to reach envelope temperatures above room temperature a closed (isolated) printing environment is required. As a result specialised equipment would need to be installed in order to monitor the part temperature in-situ. This requires significant alterations to be made to the hardware of the printer used. Unfortunately this was not possible during this research. As an alternative a software package has been used which is developed specifically for determining thermal behavior of polymer AM (FFF, FDM and SLS) methods.

5.4.2 The working principles of Digimat AM

The software package used is a finite element method (FEM) software specialised for determining thermal response in polymer AM (FFF, FDM and SLS) parts during production. The name of this software is Digimat AM by MSC Software. Digimat AM not only considers the geometry of the part (which needs to be presented as STL file) but also utilizes the G-code used to print a part. As the software uses the G-code, it also accounts for the directionality of the printed layers and printing velocities. Information regarding STL's and G-codes and their importance in relation to FFF was presented in sections 2.1.1 and 2.1.3.

The software meshes the part using voxels. G-code is required as input, as well as an STL file prescribing the geometry. By combining this with additional information on the printer and printing conditions used (such as printing room temperature and print volume) the software can model the temperature history and the materials response layer by layer. It generally does so by first simulating the response of representative volume elements (RVE's) consisting of an individual voxel and homogenizing the result. Using RVE's is a method often used for modelling the behavior of FFF parts [81][86]. For small scale applications the software is able to simulate the temperature effect of the filament as it is being deposited. This is the main point of interest for this research. The method of achieving this desired accuracy of the simulations is described in section 5.4.3.

Besides including geometry and G-code of the samples, Digimat AM uses a material card that specifies thermal and mechanical properties of the material used. These include the specific heat capacity per temperature and the thermal conductivity of a material. Due to the software still being relatively new, the database of available materials is small, consisting only of nylon PA6 and ABS. Thus running simulations using thermal properties specific for PETG was not possible without additional measurements. For the course of this research this was omitted due to limited time. As thermal properties for PETG and ABS are relatively similar (*i.e.* in the same order of magnitude) simulations for PETG are run using the ABS material card. The difference in thermal properties is included in table 5.2.

Table 5.2: Comparison of thermal properties of ABS and PETG [3].

	ABS	**PETG**
Specific heat capacity [J/kgK]	1400	1200
Thermal conductivity [W/mK]	0,23	0,29

5.4.3 Assumptions made setting up simulations

Simulations run with Digimat AM are initially representative for tensile specimens. In order to improve accuracy of the obtained time-temperature graph it was decided to run the simulation on a small segment of the tensile specimen. This was done by performing the following steps.

After initial coarse meshed simulations of the whole specimen print geometries it became apparent that around 1 cm removed from the bed in z-direction the temperature of the part reached T_{env}. Similarly, within around 1 cm removed from the print nozzle the part also reached T_{env}. An iterative process was used scaling down mesh size and sample size. At each step obtained temperature data was compared with data obtained at the same time step for a previous step. This was done to verify that similar time-temperature curves were obtained for the new meshes and samples. Thus, a 10 mm tall section of the $4x10$ mm^2 mid section of the tensile specimen was isolated for simulation, allowing for much more detailed simulation. A solution could then be obtained which did not make use of RVE's. The actual path of the filament could now be followed in stead of obtaining results per printed layer. This provided temperature measurements at locations in between printed layers at a 1 second interval.

The bed temperature was set to T_{env} in order to simulate the part semi-infinitely continuing below the sample. This can be seen in figure 5.11. DCB sample simulations were omitted as similar simplifications still resulted in excessive simulation run times and storage space running out. DCB simulation was only possible on a per layer basis resulting in minimum measurement interval of 10 seconds. No significant additional information could be obtained this way. Due to a relatively small zone being impacted by the nozzle tensile sample simulations are also used as indication for the time-temperature history of printed DCB samples.

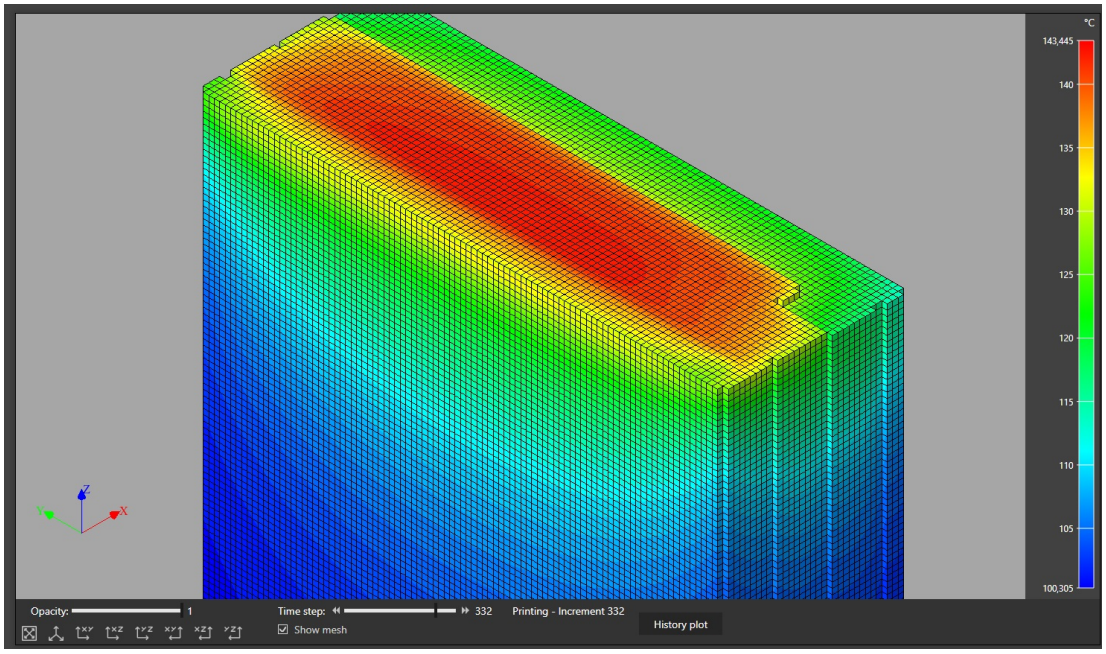

Figure 5.11: Image showing the Digimat AM post processing screen of a simulation which has been run following the filament path.

It is noteworthy that tested areas for DCB samples are closer to the bed. These are actually within the area for which bed temperature has been shown to still impact the part temperature. As a result actual temperatures within the specimens are expected to be higher than simulation would suggest. This was verified using a by layer simulation with a fine mesh ($0,1$ mm^3 voxel size). As a result effects due to the part remaining above T_g may occur earlier than expected when considering the simulated time-temperature curves based on tensile specimens.

5.4.4 Digimat AM settings used in simulations

As described in section 5.4.3 an iterative process has been used to obtain the samples eventually used in the Digimat AM simulations. These $4x10x10\ mm^3$ samples are meshed using $0,1\ mm^3$ voxels describing the filament as it is being deposited. The G-code imported has been generated using the same settings used to print the tensile specimens. As stated T_{env} is the only parameter varied across the simulations. Simulations have been run over the same range of T_{env} values described in table 5.1. Temperature-time curves are obtained by taking measurements midway during printing the 10 mm samples. Care was taken to verify that the bottom of the sample was at T_{env} at this situation.

Measurements are taken for each T_{env} simulation at three locations. The first curve is obtained by plotting the data for a node at the middle of the sample, in the middle of the filament road at that location. Secondly a curve is obtained for a node at the middle of the wall. Finally a curve is obtained by looking at a node in the corner of the sample. These locations are specified in figure 5.12.

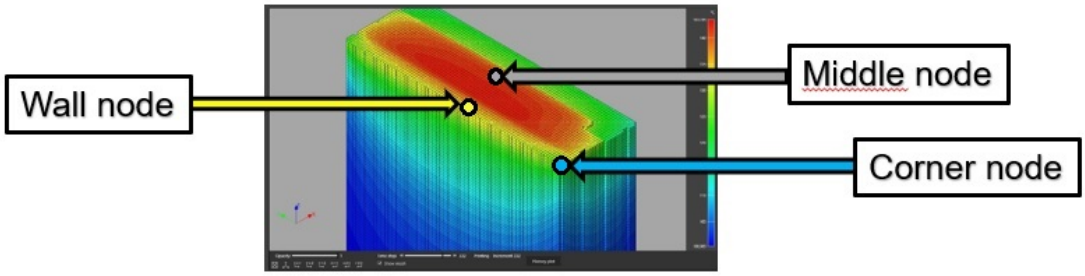

Figure 5.12: Image showing the Digimat AM post processing screen of a simulation which has been run following the filament path.

5.4.5 IR imaging equipment used for verifying simulations

In an effort to validate the simulated values infrared imaging was used to obtain experimental data on the temperature of the tensile specimens during printing. For this purpose a FLIR SC300 series infrared (IR) camera with a FOL 30 mm lens was used. IR cameras can not obtain images through transparant covers due to the cover also emitting IR radiation. This results in the camera recording the temperature of the cover, not what is occurring behind the cover. Additionally the camera was too big to place inside the printer without risking damaging both the camera and the inner workings of the printer. As a result only the situation at room temperature was observed using the IR imaging. Data obtained with the FLIR was processed using the FLIR Tools software. In order to obtain accurate readings an emission coefficient for the relevant material is needed, which indicates effective a material is at emitting thermal radiation. This is at a theoretical maximum when it has a value of 1, which does not occur for real materials [91]. An emission coefficient of 0,95 was set in the software. This was obtained from literature as a representative value for non white polymers [91]. Measuring the temperature of a printed sample with this emissivity after completely cooling down indeed showed a deviation of no more than 1 °C from the ambient temperature measured in the room using an external thermocouple.

5.4.6 Obtaining, processing and scaling IR data of printed tensile specimens

The DDDROP printer used for the production of the PETG samples tested has a bed which moves down relative to the print head. As a result, using a IR camera with a measurement point placed on a specific layer will always show the same layer relative to the print head. As a result the same periodic temperature history will be shown for each new deposited layer (once a steady state is achieved).

This is in contrast with the time-temperature curve presented by Digimat AM, which considers a single node which continously gets further removed from the print head as new layers are deposited. In order to be able to compare the results it was required to combine the data of several measurement points situated below one another. These points are presented in figure 5.13. Using ImageJ it was determined that each point was located 2,5 layer ($0,25\ mm$) below the previous measurement location. In order to obtain a curve representative for a point moving away from the print head the following process was used.

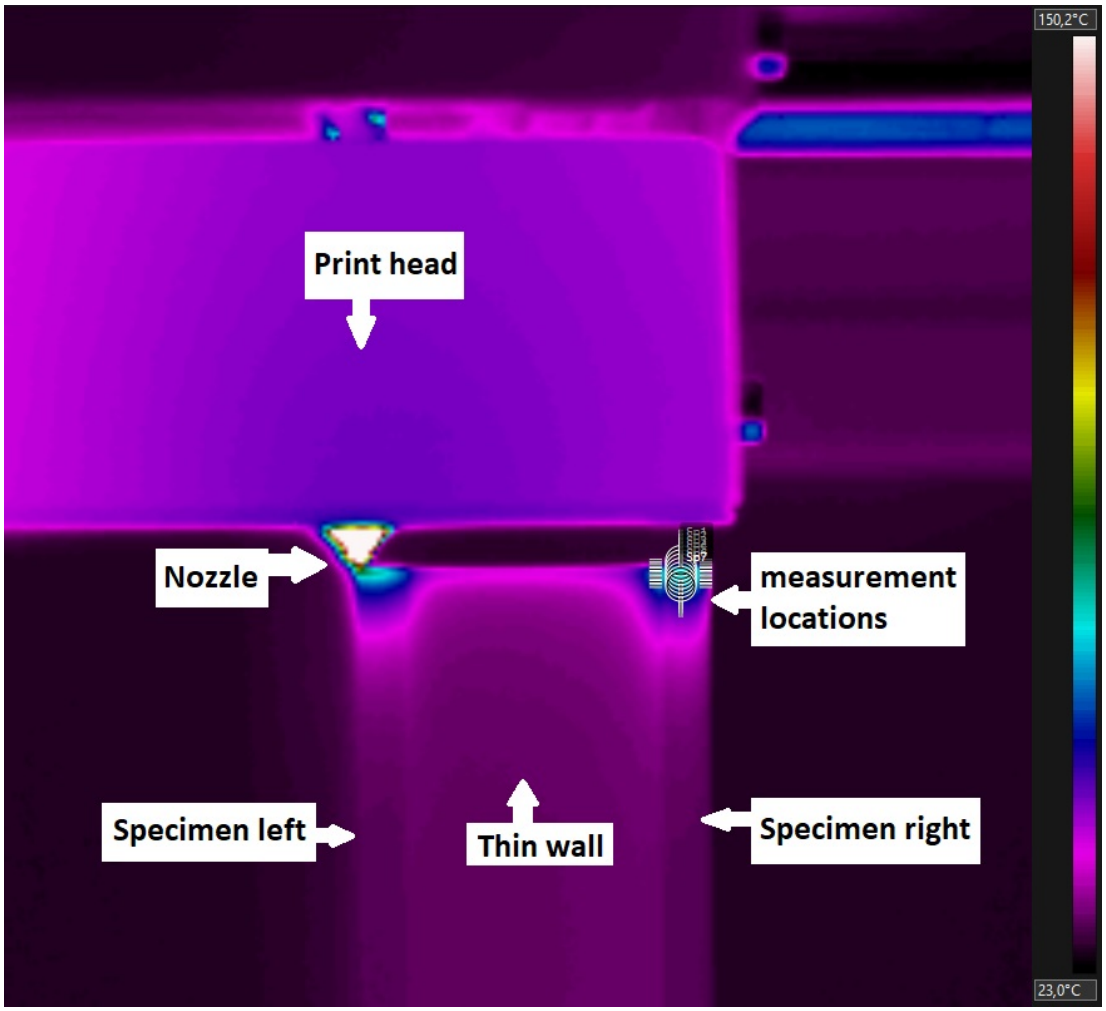

Figure 5.13: IR recording of a front view of the printing process of a tensile specimen as shown in figure 5.5. The locations at which temperature recordings are indicated with crosshairs.

Firstly, the time needed to print one layer was determined using a recording consisting of 120 seconds in which 18 layers are deposited. This results in a printing time per layer of roughly 7

seconds. As a result it takes roughly 17,5 seconds to deposit 2,5 layer. The Digimat simulation states that a single layer requires 4 seconds of printing time, which equals 2,5 layers requiring 10 seconds. This was used to scale the time-temperature data by dividing the time by 1,75. This was then used as the data representing the first 10 seconds of printing as shown in figure 6.5. All following decades were constructed in a similar manner using subsequent measuring locations as indicated in figure 5.13.

5.4.7 Inspecting sample void content and resulting meso-structure

During this research two methods are used to inspect the meso-structure and void content of 3D-printed specimens. Firstly optical microscopy is used in order to evaluate the void content of the fracture surfaces of tensile specimens. Secondly micro Computed Tomography (CT) is used to non destructively determine the void content throughout tested DCB samples. Images obtained with both optical microscopy and micro CT have been processed and analyzed using ImageJ v1.52 image processing software.

For the optical microscopy a digital microscope allowing up to 250x magnification with a resolution of up to 640 x 480 pixels was used. This allowed for the quick evaluation of the fracture surfaces of all tested tensile specimens. For each tensile specimen the fracture surface showing the highest void content has been included in the measurements as this is expected to be the limiting value.

A micro CT scanner is used in order to evaluate the void content and overall meso-structure in the tested DCB samples. For this research a Phoenix Nanotom 180NF has been used. The images were captured at 70 kV and 240 μA. For each sample images were collected over 360°(providing up to 1440 images). A resolution of 2284 x 2304 pixels was achieved. Timing was set at 500 ms per image.

Due to the time required for processing obtained micro CT data a choice was made to scan three samples. Each scanned sample was printed at a different T_{env} value in order to observe differences in meso-structure and void content and/or geometry between the respective temperatures. A reference sample was selected which was printed at room temperature. Secondly a sample printed at the highest T_{env} achieved was inspected. Finally a sample was selected at $T_{env} = T_g - 45$ °C as this provided intermediate results when considering G_{1c} values (see figure 6.8). From these T_{env} batches the sample with G_{1c} values closest to the average at the respective T_{env} was chosen.

Results obtained with the CT scans are used quantitatively to determine the effective surface area of tested samples. This is used to determine the actual interlayer fracture toughness.

Chapter 6

Results

This chapter shows and describes the results obtained by performing the simulations and experiments as described in chapter 5. Firstly, differential scanning calorimetry (DSC) measurements of filament material are presented. From this T_g and the temperature related print settings are determined. Subsequently, the time-temperature graphs obtained with simulations using Digimat AM are presented. These are followed by IR images captured for the verification of these simulations. Following this, the results obtained by mechanical testing of the printed samples are presented. Finally, this section presents the observed meso-structure measured at different T_{env} values.

6.1 DSC Results

The glass transition temperatures (T_g) of a selection of materials has been determined using differential scanning calorimetry (DSC). Besides the determination of T_g, the DSC measurements are also used to make observations regarding temperatures to potentially avoid during printing. This was done with the aim of providing consistent results without additional temperature related effects besides the reptation process.

Figure 6.1 shows the heat-temperature curve obtained for the PETG filament used for the manufacturing of the mechanical test specimens used in this research. For all materials inspected using DSC the T_g was determined using ISO 11357-2 [51]. This standard takes T_g as the temperature at the inflexion point of the exothermic dip indicating the glass transition point. This in contrast with determining T_g as the onset of glass transition temperature. It is important to consider that T_g generally speaking indicates a small range of temperatures in which the effects described in section 3.1 occur. Thus considering the midpoint provides a better indication of the temperature at which these effects are relevant, but effects may, partly, occur within a ± 4 °C interval.

The extruder nozzle temperature was decided upon based on considering the data provided by the filament manufacturer [5] and verifying this using the DSC curve in figure 6.1. As a result it has been decided to use the maximum temperature advised by the manufacturer as this is expected to benefit weld bond healing [11][84]. This temperature avoids the small exothermic peak that can be observed on the right of the printing temperature as indicated in figure 6.1. Such peaks often indicate crystallization or out-gassing of specific compounds in the polymer. As a result it is generally advisable to avoid such peaks, unless crystallization is a desired effect as is the case with many semi-crystalline polymers. As PETG is a mostly amorphous polymer

and considering that this is a desired property of the material as explained in section 5.1.1, printing temperature was set at 225 °C.

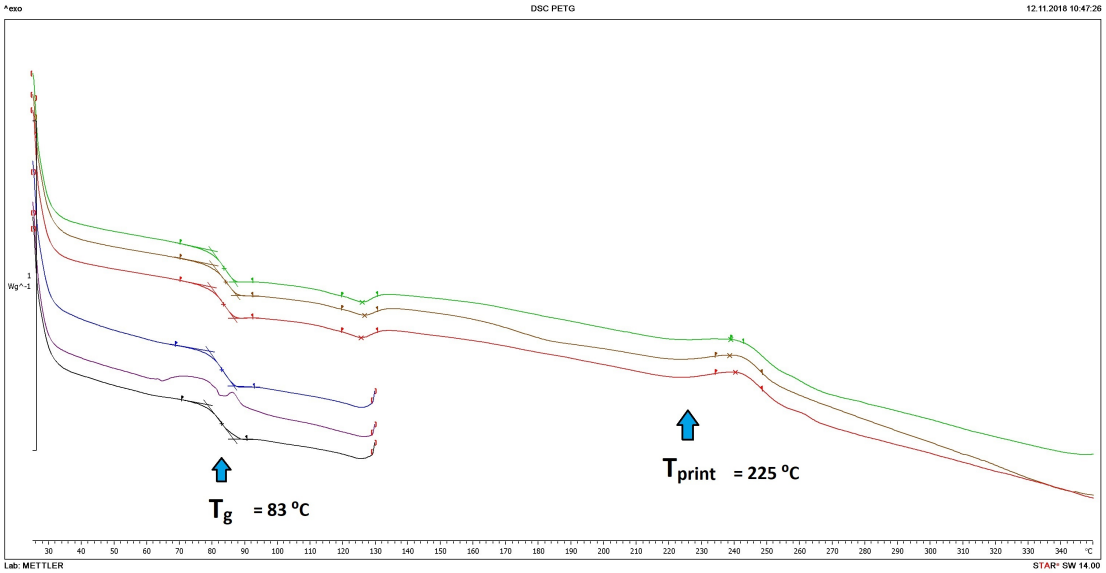

Figure 6.1: DSC measurement of PETG showing T_g at ≈ 83 °C and a minor endothermic crystallization peak at ≈ 240 °C.

For more information on the working principles behind DSC measurements, and how data obtained with a DSC can be interpreted, the reader is referred to section 3.1.1. Additional DSC curves of the other materials tested are included in appendix B for reference. The glass transition temperatures and printing temperatures for these materials are determined similarly to those of PETG described above. Except for PETG these filament materials have eventually not been used in this research as elaborately described in section 5.1. However the T_g and extruder temperature are included in table 6.1 to provide a complete overview. These properties have been determined in a similar manner as presented above for PETG.

Table 6.1: Glass transition - and Print temperatures as determined from DSC measurements

	T_g [°C]	Extruder nozzle temperature [°C]
PLA	70	190
PETG	84	225
ABS	112	230
Nylon PA 12 (STYX)	133	270

6.2 Simulated time-temperature curves

The Digimat AM software package has been used to obtain an indication of the temperature history of objects produced using FFF. As described in more detail in section 5.4.2, this software makes it possible to obtain simulated time-temperature plots of FFF, and SLS, 3D-printing methods. Assumptions made in order to obtain the simulated results presented in this section are discussed in section 5.4.3.

The Digimat AM simulations are run for the same range of T_{env} values used for printing the test specimens. For each T_{env} and print speed combination three measurement points are considered. These measurement locations are specified in figure 5.12. Figures 6.2 and 6.3 show

the temperature history of these three measurement locations at respectively the minimum and maximum T_{env} value considered in this research.

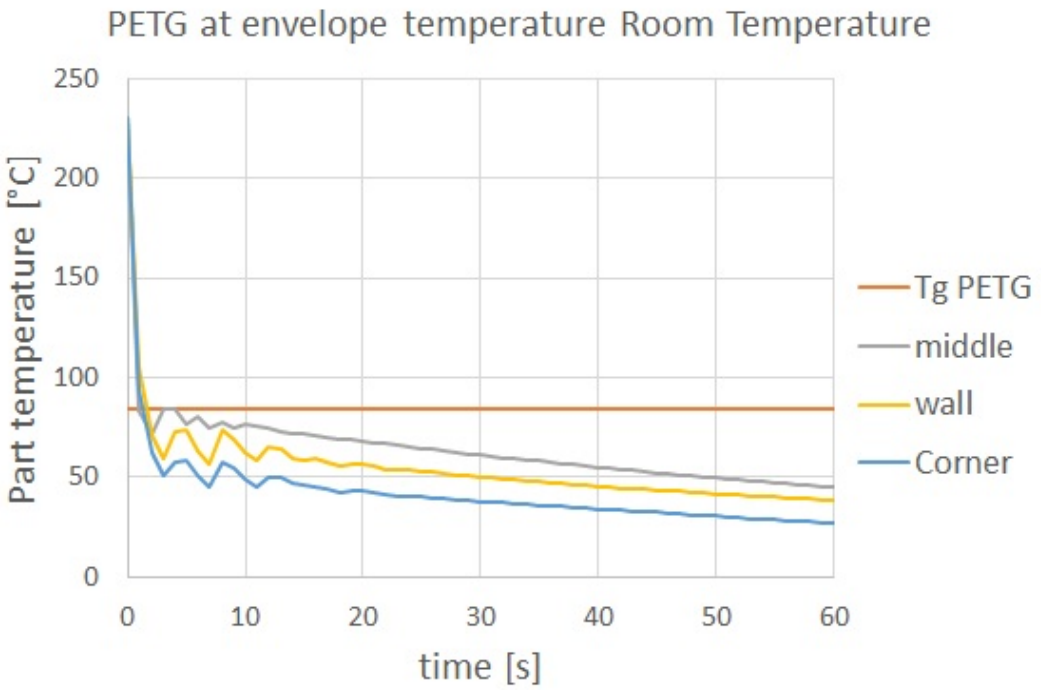

Figure 6.2: Graph showing time-temperature curves obtained from Digimat AM simulating PETG printed with a nozzle temperature of 225 °C at an envelope temperature of 23 °C.

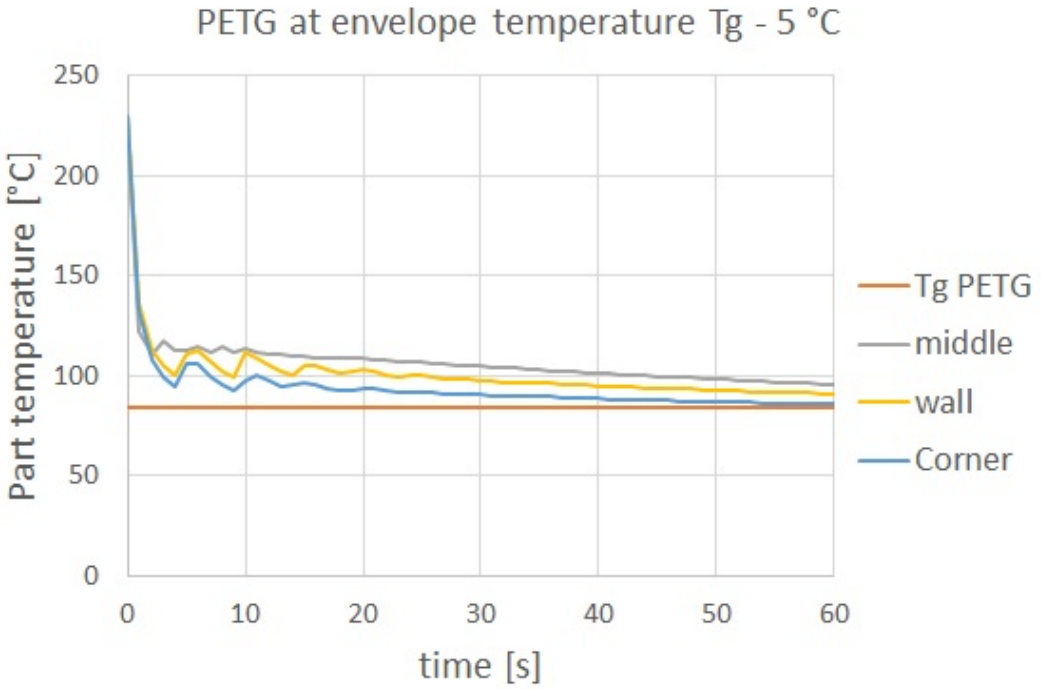

Figure 6.3: Graph showing time-temperature curves obtained from Digimat AM simulating PETG printed with a nozzle temperature of 225 °C at an envelope temperature of 79 °C.

Figure 6.4 shows the collected curves for measurements for all simulated T_{env} values taken at the middle nodes. Setting a higher envelope temperature resulted in simulations predicting the specimens residing a significantly longer time above glass transition temperature of the material. Indeed when comparing simulations run for an envelope temperature at room temperature and $T_g - 5$ °C, an increase from less than 1 to over 60 seconds spent above T_g can be observed. This 60 fold increase has been measured at the corner node, which cools down significantly faster than nodes in the middle of the sample as indicated by figures 6.2 and 6.3. The corner node is considered limiting because weak interlayer bonding at the corners is likely to result in crack formation at that location. This may lead to the sample failing prematurely.

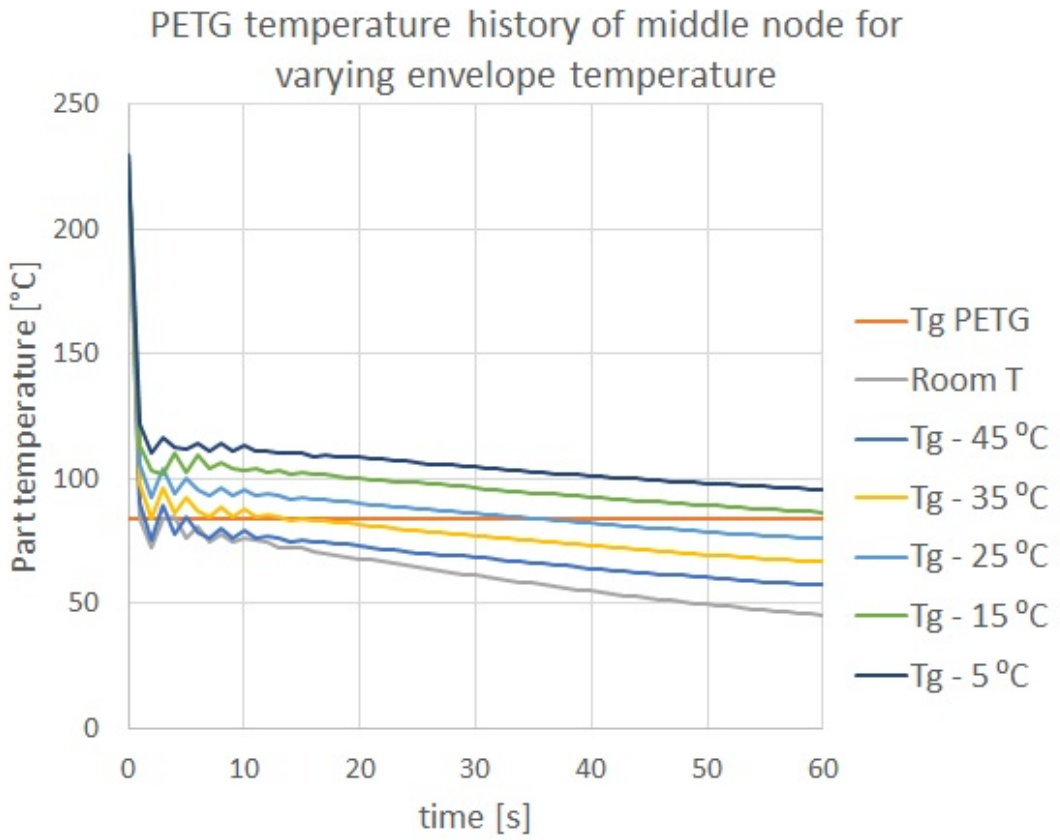

Figure 6.4: Graph showing time-temperature curves obtained from Digimat AM simulating PETG printed with a nozzle temperature of 225 °C for a range of T_{env} values. Measurements have all been obtained from nodes in the middle of the sample as specified in figure 5.12.

6.3 Time-temperature curves obtained using IR imaging

IR imaging has been used to verify the time-temperature curves obtained with Digimat AM. Figure 5.13 shows a still of the IR recording used to make the graph presented in figure 6.5. Figure 5.13 is included to give a qualitative indication of the temperature distribution within a sample during printing. Additionally the points at which temperatures have been measured are included in this image. The data obtained with these measurements is included in figure 6.5. This figure shows the combined time-temperature curves of the temperatures measured for these points.

In order to compare this curve with the simulated data the curves are plotted in the same graph. The curve measured using IR imaging is scaled to show equal print times per layer as the simulated time-temperature history. How this graph was constructed is described in section 5.4.6.

It can be seen that the curve constructed using IR, which was measured at T_{env} = room temperature, follows a similar decrease in temperature with time as the curves simulated with Digimat. There is however a significant ΔT along the entirety of the curve. This results in the curve obtained with IR imaging constantly showing a temperature around 20 °C higher than the Digimat AM simulation run for the same T_{env} suggest.

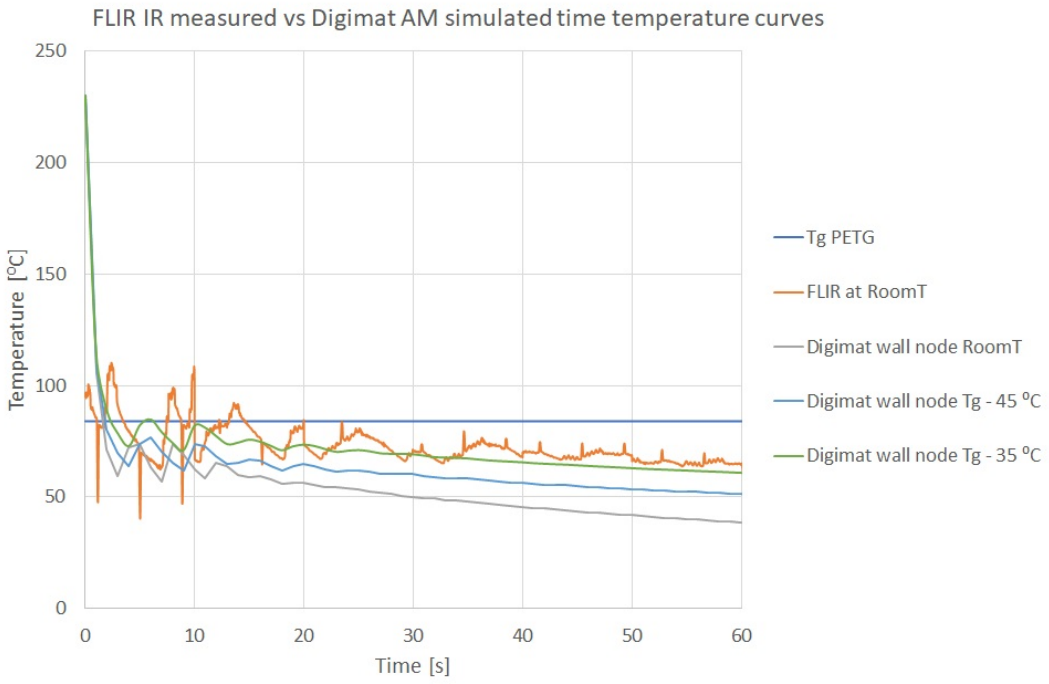

Figure 6.5: Graph showing the time-temperature curve constructed using measurements made with the FLIR IR camera along with time-temperature curves obtained using Digimat AM up till $T_g - 35°C$.

IR imaging of the sample during printing showed that the air directly surrounding the sample heated up significantly during printing, showing a gradual decrease in temperature moving away from the printed sample. This decrease in temperature reached a steady state at $1mm$ from the sample. This resulted in the sample reaching a steady state temperature at roughly 33 °C, which is 10 °C above T_{env} at which measurements were made.

6.4 Double cantilevered beam test results

In this section the results obtained by testing double cantilevered beam (DCB) samples are presented. Firstly the sample during testing and raw data, as given by the testing software, are presented. Subsequently the energy release rate G_{1c} as determined from this data is presented. This data is also presented calculated according to modified beam theory (MBT).

6.4.1 Crack propagation in printed DCB samples

Figure 6.6 shows a representative DCB sample during testing. In this figure it can clearly be seen that the crack propagates along a straight line down the center of the specimen. This crack is initiated in the area specified by the pre-crack printed into the sample. This pre-crack has been indicated in figure 5.1, which showed DCB sample dimensions. Further inspection of figure 6.6 indicates that the crack propagates neatly in between two printed layers. Visual inspection of the sample after removing it from the testing machine showed no significant plastic deformation occurring in the arms of the sample.

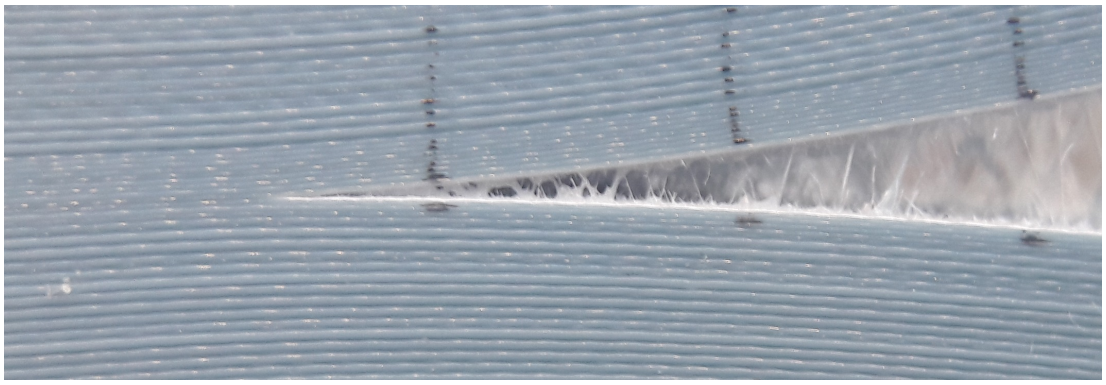

Figure 6.6: Figure showing the crack propagating in between printed layers, showing that samples used measure interlayer properties.

6.4.2 Load displacement curves obtained with DCB samples

Figure 6.7 shows two representative load-displacement (P-δ) curves. One for a sample printed at the benchmark T_{env} value (room temperature) and one for a sample printed at maximum T_{env} ($T_g - 15$ °C). For both curves the 5 %-offset line has also been included, which is required for the determination of the critical energy release rate (G_{1c}) as has been discussed in section 3.4.2. The sample printed at higher T_{env} showed both an increase in maximum load and maximum displacement of up to respectively 60 % and 40 %.

Upon unloading the samples, for both T_{env} values, a force is measured which is being exerted by the sample on the load cell of the Zwick/Roell Materials testing machine. This force increases with roughly 50 % when comparing these values for both curves.

6.4.3 Energy release rate values of DCB samples

Figure 6.8 shows the initially obtained G_{1c}, without modified beam theory (MBT), values plotted against the measured T_{env}. The names in the legenda indicate the desired T_{env} values. As was indicated in table 5.1, 5 DCB samples have been printed and tested for each T_{env} value. As such the data points in figure 6.8 each indicate the average and standard deviation values of 5 samples. In-situ measurements using an external thermocouple (as indicated in figure 5.10) showed there was some variation in T_{env} values during printing. These deviations in T_{env} are indicated in figure 6.8 by the horizontal error bars. Vertical error bars indicate the standard deviation of the measured interlayer fracture toughness. The data in table 6.2 and 6.3 are also based upon data obtained with the same 5 samples per T_{env} value.

Using the values presented in table 6.2 an increase of 109 % in G_{1c} is observed when comparing DCB samples printed at T_{env} = room temperature = 23 °C and $T_{env} = T_g - 15$ °C = 69

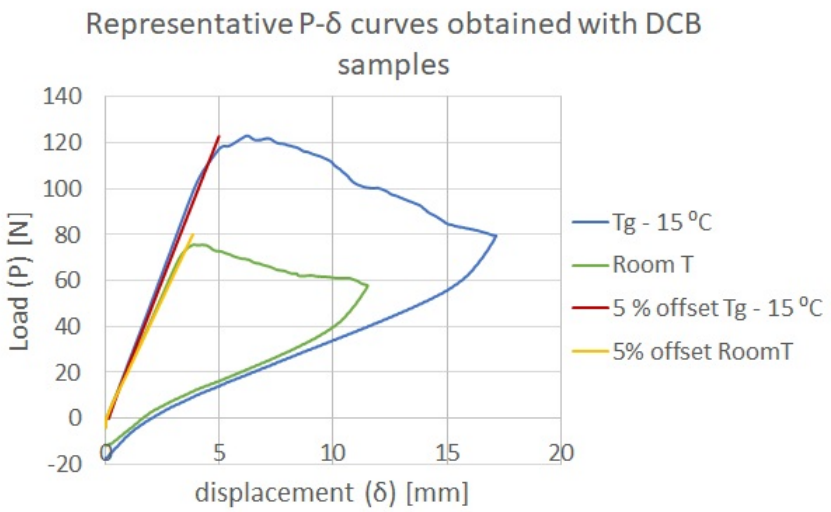

Figure 6.7: Representative curves of the P-δ curves obtained with printed DCB samples.

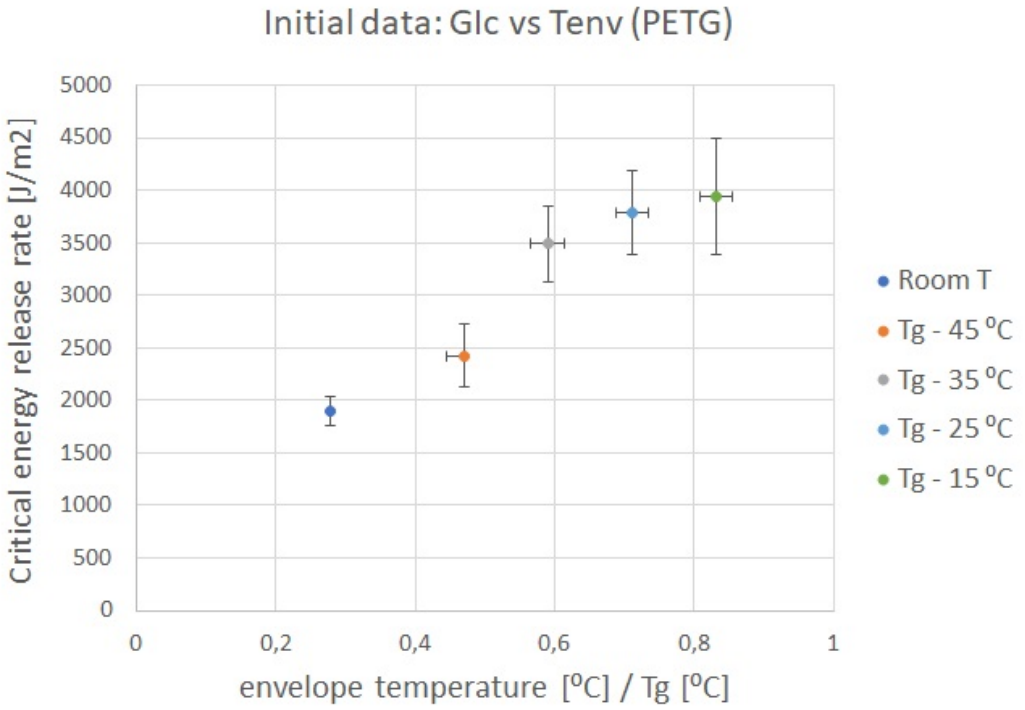

Figure 6.8: Initial results from DCB tests on PETG printed specimens.

°C. Additionally, from this table it is observed that G_{1c} data increases most significantly in the step from $T_g - 45$ °C to T_g - 35 °C. At higher T_{env} values an increase in G_{1c} is also observed, however the percentual increase appears to taper off.

Table 6.2: Initial data obtained with DCB samples along with the increase in percentage *w.r.t.* G_{1c} measured for samples at the previous T_{env}.

Tenv [°C]	23	39	49	59	69
G1c [J/m^2]	1,89e3	2,43e3	3,49e3	3,79e3	3,95e3
Increase from previous temperature [%]	-	13,5	27,0	7,6	4,0

Using the raw data obtained from DCB tests, G_{1c} has been calculated according to the modified beam theory (MBT) method as described in ASTM D5528 [15] and elaborated upon in section 3.4.2. The G_{1c} values obtained using MBT are significantly lower than the initial data, showing a decrease of up to roughly 43 %. In order to further inspect the possible influence of using this method, normalized values are presented in table 6.3 for both the initial G_{1c} values as well as those determined using MBT. Values for both the initial G_{1c} data and those determined using MBT are normalized by dividing the respective average G_{1c} values by the maximum average G_{1c} value obtained with the same method. This was decided upon due to the absence of a bulk G_{1c} value for the material. Comparing the normalized values determined both with and without MBT, as presented in table 6.3, does not show significant differences between the values obtained initially and those determined using MBT.

Table 6.3: Initial G1c data and G1c calculated using modified beam theory along respective standard deviations. Also included are normalized values for both initial and MBT values.

T_{env} [°C]	**23**	**39**	**49**	**59**	**69**
G_{1c} $[J/m^2]$	1,89e3	2,43e3	3,49e3	3,79e3	3,95e3
G_{1c} MBT $[J/m^2]$	1,09e3	1,42e3	2,00e3	2,19e3	2,27e3
G_{1c} standard deviation $[J/m^2]$	1,40e2	2,93e2	3,62e2	3,99e2	5,51e2
G_{1c} MBT standard deviation $[J/m^2]$	1,55e2	1,56e2	2,78e2	1,96e2	2,67e2
G_{1c}/G_{1cmax} [-] (normalized)	0,48	0,61	0,88	0,96	1
G_{1c}/G_{1cmax} MBT [-] (normalized)	0,48	0,63	0,88	0,97	1

Table 6.3 also shows the standard deviations for G_{1c} values obtained at each T_{env}. These are presented both for initial G_{1c} values and those determined using MBT. When these standard deviations are compared, it is seen that overall these vary between 7,4 % and 14,3 %. No distinct difference in trend has been found comparing standard deviations for initial G_{1c} values and those determined using MBT.

6.5 Tensile testing results

In this section representative stress-strain curves are presented, which have been obtained for the tensile specimens tested during this research. Results obtained from inspecting the fracture surfaces of these specimens are also presented. Secondly the ultimate tensile strength (UTS) plotted against T_{env} is reported. This is presented both as initially measured and corrected for the effective surface area. Additionally the tensile toughness, as determined using the stress-strain curves, is presented as obtained for samples printed at the respective T_{env} values.

6.5.1 Stress strain curves obtained with tensile samples

Figure 6.9 shows representative stress strain curves obtained for tensile samples printed at T_{env} = room temperature and $T_{env} = T_g - 25$ °C. $T_g - 25$ °C was decided upon due to samples from this set showing better results than $T_g - 15$ °C as is presented in figure 6.13. This figure also shows that values obtained with the $T_g - 15$ °C data set still provide values which are significantly higher than the data set acquired at room temperature.

In figure 6.9 it can clearly be seen that the representative sample printed at higher T_{env} shows a significantly higher UTS than the representative sample printed at room temperature. Additionally the strain at break also shows a significant increase. Both samples only show a linear elastic region before failing critically, indicating brittle failure of the tensile specimens.

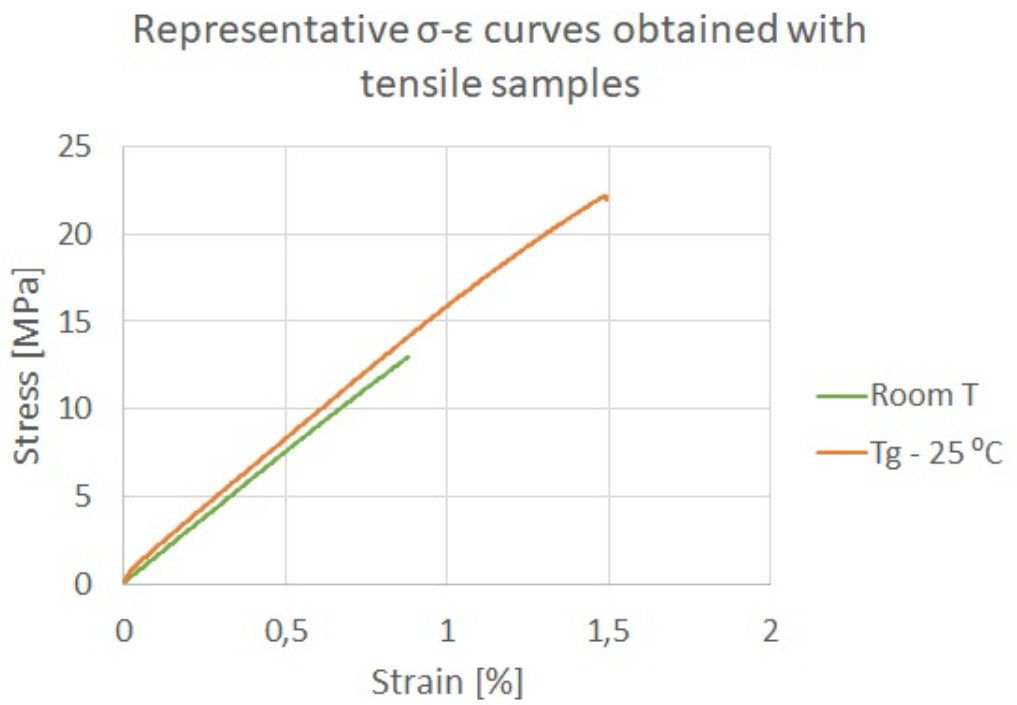

Figure 6.9: Representative curves of the σ-ϵ curves obtained with printed tensile samples.

These samples have been selected as they show UTS values closest to the average value obtained for the respective sample set.

6.5.2 Fracture surfaces of tensile specimens

Indeed visual inspection of the samples and fracture surfaces as seen in figures 6.10 and 6.11 shows no necking occured, further indicating brittle failure. At the same time only minimal crazing is observed verifying that samples indeed failed critically before significant plastic deformation could occur.

While an effort has been made to print samples to be completely solid, as described in section 5.3.5, figures 6.10 and 6.11 show that this was not completely successful. Samples show varying degrees of void content even within a single sample set (*i.e.* printed at the same target T_{env} values).

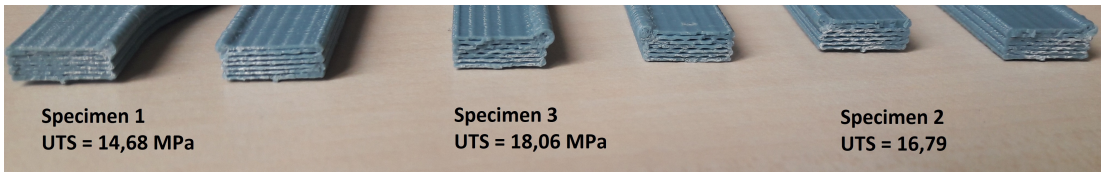

Figure 6.10: Image showing tensile specimens 1 through 3 of the sample set printed at $T_{env} = T_g - 15°C$. These are less solid and show lower UTS values.

Sample fracture surfaces have been inspected using optical microscopy. ImageJ analyzing software has been used in order to quantify the effective surface area. To give an impression of the varying print quality, the inspected cross sections which presented the extreme values of the measured void area percentages are included in figure 6.12. Figure 6.12 shows both the images

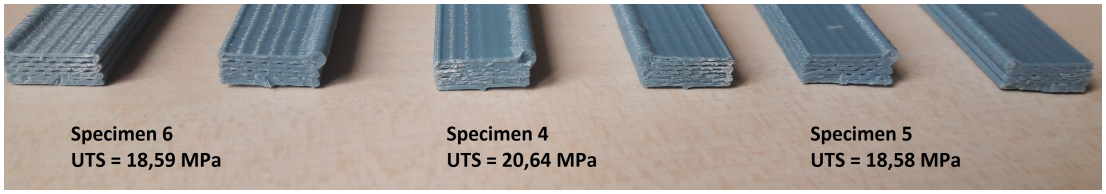

Figure 6.11: Image showing tensile specimens 4 through 6 of the sample set printed at $T_{env} = T_g - 15°C$. These are more solid and show higher UTS values.

obtained with optical microscopy and the respective images after processing in ImageJ. This processing allowed the measurement of the effective surface area percentage. The black squares in the bottom figures indicate the area in which the measurements are collected. An effort has been made to measure an area as large as possible without including measuring data outside the boundaries of the tensile specimens. Table 6.4 shows the average values and standard deviations of measured void area percentages for all tensile samples.

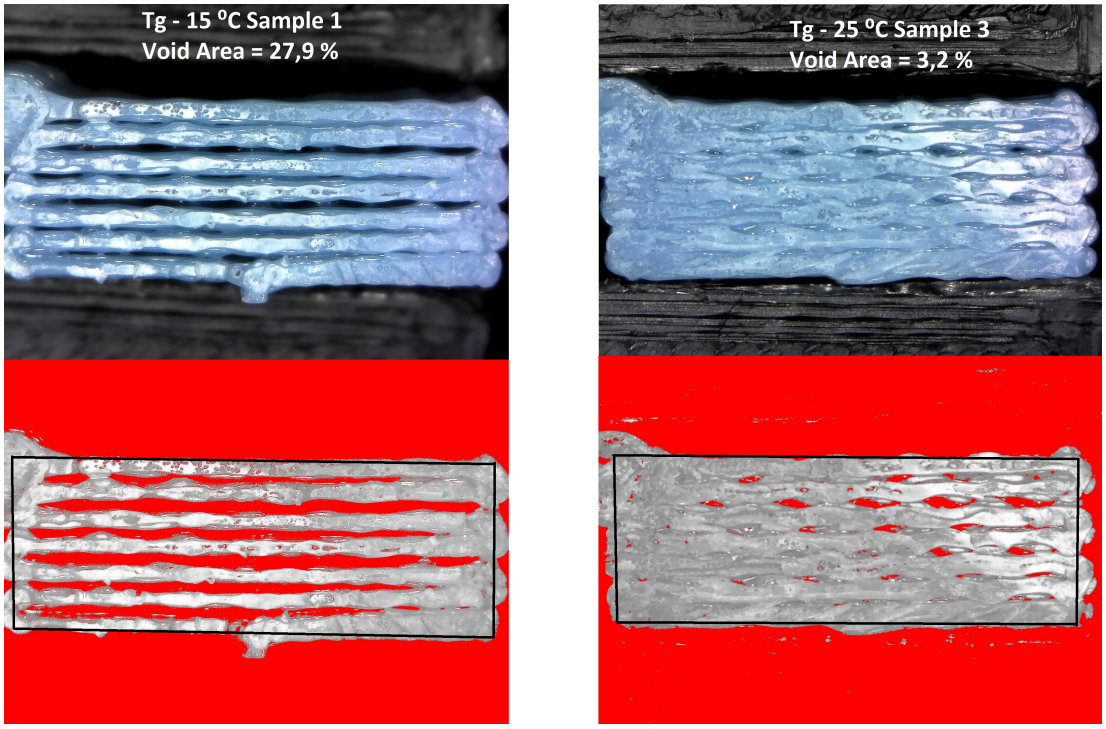

Figure 6.12: Image showing planes between which the cross sections of the DCB sample are recorded using the micro CT images.

Table 6.4: Table showing void area % determined from optical microscopy for each sample set.

Target Tenv [°C]	RoomT	Tg - 45 °C	Tg -35 °C	Tg - 25 °C	Tg - 15 °C
Average measured Tenv [°C]	23	39	42	59	63
Average void area [%]	10,3	12,2	20,2	7,1	16,6
Standard Deviation void area [%]	3,4	4,4	3,1	3,7	9,2

6.5.3 Ultimate tensile strength of tensile specimens

In figure 6.13 UTS is plotted against the respective measured T_{env} values. Contrary to G_{1c} a bulk value for UTS of PETG was available. Average UTS values have therefore been normalized

for UTS as reported in the data-sheet [5]. This presents us with an impression of how the anisotropy of the mechanical properties of printed samples decreased with increasing T_{env} values. T_{env} values are normalized against T_g as presented in table 6.1.

As was the case for the graph presenting DCB results, the names of the curves indicate desired T_{env} values as specified in table 5.1. The data points indicate the UTS average and standard deviation of 6 tested samples as shown in table 5.1. The error margins in the direction of the temperature axis indicate the temperature fluctuations within the print room during printing.

It can be seen that most of the data points in figure 6.13 are not at the desired envelope temperatures. This was due to the print room not being capable of reaching the T_{env} values as set in table 5.1. Why this occured, as well as the solution to this problem have been described in section 5.3.7. Lower T_{env} values could be achieved near the top printing during the printing of tensile specimens compared to DCB samples. This can be understood by considering that the primary heat source, the print bed, was considerably further removed from the currently printing layer for a large part of the printing of the tensile samples.

It can clearly be seen that samples printed at temperatures closer to T_g provided higher UTS values compared to samples printed at lower T_{env} values. An increase of up to 50 % in ultimate tensile strength is measured.

It is worth noting that compared with the DCB measurements, the increase in properties for the tensile specimens with increased T_{env} appears to be less consistent. For example the average values measured for $T_g - 35$ °C and $T_g - 15$ °C show a distinct drop in tensile properties compared with the precedent T_{env} values.

As presented in section 6.5.2 the fracture surfaces of tested tensile specimens showed that samples did not print completely solid. As a result a spread in effective surface area was measured from 72,1 % to 96,8 % was measured as can be seen in figure 6.12. To compensate for this effect UTS values have been corrected for the effective surface area (η) as presented in equation 6.1. The results are shown in table 6.5, comparing the UTS values corrected for effective surface area with the initially obtained values. The corrected values show that indeed average UTS at $T_g - 15$ °C is now more in line with the expected values. The average UTS for $T_g - 35$ °C still shows a significant unexpected drop in value compared with the previous T_{env} value.

$$UTS = \frac{F}{\eta A}. \tag{6.1}$$

Table 6.5: Table showing average values and standard deviations for initial UTS values and UTS values corrected for the effective surface area.

Target Tenv [°C]	Room T	Tg - 45 °C	Tg -35 °C	Tg - 25 °C	Tg - 15 °C
Average measured Tenv [°C]	23	39	42	59	63
Average initial UTS [MPa]	13,7	13,0	10,4	19,9	17,9
Standard Deviation initial UTS [MPa]	2,2	2,0	0,8	2,3	2,0
Average actual UTS [MPa]	15,3	14,8	13,0	21,4	21,5
Standard Deviation actual UTS [MPa]	2,1	2,2	0,8	1,8	1,4

6.5.4 Tensile toughness of tensile specimens

The tensile toughness (U_T) of a material can be calculated by taking the integral of stress-strain curve as mentioned in section 5.2.3. This is representative for the amount of strain energy a

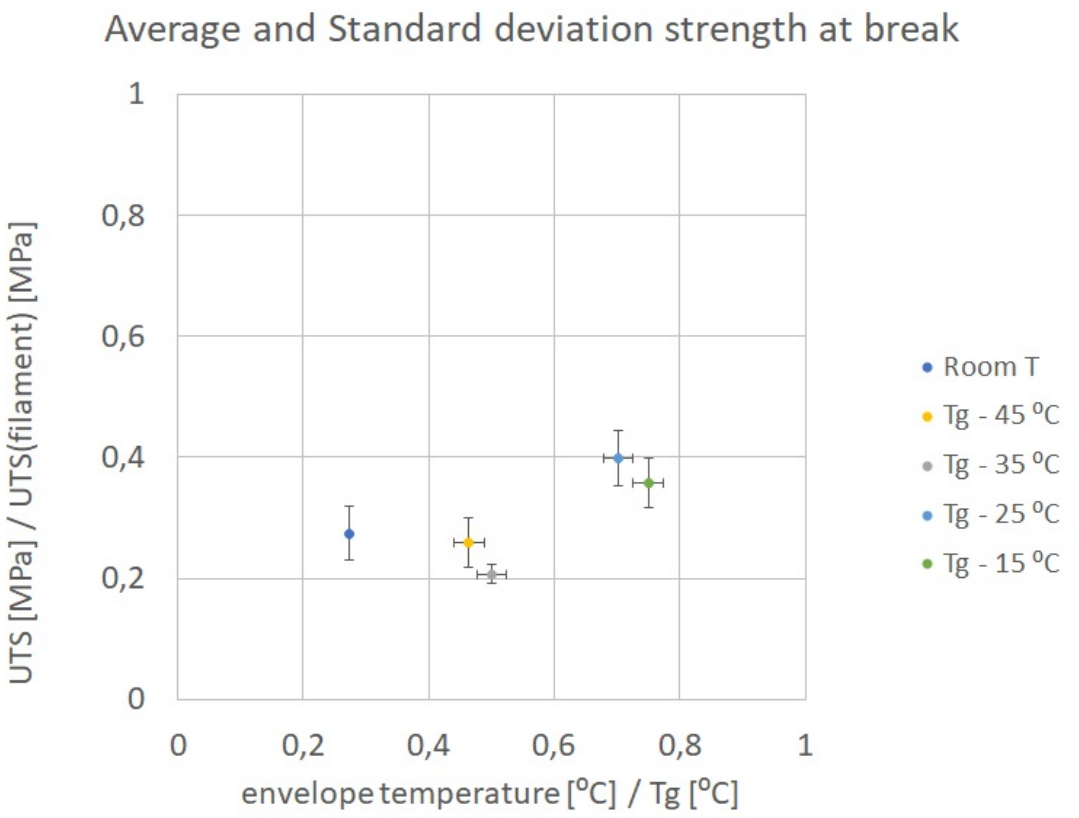

Figure 6.13: Ultimate tensile strength as obtained from tensile testing data for ISO 527-2 [53] samples printed in Z-direction printed at specific T_{env} values.

sample loaded in tension can absorb before failure. The U_T values determined this way are presented in figure 6.14.

If the U_T at T_{env} = room temperature = $23°C$ and maximum toughness at $T_{env} \approx 60°C$ (the value for $T_g - 25°C$) are compared an increase in average U_T of up to 106% is obtained. Standard deviations for U_T show values up to 36%. This standard deviation is significantly higher than those measured for G_{1c} and UTS. This can be explained by the fact that U_T is calculated using both stress and strain data obtained from tensile specimens. These show a standard deviation of respectively up to 16 % and 22 %. Calculating U_T for each sample and subsequently determining the average and standard deviation values for these results in yet higher standard deviation values.

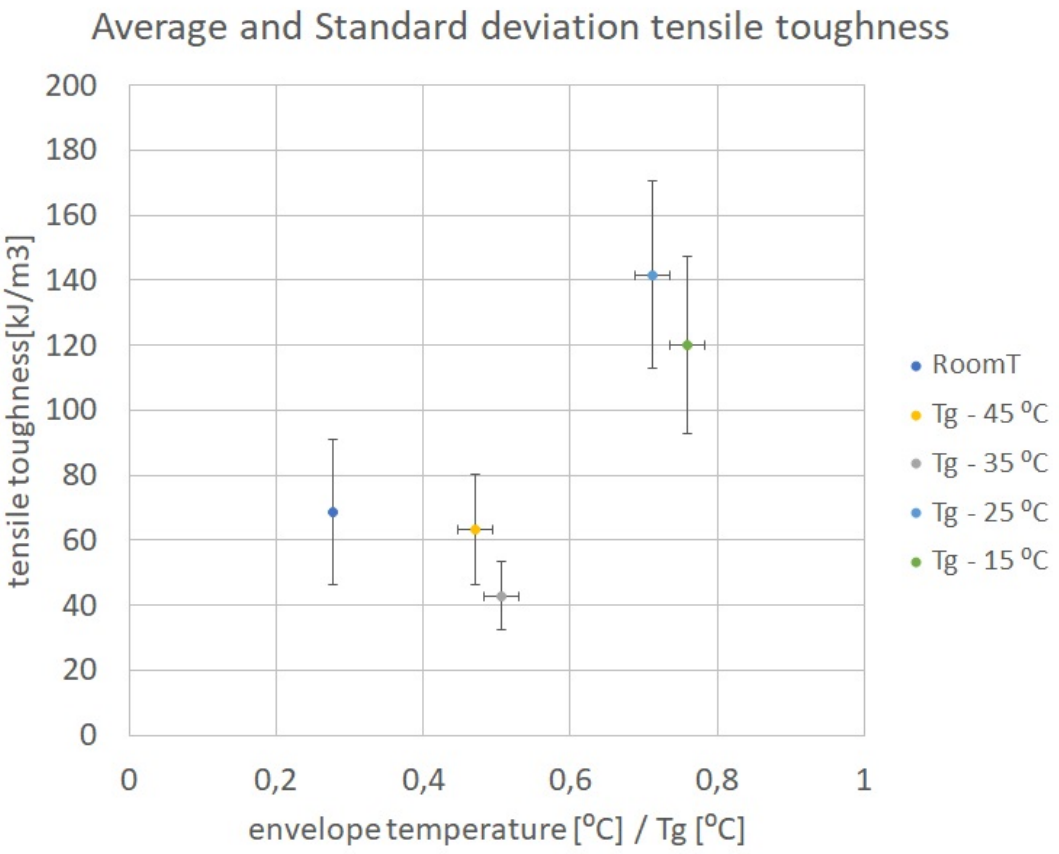

Figure 6.14: Tensile toughness (U_T) as obtained from tensile testing data for ISO 527-2 [53] samples printed in Z-direction printed at specific T_{env} values.

6.6 Micro CT results

In this section the results obtained using a micro computed tomography (CT) scanner are presented. This scanner is used to obtain images of tested DCB samples in an area just beyond the propagated crack. To facilitate interpretation of the results presented in this section, a figure showing the location at which the micro CT images are recorded is included in figure 6.15. The coordinate system of this figure corresponds with the coordinate system presented in figure 6.16. This means that the print roads go into the page and the bottom of the figure is the location of the build plate.

In table 6.6, quantitative data is presented in the form of the volume percentages of air measured in the samples printed at different T_{env} values. This has been determined by measuring the percentage of area within the sample consisting of air. In order to make these measurements, the cross sections made using micro CT have been imported in ImageJ. A macro using the threshold function and a predefined measurement area was used to measure the area % of air in the cross section.

These measurements have been limited to the center third of the sample with respect to the z-axis. This measurement location is indicated by the black square in the right frame in figure 6.16. This has been done in order to obtain a more relevant average considering that the crack propagates within this area of the sample. Due to the sample not being perfectly centered during scanning, the measurement area has a slight margin in the direction of the x-axis to

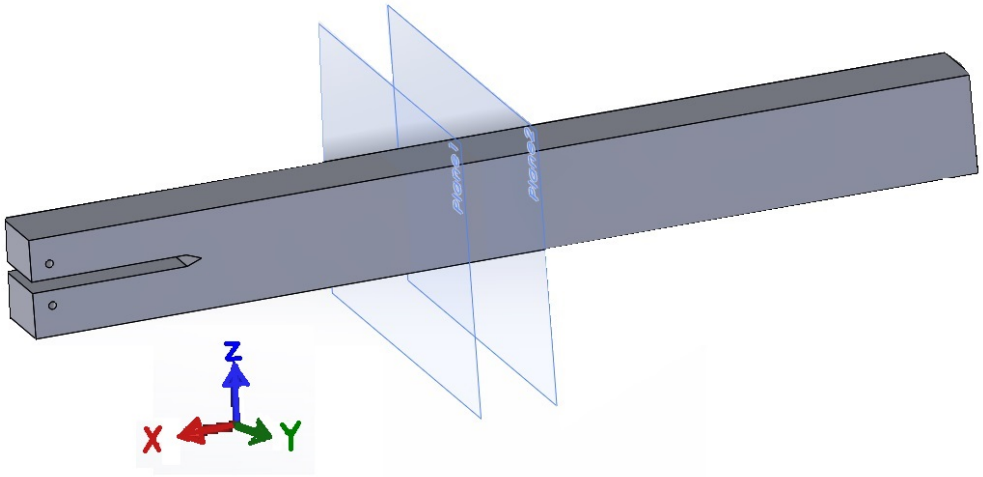

Figure 6.15: Image showing planes between which the cross sections of the DCB sample are recorded using the micro CT images.

ensure all measurements are located within the sample. Similar measurements have been made for all available cross sections of the respective samples. As a result an average and standard deviation of the percentage of air in the samples could be determined over roughly 1000 cross sections per sample.

As can be seen in table 6.6, across the roughly 1000 cross sections per sample, large variations have been measured considering maximal and minimal area percentage at the center of the cross section. Maximum and minimum values, as well as some randomly selected cross sections have been inspected by hand. This was done in order to ensure the validity of the automated measurements. For the sample printed at room temperature only the first 1000 images were considered. The reason for this being that in the final ≈ 150 cross sections, a large percentage of images was of lower quality. This made it impossible to distinguish between the air in the voids and the polymer itself. Thus no precise measurements could be made considering the void content in these 150 cross sections.

Table 6.6: Table showing area percentage of air measured in DCB samples inspected using micro CT imaging.

	RoomT	Tg-45 °C	Tg-15 °C
Average void area %	5,39	9,32	3,63
Standard deviation void area %	1,15	1,37	0,32
Maximal void area %	10,58	13,01	4,62
Minimal void area %	4,51	7,25	2,92

Besides calculating the area percentage of air within the samples, the cross sections were also used to measure the print road width and layer height of individual print roads. Layer height, measured in the z-direction, was found to be quite consistent showing values of around 0,1 mm as set in the slicer software. However when considering the print road width it becomes apparent that this varies significantly. This variance in road width has been determined by random sampling of 60 road widths equally spread across the $T_g - 45$ °C sample presented in figure 6.16. This showed an average print road width, measured in the y-direction, of 0,45 mm and standard deviation of $0,05$ mm while slicer settings had been set at a print road width of $0,48$ mm. This resulted in parts not being completely solid and voids coalescing in the z-direction (as indicated in figure 6.16). This was most apparent in the micro CT image for

the sample printed at $T_g - 45$ °C. This sample also showed the large average, minimum and maximum area percentage of air.

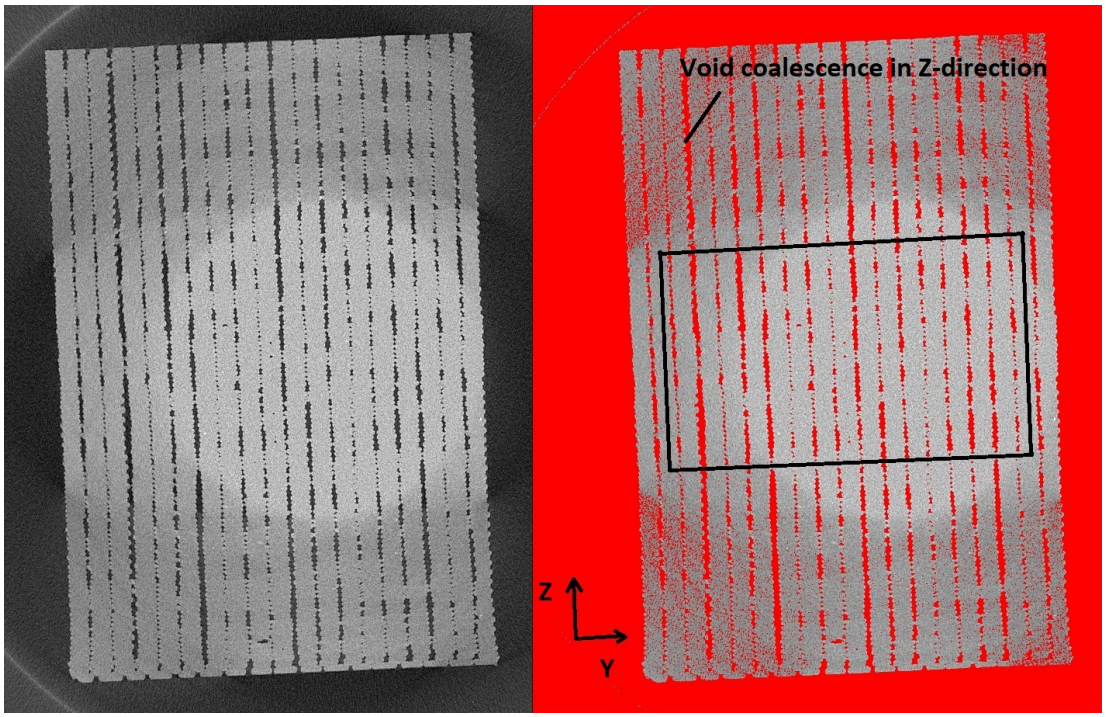

Figure 6.16: Micro CT images of sample printed at $T_{env} = T_g - 45°C$. The image on the left shows the original CT scan, the image on the right shows the same image with a threshold and measurement area set.

Finally the quantitative data obtained is used to correct the G_{1c} values obtained with the DCB testing using the effective surface area. The effective surface area is determined by inserting the effective surface area percentage (η) in equation 3.24. This results in the following equation

$$G_1 = \frac{3P\delta}{2\eta b(a + |\Delta|)}. \tag{6.2}$$

This is done only for the samples that were inspected using micro CT. The data obtained with correcting for the effective surface area is denoted as the actual interlayer fracture toughness. This has been calculated using the effective surface area with the G_{1c} value obtained for the respective sample. Results are presented in table 6.7.

Table 6.7: Table showing effective surface area and actual G_{1c} compensated for

	RoomT	Tg - 45 °C	Tg - 15 °C
Effective surface area % (η)	94,6	90,7	96,4
Measured G1c [J/m^2]	9,97e2	1,38e3	2,36e3
Actual G1c [J/m^2]	1,05e3	1,52e3	2,4e3

Chapter 7

Discussion

This chapter serves to discuss the results presented in chapter 6 and relate these results to the theory described in chapter 3. Firstly the temperature history of parts during printing is discussed. This is done by first relating the data obtained with simulations to measurements done with IR imaging. Subsequently the results obtained with DCB and tensile test samples are discussed. These are related to the time-temperature curves obtained with simulations. Finally the impact of the meso-structure on mechanical properties, as observed using micro CT scanning, is discussed.

7.1 Analyzing simulated and measured temperature histories of the printing process

Firstly, in this section the simulated time-temperature curves illustrating the temperature history of FFF produced samples during printing presented in section 6.2 are discussed. In order to verify these simulated time-temperature curves, IR imaging was used to record the temperature history of upright printed tensile specimens printed at room temperature. As stated in section 5.4.1, the temperature history during printing was simulated mainly due to IR imaging of samples printed at all T_{env} values was not possible during this research. Therefore IR images have only been recorded for a sample printed at room temperature. In this section the results obtained with IR imaging are discussed and related to simulated data.

7.1.1 The effect of increasing T_{env} in simulations

When inspecting the time-temperature curves in figure 6.2 and 6.3 a clear increase in the time a part spends above T_g during printing can be observed. Indeed it was shown in section 6.2 that this increases by a factor of 60. When considering figure 6.4 it can be seen that the ΔT of the part with respect to T_g also increases consistently with each step in T_{env} from $T_g - 45$ °C onwards. The initial step up from room temperature to $T_g - 45$ °C is not yet expected to result in significant increases in mechanical properties as the part does not spent a significant extra amount of time above T_g. The ΔT of the interlayer with respect to T_g also does not appear to increase for this step up in T_{env}.

Based on the simulations, the step from $T_g - 35°C$ to $T_g - 25$ °C is expected to yield the most significant increase in mechanical properties. This is due to this being the first step up in T_{env} resulting in the part spending more time above T_g, along with a ΔT with respect to T_g of

up to 15 °C. Considering the simulated curves presented in figure 6.4, each subsequent step up in T_{env} is then expected to show a further increase in mechanical properties. Eventually this is expected to lead to the respective bulk value being approached.

The theory as described by Wool *et al.* presented in section 3.1.3 suggests that the increase in properties is expected to taper off at longer weld times when bulk values are approached. In the case of FFF 3D-printing the weld time can be related to the time spent above T_g. This relation is described in more detail in section 7.3.3. These simulated curves are related to mechanical properties of printed samples in section 7.3.

7.1.2 Differences between measured and simulated time-temperature curves

As was mentioned in section 6.3, measured IR data consistently showed (up to 20 °C) higher temperatures compared with simulated data. This can partly be explained by the fact that simulations do not account for interaction between the part and the largely stagnant air surrounding the part. As no air, or other medium, is being forced past the printed object natural convection can be assumed. The air directly surrounding the part rises in temperature, creating a temperature buffer zone. This results in the part not reaching $T_{part} = T_{env}$. IR imaging showed that during printing the part is consistently at $T_{part} > 33$ °C. In contrast with this; in the simulation the temperature of the chamber is kept at 23 °C and no interaction with the part is considered. This results in the part cooling down to $T_{part} = T_{env} = 23$ °C. As a result the actual temperature during printing is more likely to resemble a simulation at higher T_{env}.

At room temperature T_{env} part temperatures are 10 °C higher than simulations suggest. Simulated results at $T_{env} = T_g - 45$ °C would then be expected to provide a time-temperature curve more closely resembling measured data. However, considering the time-temperature curve of $T_{env} = T_g - 45$ °C as it is included in figure 6.5 the simulated data still seems to underestimate the temperatures measured using IR imaging. It is likely the remaining discrepancy can, at least in part, be explained by the fact that simulations use specific heat capacity and thermal conduction data not specifically determined for PETG. This was shown in table 5.2 and elaborated upon in section 5.4.2.

Considering PETG has a lower specific heat capacity, less energy is required to raise the material's temperature. The higher thermal conductivity indicates that the material distributes heat through the sample more readily. As a result a larger zone affected by the bed and nozzle is expected. Indeed figure 6.5 shows a larger heat affected zone than simulations suggest. Measurements using ImageJ indicated that part temperatures reached a steady state at roughly 13 mm removed from L_p (see layer naming convention introduced in figure 3.11. This is at least 30 % larger than simulations suggest, as has been described in section 5.4.3.

Based upon these findings the simulated curves for all T_{env} values as presented in figure 6.4 are expected to quite significantly underestimate the temperature history of the samples during printing. This needs to be considered when evaluating the mechanical properties of samples printed with respect to the T_{env} at which they are printed.

7.2 Determining interlayer properties in FFF samples with mechanical testing

In this section the testing methods used for determining the interlayer mechanical properties in FFF produced samples are discussed. Firstly, the validity of using double cantilevered beam (DCB) samples for the determination of interlayer bond strength is discussed. Secondly, the tensile test stress strain curves and fracture surfaces are discussed.

7.2.1 Double cantilevered beam specimens

As presented in figure 6.6 the crack in the DCB samples used propagates in between printed layers. This indicates that it is indeed the interlayer energy release rate which is measured using this testing method. Some crazing, a concept discussed in section 3.4.3, does appear to occur in between printed layers. As these crazes limit the ductility of the material, the crack propagates in a mostly brittle manner. A slight degree of bridging of the crack occurs due to these crazes. These bridges deform in a plastic manner, resulting in the stretched white fibrils observed in figure 6.6. These can partly explain the small degree of plasticity observed in the load-displacement curves presented in figure 6.7.

This plasticity is indicated by the sample imposing a load upon the load cell of the testing machine after returning the sample to its initial displacement. It is interesting to observe that this load imposed by the sample increases a similar order of magnitude compared to the maximum on the samples at the respective T_{env} values.

Additionally when visually inspecting tested samples by placing them on a flat surface they indeed appear not to be entirely flush after testing. Overall the presence of this, minor, plastic deformation suggests that this may not be the ideal method for obtaining an absolute value for energy release rate value for PETG. However, for this research DCB is solely used to determine a relative increase in interlayer properties. For this purpose the method is clearly suited as the increase in plastic deformations are minimal and scale proportionally to the maximum load on the tested sample.

When considering the representative load displacement curves presented in figure 6.9, and comparing these with figure 3.23, it can be observed that the crack propagates in a stable manner. The curves obtained indeed show results similar to those in figure 3.23. Combining this with the minimal amount of plastic deformation observed during testing it has been concluded that results can be interpreted according to ASTM D5528 [15]. This method has been presented in section 3.4.2.

Finally, comparing the order of magnitude of the G_{1c} values obtained these indeed validate the maximum G_{1c} value presented in section 5.2.2, as suggested by literature [68]. Samples with dimensions as suggested in section 5.2.2 indeed lead to stable crack growth and minimal plastic deformation as observed in DCB samples during testing.

7.2.2 Tensile test specimens

It is interesting to note that tensile samples printed at higher T_{env}, which show higher UTS and strain consistently still show brittle stress strain curves. Representative stress-strain curves for tensile specimens have been presented in figure 6.9. The consistently brittle failure in tensile specimens, along with the 120 % elongation at break presented in the data sheet for the filament material [5], indicates that the weld bond is not yet at bulk strength and further healing might

be a distinct possibility. As a result it is expected that printing tensile specimens at T_{env} closer to T_g will lead to better results than those obtained during this research. Additionally, the printing process introduces stress concentrations at each layer, smoothing of the surface is expected to also contribute to increasing the elongation at break of the printed samples [74].

It is important to note that the exact manner of testing (*e.g.* print direction and print settings) are not specified on the datasheet. It is therefore assumed that this are the maximum achieved properties due to comparison with generic PETG properties [3].

Figures 6.10 and 6.11 also present visual confirmation that tested tensile samples exhibit brittle failure. The lack of necking indicates that no significant plastic deformation occurred before failure. Some crazing, a concept discussed in section 3.4.3, can be seen on parts of the fracture surfaces. These are likely the locations where failure first initiated followed by a rapid critical failure of the entire sample. Part of the fracture surface does not show crazing. This likely occurred as a result of increased localised stress leading to the molecular chains not having sufficient time to stretch between entanglements. As a result failure in the molecular chain occurred before the chain could be stretched and no crazing occurred prior to critical failure. The presence of crazing does indicate that molecular chains diffused into other layers, however no direct correlation based upon this can be made towards the degree of inter diffusion.

Figures 6.10 and 6.11 show that the fracture surfaces of the tensile specimens show a significant variation in void content even within a single sample set. Considering the UTS values associated with each fracture surface, an initial estimation suggests that samples that contain a larger surface fraction of voids exhibit lower UTS values. Especially samples showing long, connected voids appear to have lower UTS values. This is discussed more in section 7.4.1 which focuses on the effect of meso-structure on tensile specimens.

Additionally figures 6.10 and 6.11 show a recurring artifact of the printing process which is present in all printed tensile specimens. In an effort to obtain more solid specimens the extrusion multiplier (a printer setting determining the filament flow rate and specified in appendix A) needed to be set to a higher value. This provided the desired effect of printed parts becoming more solid. However, it also resulted in excess material extruding at the end of each printed layer. This lead to the introduction of these artefacts at the end and beginning of the printing routine of each layer. As these were present in all specimens this was accepted as a necessity in order to obtain more solid specimens. In the ideal case these artefacts would not be present and in further research additional effort should be made to avoid such artifacts.

7.3 Increased mechanical properties obtained by printing at higher T_{env}

This section starts with discussing the observed increase in mechanical properties for tested DCB samples at different T_{env} values. Subsequently, this increase in properties is related to the increased time spend above T_g due to increased T_{env}, as indicated by simulations and IR imaging. Finally, data obtained by performing tensile tests on samples printed at different T_{env} values is reviewed and similarities and discrepancies are discussed.

7.3.1 Increased G_{1c} for printing at higher T_{env}

The significant increase in average G_{1c} values of up to 109 % indicates that raising T_{env} to values close to T_g is a effective method of enhancing mechanical properties. While figure 6.8

along with tables 6.2 and 6.3 show a clear increase in mechanical properties for samples printed at higher T_{env} values, it is not possible to make a meaningful fit through the measured data. Due to the limitations imposed by the printer used, it was not possible to raise T_{env} enough to obtain a significant amount of data points to state with confidence that a bulk value was obtained. Standard deviations of up to 14,3 % allow for a large variation in line fit types, which resulted in not including a fit in the aforementioned figures.

When looking at the increase in average G_{1c} values between steps as shown in table 6.2 the following observation can be made: If we do not consider the initial step from room temperature up to $T_g - 45$ °C, values increase by a smaller percentage with each consecutive step in T_{env}. This seems to indicate that the step from $T_g - 45$ °C to $T_g - 35$ °C results in the relative largest effect on the degree of healing in the weld bond.

Additionally an increase in G_{1c} is already measured at T_{env} values for which, according to the simulations made with Digimat AM, the time spend above T_g has not yet increased.

7.3.2 Relating IR image data to mechanical testing results

As stated in section 7.3.1, mechanical properties already seem to increase at T_{env} values for which simulations do not yet show a significant increase in time spend above T_g. This can be understood by acknowledging that the simulations underestimate the actual temperature in the part during printing as stated in section 7.1.2. Considering the fact that actual temperature of the part seems to be roughly 20 °C above the temperature data suggested by simulations, the first step up in T_{env} is expected to more closely resemble the increase seen for simulations at $T_g - 35$ °C and $T_g - 25$ °C. Indeed this step indicates the first point at which the central part of the specimen spends a continuous amount of time above T_g as can be seen in figure 6.4. Each subsequent step then results in a significant increase in time spend above T_g. As such this can explain how an increase in mechanical properties is already observed at T_{env} values for which this would not yet be expected when solely considering the simulated data.

7.3.3 Increased interlayer properties due to part residing above T_g

Comparing the increase in G_{1c} with the time-temperature graphs obtained with Digimat AM, as shown in figure 6.4, it can be explained why the first step in T_{env} exhibits different behavior. When we consider what was stated in section 7.1.2, the first step up in T_{env} (to $T_g - 45$ °C) is expected to provide a temperature history as presented by simulations at $T_g - 25$ °C. This is the first simulated curve at which the printed part resides a significant time above T_g. Thus weld bond healing is expected to occur. From this step onwards the time spend above T_g increases exponentially. This is expected to cause a significant increase in the weld time and, as a result, a significant increase in mechanical properties.

If the results presented in figure 6.8 and table 6.2 are considered properties are shown to indeed increase with each subsequent step up in T_{env}. This increase in properties however is not exponential. It is observed that G_{1c} values appear to increase less with each subsequent step even though the weld time is still expected to increase quite drastically. This could be explained due to mechanical properties approaching bulk value. Properties in a weld bond approaching bulk properties have been shown to increase by a root function when plotted against the weld time. The theory behind this was described in section 3.1.3.

An effort has been made to confirm this expected cause of the decrease in the rate at which mechanical properties increase with raising T_{env} from $T_g - 35$ °C onwards. To achieve this, G_{1c} data was plotted against the time spend above T_g instead of T_{env}. Using the time-temperature

curves obtained with simulations, as shown in figure 6.4, the time a part remains at $T > T_g$ at specific T_{env} values can be determined. These values have been normalized by dividing by the maximum temperature reported by the simulations (around 70 seconds). This has been plotted against the G_{1c} values measured for the respective T_{env} values in figure 7.1.

Again the limited amount of data points and relatively large standard deviation prevents us from fitting a line. However, plotted data appears to follow a curve resembling a root function. This is as expected considering equation 3.8, and more generally 3.9. Theory by Wool [97] suggested exponents with either a value of $n = 1/4$ or $n = 1/2$, depending on how the mechanical property is related to the interpenetration depth of the molecular chain. For the derivations the reader is referred to section 3.1.3. In order to give an interpretation of the degree to which these trends are followed, curves have been added to the figure varying the values for the exponential in equation 3.8. Variations of n-values ranging from $n = 1/2$ to $n = 1/6$ have been introduced in equation 7.1, assuming the average G_{1c} value measured for $T_g - 15$ °C as a maximum G_{1c} value. It should be noted that this value was chosen as no bulk values are available. This is not considered to be the bulk value of this material, but rather the maximum value achieved thus far.

$$G_{1c}(t) = G_{1c\infty}\left(\frac{t}{t_{rep}}\right)^n. \tag{7.1}$$

Figure 7.1 shows that the exponential of a fit with similar shape to equation 3.9 would be significantly different to the value equation 3.8. This exponential would be closer to $n = 1/6$ than the $n = 1/2$ value which Wool prescribes.

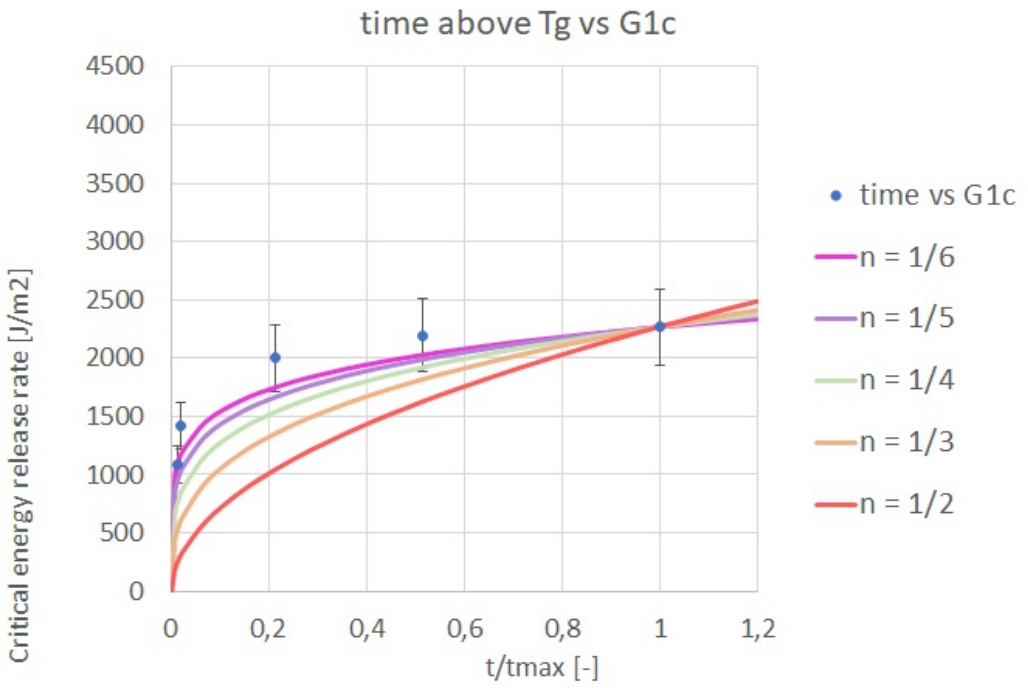

Figure 7.1: Results from DCB tests on PETG printed specimens after applying modified beam theory plotted against the time respective specimens spend above T_g.

Leaving the exact value of the exponent aside for now, a maximum value is expected to occur at the situation presented in equation 7.2

$$\left(\frac{t}{t_{rep}}\right)^{n} = 1. \tag{7.2}$$

That is to say: G_{1c} values should approach a horizontal asymptote for samples which spend more time above T_g. The data presented in figure 7.1 appears to follow a similar trend.

As stated in section 7.1.2 and 7.3.2, when using the simulated data it is necessary to keep in mind that this significantly underestimates the temperature actually reached in printed parts. As a result nodes are expected to remain above T_g for longer times than indicated in figure 7.1. This would stretch the data horizontally with respect to the y-axis. Repeating this with simulated values which more closely resemble reality is expected to present data which more closely agrees with the theory presented in section 3.1.3.

Additionally the discrepancy in the exact value of the exponent could be explained in part by the weld bond not being isothermal for the time it remains above T_g, i.e. the welding time. Temperature in FFF produced parts follows a specific shape of time-temperature curve. This has been established by previous work, presented in figure 3.11, as well as with simulations as shown in figure 6.4 and data obtained by IR imaging presented in figure 6.5. These consistently show that after an initial sharp drop, the temperature consistently lowers until T_{part} approaches a minimum close to T_{env}.

From figure 6.4 it has been determined that time spend above T_g increases for increasing T_{env} values. Additionally figure 3.10 shows that reptation time decreases exponentially with ΔT increasing with respect to T_g increasing. Figure 6.4 also shows that this ΔT increases for elevated T_{env} values. From this it can readily be understood that $\frac{t}{t_{rep}}$ (from here on indicated with τ) increases with increasing T_{env} values.

In isothermal situations, theory as presented by Wool *et al.* suggests that τ can be directly related to the degree of healing in the weld bond. However, due to the non isotherm nature of the FFF process it is not readily apparent how a representative value of τ can be obtained. In order to obtain a curve approaching the behavior described by Wool [97] it is desired to obtain a representative τ value. This value needs to be approached as the sum of all time steps (dt) in the time-temperature curve divided by the respective reptation time ($t_{rep}(t)$) as determined using a WLF plot. A suggestion for this approach, based on the work of Seppala [84], is shown in equation 7.3

$$\int_0^{t_{T=T_g}} \left(\frac{1}{t_{rep}(t)}\right) dt = \left(\frac{t}{t_{rep}}\right)_{representative} = \tau_{representative}. \tag{7.3}$$

In order to clarify this approach and provide a visual explanation of how equation 7.3 has been derived, figure 7.2 is included.

For inifinitesimally small time steps these values plotted against G_{1c} values are expected to provide curves showing behavior similar to isothermal welding conditions as presented by Wool *et al.* [97]. Due to the absence of rheology measurements for the specific material used in this research, and a lack in precision of the time-temperature history of the printed specimens, such calculations are omitted from this report.

Recent work by Seppala *et al.* [84] and Coogan *et al.* [25] has shown promising results regarding the predictive capabilities of such a representative τ value. In this previous work the representative weld time is named the equivalent isothermal weld time, which can be understood considering that this calculated value can be substituted into equation 3.9 which normally assumes a constant t_{rep} in isothermal situations.

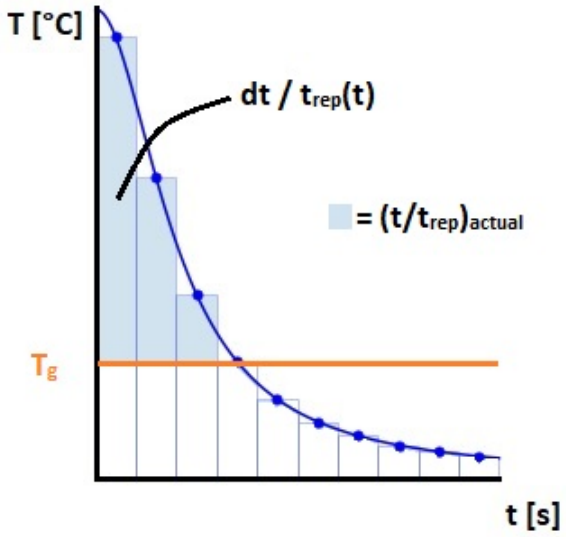

Figure 7.2: Graph explaining how summation of $\frac{dt}{t_{rep}(t)}$ can be used to determine a representative value of $\frac{t}{t_{rep}}$.

Another explanation for the curve in figure 7.1 having a different slope could be that a maximum value for increasing properties by raising T_{env} has already been (approximately) attained at a T_{env} before the highest T_{env} value measured. Taking into consideration that the standard deviation measured for G_{1c} values at $T_g - 25$ °C and $T_g - 15$ °C easily covers the measured increase in average G_{1c} value this is a distinct possibility. As a result only considering the initial values may provide a curve which better represents the behavior as described by Wool [97] in equation 3.8. Indeed excluding the maximum T_{env} ($T_g - 15$ °C) samples from figure 7.1 shows a curve which starts to more closely resemble equation 3.8. This would however indicate that the temperature histories simulated and measured for tensile specimens are not representative for the DCB samples. Due to relative values of the standard deviations, the absence of G_{1c} values for the bulk material and limited availability of data points at this time no definitive statements can be made regarding this phenomenon.

Unfortunately no reptation time versus temperature curve was found in literature for PETG. Additionally results obtained with simulations run in this research leave room for improvement as specified in section 7.1.2. Thus, currently it is not possible to implement equation 7.3. Due to the printer not being capable of reaching T_{env} values over $T_g - 15$ °C not enough data points were collected to make definitive statements regarding the degree of healing obtained thus far.

7.3.4 Increased UTS for printing at higher T_{env}

An initial look at figure 6.13 shows that results obtained with the tensile test samples show less consistent results compared with DCB tests. However, overall these samples still show an increase in mechanical properties of up to 50 % for samples printed at higher T_{env} values. It immediately stands out that two sample sets, $T_g - 35$ °C and $T_g - 15$ °C, show lower UTS values compared to the previous T_{env} set. This inconsistency is not seen in data collected from DCB samples.

The fracture surfaces of tensile specimens as presented in figures 6.10 and 6.11 provide a

possible explanation for this inconsistency. Inspection of the fracture surfaces of the samples, along with their respective UTS values as shown in the figures indicates that samples of which fracture surface areas appear more solid tend to have better mechanical properties. This is elaborated upon further in section 7.4, which discusses the effect of meso-strucure on mechanical properties.

Due to difficulties in achieving the desired T_{env} values during the printing of tensile specimens, measured UTS values could not all be related to simulated data as has been done for G_{1c} values in figure 7.1. Simulated data for the intermediate temperatures achieved during printing of the tensile specimens was not available. As a result a graph relating tensile properties to the time spend above T_g, as presented for G_{1c}, could not be produced. Additionally, due to T_{env} values of printed samples varying little no additional insights are expected to be gained with such a graph. Therefore no additional simulations have been run.

7.3.5 Increased tensile toughness for printing at higher T_{env}

Tensile toughness (U_T) is a measure for the amount of energy a material can absorb under tensile deformation without fracturing. U_T is commonly denoted in $[J/m^3]$. The U_T can be measured by integrating the stress strain curve up until fracture. The U_T has been determined using the stress strain curves obtained with tensile testing specimens printed at different T_{env} values. Figure 6.14 shows the average and standard deviation of the U_T plotted against the respective T_{env} values.

An increase in average U_T of 106 % has been reported in section 6.5.4. Comparing this to the increase in interlayer fracture toughness measured in DCB samples of 109 % a similar increase is observed. Both quantities are measures for the energy required to induce failure through fracture by applying a load perpendicular to the interlayer bonding. A similar increase in interlayer bonding is therefore expected across two different testing methods. The results obtained from mechanical tests seem to support this.

It should be noted that standard deviations determined for the U_T are not insignificant and need to be taken into consideration. Values for the standard deviation of U_T are calculated to be between 23 % and 36 %. This is mainly due to this property being determined using two measured quantities which both already show standard deviations up to 22 %.

7.4 Impact of sample meso-structure on measured mechanical properties.

In this section the images showing the meso-structure of tested samples are discussed. This includes both the images obtained with optical microscopy and micro CT. Firstly, the fracture surfaces of tensile specimens are discussed. Subsequently, the results obtained with micro CT are discussed in relation to the expectations and the results obtained with mechanical tests.

7.4.1 Analyzing the meso-structure in tensile samples

Optical microscopy has been used to measure the void percentage in each tensile sample. Subsequently this has been used to calculate corrected UTS values, referred to in this report as "actual UTS". Figure 6.12, and the data presented in table 6.4, show that the void area percentage can differ drastically across tested tensile samples. When comparing the initial and

actual UTS values, as presented in table 6.5, it can be seen that relatively the standard deviations decrease slightly for the actual UTS values. Furthermore, the actual UTS values do no longer show a drop in UTS values at $T_g - 15$ °C. This is more in line with what was expected considering the DCB sample results. At $T_g - 35$ °C a drop in UTS is still seen, however it is less drastic and is now within the standard deviation of the previous two T_{env} values.

7.4.2 Importance of meso-structure for interlayer energy release rate

As described in section 3.2 the healing of a weld bond is expected not to be the only parameter to contribute to the mechanical properties of FFF produced parts. Considering the the G_{1c} values obtained with the DCB samples, it has been shown by Hart [49] to be important to also consider the meso-structure of printed samples. As was presented in sections 2.1.3 and 3.2.1 a common feature of the meso-structure of FFF produced parts is the presence of voids. When considering the meso scale, these voids are the main feature affecting the mechanical properties of an FFF produced part. As a result they are the aspect focused on when discussing the micro CT results.

Generally speaking an increase in voids is considered a negative effect, as a smaller effective surface area in the material is loaded and thus stresses in the specimens increase. An example of this has been discussed in section 7.4.1. Fracture toughness (which is measured using G_{1c}) however is an interesting property as certain types of voids can actually increase the fracture toughness of a material. As was elaborated upon in section 3.3.2, the work of Hart *et al.* [49] showed that the formation of spherical voids through void coalescence can drastically increase the fracture toughness. Hart reported that this coalescence of the voids within a 3D-printed specimens can occur while annealing it at temperatures above T_g. DCB samples were inspected using micro CT because this effect was considered relevant for the properties measured using this type of test specimen.

7.4.3 Analyzing the meso-structure of DCB samples

Considering figure 6.16, it can be seen that the voids in the tested samples mostly align perpendicular to the build plate. These voids can be attributed to the print road width of printed roads being inconsistent. These are often less than the value set in the slicer software. Due to these inconsistencies it becomes difficult to describe concise relations between the meso-structure and the T_{env} at which samples are printed. It is apparent that, at least with the current set up, the printing process used is not consistent enough to make definitive statements about these relations.

In table 6.6 it can be seen that the maximum and minimum area measured can differ by up to a factor 2. Comparing this to the average area percentage and the standard deviation measured over roughly 1000 cross sections within a sample size of approximately 10x10x13 mm^3 the added benefit of using micro CT becomes apparent. Analyzing the micro CT results and considering the results as presented in table 6.6 the an-isotropic and inhomogeneous nature of FFF produced samples is further established. As a result, it becomes apparent that when optical microscopy or SEM imaging is used to validate the consistency of sample meso-structure, and print quality, it is advisable to consider cross sections at multiple locations within the sample.

While no relation between T_{env} and the meso-structure as described by Hart [49] has been found, several other results have been obtained. The area percentage of air measured has been used in section 6.6 to determine the effective interlayer fracture toughness. Literature indicated that the effect of increased strength obtained for FFF produced samples at elevated room, bed

and nozzle temperatures can largely be attributed to a change (or decrease) in voids in the meso-structure [11][12][49][89]. Table 6.7 shows the G_{1c} values both as measured and corrected for the effective surface area in the samples. This effect leads to a maximum increase of 10 % in G_{1c} values for corrected values. Considering these results in the context of the 109 % increase measured for G_{1c} in this research, it becomes apparent that a significant effect other than the meso-structure contributes. Considering the reported temperatures of parts during printing in sections 6.2 and 6.3 this can largely be contributed to the increased degree of interlayer diffusion when parts remain above T_g during printing.

The standard deviation determined for the area percentage values within single samples, as presented in table 6.6, are quite significant at up to 20 % of the average value. Considering the results presented for tensile specimens in table 6.4, it is likely similar variations in void content can be found for DCB samples printed on the same machine. It can be seen in figure 6.8 and table 6.2 that standard deviations of G_{1c} values measured for the DCB samples are also quite significant. This variation in effective surface area can partly explain the variation in G_{1c}.

In order to make more definitive statements about this it would be preferable to obtain more data about the effective surface area of all specimens printed at a specific T_{env}. As was the case for tensile specimens, described in section 7.4.1, the corrected G_{1c} values might lead to a smaller standard deviation. This could provide more precise data regarding the increase in mechanical properties with respect to the increased T_{env} values.

Chapter 8

Conclusion

This research focused on the 3D-printing of fused filament fabricated (FFF) parts at elevated print room temperatures (T_{env}). This was expected to enhance mechanical properties due to increased inter-molecular diffusion in interlayer weld bonds residing due to these residing above the glass transition temperature (T_g) for prolonged periods of time. In order to validate this hypothesis, it was firstly necessary to determine if raising T_{env} prolonged the time the printed part resided above T_g. Secondly, a method of testing the interlayer properties in FFF samples needed to be determined . Thirdly relating the results of the previous two research questions a possible relation between these needed to be determined. Finally, it was necessary to evaluate if observed changes in mechanical properties were predominantly caused by the increased inter-molecular diffusion.

In order to verify if elevating T_{env} significantly prolonged the time a part resides above T_g simulations have been run, which have been verified using IR imaging. Simulating the temperature history of FFF parts during printing over a range of T_{env} values it was found that this significantly increases part temperature. It has been shown that even for T_{env} values significantly below T_g this can lead to the part residing above T_g for prolonged period of time. IR imaging during printing indicated that simulations underestimate the temperature during printing by up to 20 °C. This explained why effects on interlayer weld bond healing occured earlier than simulations suggested. Simulations as used in this report leave room for improvement.

A method has been determined which is capable of evaluating interlayer properties in FFF produced samples. This method is based on double cantilevered beam (DCB) testing. Sample dimensions have been based in previous work done by Aliheidari *et al.* [11][12] and altered according to ASTM D5528 [15]. This method has been used to measure interlayer mechanical properties in FFF parts. Additionally tensile tests have been performed in order to determine the effect of interlayer bonding on other mechanical properties.

Results obtained with the mechanical testing of DCB and tensile samples printed at elevated T_{env} values showed a significant increase in mechanical properties. Critical energy release rate (G_{1c}) showed an increase of up to 108 %, ultimate tensile strength (UTS) showed an increase of up to 50 % and tensile toughness (U_T) showed an increase of up to 106 %. The Critical energy release rate, which is a measure for the interlayer fracture toughness has been shown to increase a same order of magnitude as the U_T. Both are a measure for the amount of energy a sample can take before failure. This provided additional confidence in the consistency of the results obtained with mechanical testing.

Previous research indicated that varying temperature related parameters can lead to an increase in mechanical properties due to changes in sample meso-structure. Micro CT and optical microscopy have been used in order to inspect the meso-structure of tested samples. From this it has been determined that the meso-structure did not contribute significantly to the increase in mechanical properties. Correcting for effective surface areas showed an increase of average mechanical properties of around 10 %. No significant differences have been found comparing these results between sample sets printed at different T_{env} values. No significant qualitative difference has been observed in the shape of voids in printed DCB and tensile samples printed at different T_{env} values. It has therefore been concluded that inter-molecular diffusion is expected to be the dominant mechanism causing the reported increase in interlayer properties.

A lack of interlayer bonding in the direction perpendicular to the print bed generally results in mechanical properties of FFF printed parts being significantly weaker in this direction. Mechanical properties have been shown to decrease to 30 % of bulk mechanical properties when loaded in this direction. The work presented in this research verified that, for an amorphous thermoplastic polymer, raising T_{env} to temperatures close to T_g, results in printed parts with significantly increased mechanical interlayer properties. By increasing the T_{env} to values close to the T_g of the material being printed, part temperatures have been shown to remain above T_g for prolonged periods of time. The resulting inter-molecular diffusion resulted in interlayer mechanical properties increasing around 50 % to 100 % compared to samples printed at room temperature.

As a result this research provides a method of reducing the an-isotropy of printed parts by increasing interlayer mechanical properties. These increased mechanical properties serve to make 3D printed parts more viable in situations in which significant loads are present. The decreased an-isotropy is expected to enhance the predictability of the material's response under load. A method has been suggested which is expected to aid in the modelling of the behavior of FFF produced parts. By being able to predict the mechanical response of 3D-printed parts, printing critical parts becomes a viable option. Eventually this is expected to help FFF printing towards a future where it can be used as a method for the production of structurally critical parts.

Chapter 9

Recommendations

As stated in chapter 8 this research is expected to provide a stepping stone for bringing FFF to a future where it can be used for the production of structurally critical parts. This section serves to present recommendations for future research which are expected to serve this purpose.

In order to verify the degree of healing achieved with raising T_{env} values, it is recommended to determine bulk mechanical properties. These can serve as a benchmark to test against. This is not limited to the case of weld bond healing, but may also provide a relevant benchmark when considering other research into the mechanical properties of FFF produced parts. Consider, for example, how specific material properties compare between samples consisting of bulk material and 3D-printed samples with certain infills. Currently data sheets for FFF filament materials generally do not provide bulk data for mechanical properties. It is suggested that in order to obtain bulk values for filament material test samples are produced by either casting or extrusion molding the filament material. By extrusion molding shredded filament material a homogeneous sample can be obtained. Additionally annealing this sample at temperatures above T_g ensures a completely homogenized sample providing bulk material properties. It is important to ensure no voids are contained in the sample during this process, as was discussed in section 3.3.2.

The production and testing of samples at higher T_{env} values is suggested in order to obtain a larger data set. Additionally a printer should be used which more precisely controls T_{env} in order to obtain data for samples printed at intermediary T_{env} values. A larger data set can be used for more precise predictions about the degree of weld bond healing with respect to the relevant T_{env} value. A maximum T_{env} value may thus be obtained at which the structural integrity of parts during printing starts to be affected by the elevated print room temperatures. Combining this data with the bulk value of a material can show if the interlayer weld bond has fully healed at this T_{env} value. This can be used to determine an optimal T_{env} value.

In section 7.3.3 the results obtained with mechanical tests during this research are related to theory on the development of polymer weld bond healing with respect to the t_{weld} and t_{rep} [97]. A method for determining an equivalent isothermal weld time is suggested which might be used to more accurately predict the degree of weld bond healing. Previous work by Seppala And Coogan [25][84] showed promising results on the capabilities of equivalent isothermal weld times in predicting mechanical properties. For this research it would be required to perform rheology measurements on the filament material used to print the test samples.

It is recommended to link this research to precise simulations of the temperature history in printed parts and knowledge on bulk material properties of the filament material. By combining this it is expected to be possible to precisely predict the mechanical properties of samples at

specified T_{env} values. This provides interesting possibilities regarding the incorporation of such simulations in FEM analyses of complex load cases on FFF produced parts.

During this research only amorphous thermoplastic polymers have been discussed. Semi-crystalline materials however make up a significant part of the types of FFF filament materials available. A selection high-end materials with interesting mechanical properties, such as nylon and PEEK, are semi-crystalline. These materials are of significant interest to both industry and defense. Thus it is recommended to investigate the relevance of the research presented of this report in the context of semi-crystalline materials. Additionally it is recommended to verify the results presented in this research for other types of amorphous thermoplastic materials to ensure that it is indeed the increased inter-molecular diffusion which leads to the enhanced mechanical properties.

The method suggested in this report utilizes the print chamber temperature as a method of increasing the inter-layer weld bond to temperatures above T_g. While this uses existing equipment and provides significant results it is not very energy efficient. Considering the exponential behavior of the reptation time with increased temperatures, it is recommended to investigate the possibilities regarding localised heating of the part before depositing a new layer of filament. At sufficiently high local temperatures inter-molecular diffusion has been shown in figure 3.10 to lead to reptation times in the order of milliseconds. This could provide near instantaneous welding, making it redundant to keep T_{env} at temperatures higher than required for the prevention of warping. Additionally this may increase weld bond healing to a degree not possible without potential loss of structural integrity caused by elevating T_{env} above T_g.

Bibliography

[1] Differential scanning calorimetry thermo-gravimetric analysis. http://www.flemingptc.co.uk/our-services/dsc-tga/. Accessed: 22-01-2018.

[2] Dimafix. http://www.dima3d.com/en/home/dimafix/. Accessed: 14-01-2018.

[3] Material properties database. https://www.makeitfrom.com. Accessed: 18-02-2019.

[4] Stratasys. https://www.stratasys.com/. Accessed: 20-9-2018.

[5] Technical data sheet product name: Hdglass^{TM}. v3.

[6] testxpert ii testing software – intelligent and reliable. https://www.zwickroell.com/en/testing-software/testxpert-ii. Accessed: 05-03-2018.

[7] Using differential scanning calorimetry to characterize polymers. https://www.azom.com/article.aspx?ArticleID=15458. Accessed: 22-01-2018.

[8] What is 3d printing? https://www.3dhubs.com/what-is-3d-printing. Accessed: 19-9-2018.

[9] 3D4makers. High temperature fdm 3d printing for pei, peek and other high performance polymers what you need to know. https://www.3d4makers.com/blogs/news/. Accessed: 14-12-2018.

[10] Alger, M. (2017). *Polymer Science Dictionary*. Springer Netherlands.

[11] Aliheidari, N., Christ, J., Tripuraneni, R., Nadimpalli, S., and Ameli, A. (2018). Interlayer adhesion and fracture resistance of polymers printed through melt extrusion additive manufacturing process. *Materials & Design*, 156:351–361.

[12] Aliheidari, N., Tripuraneni, R., Ameli, A., and Nadimpalli, S. (2017). Fracture resistance measurement of fused deposition modeling 3d printed polymers. *Polymer Testing*, 60:94–101.

[13] Álvarez, K., Lagos, R. F., and Aizpun, M. (2016). Investigating the influence of infill percentage on the mechanical properties of fused deposition modelled ABS parts. *Ingeniería e Investigación*, 36(3):110.

[14] Anderson, K., Wescott, J., Carver, T., and Windle, A. (2004). Mesoscale modelling of polymer welding. *Materials Science and Engineering: A*, 365(1-2):14–24.

[15] ASTM D5528-01 (2002). Standard Test Method for Mode I Interlaminar Fracture Toughness of Unidirectional Fiber-Reinforced Polymer Matrix Composites. Standard, American Society for Testing Materials, West Conshohocken.

[16] Azimi, P., Zhao, D., Pouzet, C., Crain, N. E., and Stephens, B. (2016). Emissions of ultrafine particles and volatile organic compounds from commercially available desktop three-dimensional printers with multiple filaments. *Environmental Science & Technology*, 50(3):1260–1268.

[17] Bassoli, E., Gatto, A., Iuliano, L., and Violante, M. G. (2007). 3d printing technique applied to rapid casting. *Rapid Prototyping Journal*, 13(3):148–155.

[18] Belter, J. T. and Dollar, A. M. (2015). Strengthening of 3d printed fused deposition manufactured parts using the fill compositing technique. *PLOS ONE*, 10(4):e0122915.

[19] Ben Redwood, F. S. and Garret, B. (2017). *The 3D Printing Handbook*. 3D Hubs B.V.

[20] Berens J., Bex G.J.P., t. C. A. K. J. (2018). Markforged materials research tno 2018 r10875.

[21] Braun, E. and Levin, B. C. (1987). Nylons: A review of the literature on products of combustion and toxicity. *Fire and Materials*, 11(2):71–88.

[22] Cebon, M. A. H. S. D. (2012a). *Introduction to the physics and chemistry of materials*. Taylor Francis Group.

[23] Cebon, M. A. H. S. D. (2012b). *Materials: Engineering, Science, Processing and Design*. Elsevier.

[24] Chen, J., Yang, W., ping Yu, G., Wang, M., ying Ni, H., and zhi Shen, K. (2008). Continuous extrusion and tensile strength of self-reinforced HDPE/UHMWPE sheet. *Journal of Materials Processing Technology*, 202(1-3):165–169.

[25] Coogan, T. J. and Kazmer, D. O. (2017). Healing simulation for bond strength prediction of FDM. *Rapid Prototyping Journal*, 23(3):551–561.

[26] David Espalin, Mireya Perez, F. M. and Wicker, R. Sterilization of fdm-manufactured parts.

[27] de Gennes, P.-G. (1983). Entangled polymers. *Physics Today*, 36(6):33–39.

[28] Dizon, J. R. C., Espera, A. H., Chen, Q., and Advincula, R. C. (2018). Mechanical characterization of 3d-printed polymers. *Additive Manufacturing*, 20:44–67.

[29] Doolittle, A. K. (1951). Studies in newtonian flow. i. the dependence of the viscosity of liquids on temperature. *Journal of Applied Physics*, 22(8):1031–1035.

[30] dr. Joost van Lingen. Munitie uit de printer. https://time.tno.nl/nl/artikelen/munitie-uit-de-printer/. Accessed: 19-9-2018.

[31] DSC3+. Differential Scanning Calorimetry - for Unmatched Performance. Brochure, Mettler Toledo, Switzerland.

[32] Edwards, S. F. and Vilgis, T. A. (1988). The tube model theory of rubber elasticity. *Reports on Progress in Physics*, 51(2):243–297.

[33] Einstein, A. (2005). Über die von der molekularkinetischen theorie der wärme geforderte bewegung von in ruhenden flüssigkeiten suspendierten teilchen [AdP 17, 549 (1905)]. *Annalen der Physik*, 14(S1):182–193.

[34] Fernandez-Vicente, M., Calle, W., Ferrandiz, S., and Conejero, A. (2016). Effect of infill parameters on tensile mechanical behavior in desktop 3d printing. *3D Printing and Additive Manufacturing*, 3(3):183–192.

[35] Fixman, M. (1955). Excluded volume in polymer chains. *The Journal of Chemical Physics*, 23(9):1656–1659.

[36] Fleischer, G. (1984). Temperature dependence of self diffusion of polystyrene and polyethylene in the melt an interpretation in terms of the free volume theory. *Polymer Bulletin*, 11(1):75–80.

[37] Fodran, E., Koch, M., and Menon, U. (1996). Mechanical and dimensional characteristics of fused deposition modeling build styles. In *Solid Freeform Fabrication Proc*, pages 419–442.

[38] Formfutura. Technical data sheet product name: Premium abs. Technical report. v3.

[39] Forster, A. M. (2015). Materials testing standards for additive manufacturing of polymer materials: State of the art and standards applicability. Technical report.

[40] Fujita, H. Diffusion in polymer-diluent systems. In *Fortschritte Der Hochpolymeren-Forschung*, pages 1–47. Springer-Verlag.

[41] Garcia, C. R., Correa, J., Espalin, D., Barton, J. H., Rumpf, R. C., Wicker, R., and Gonzalez, V. (2012). 3d PRINTING OF ANISOTROPIC METAMATERIALS. *Progress In Electromagnetics Research Letters*, 34:75–82.

[42] Ge, T., Robbins, M. O., Perahia, D., and Grest, G. S. (2014). Healing of polymer interfaces: Interfacial dynamics, entanglements, and strength. *Physical Review E*, 90(1).

[43] Gill, S. S. and Kaplas, M. (2009). Comparative study of 3d printing technologies for rapid casting of aluminium alloy. *Materials and Manufacturing Processes*, 24(12):1405–1411.

[44] Gotro, J. Poly lactic acid (pla) is gaining traction in the market. https://polymerinnovationblog.com/poly-lactic-acid-pla-is-gaining-traction-in-the-market/. Accessed: 22-10-2018.

[45] Gottstein, G. (2004). *Physical Foundations of Materials Science*. Springer Berlin Heidelberg.

[46] Greco, A., Rizzo, M., and Maffezzoli, A. (2012). Effect of the addition of organically modified nanofiller on the relaxation behavior of a thermoplastic amorphous matrix. *Thermochimica Acta*, 543:226–231.

[47] Guo, Y., Wang, Q., and Bai, S. (2010). The effect of rotational extrusion on the structure and properties of HDPE pipes. *Polymer-Plastics Technology and Engineering*, 49(9):908–915.

[48] Haire, K. and Windle, A. (2001). Monte carlo simulation of polymer welding. *Computational and Theoretical Polymer Science*, 11(3):227–240.

[49] Hart, K. R., Dunn, R. M., Sietins, J. M., Mock, C. M. H., Mackay, M. E., and Wetzel, E. D. (2018). Increased fracture toughness of additively manufactured amorphous thermoplastics via thermal annealing. *Polymer*, 144:192–204.

[50] Henshaw, J. M., Han, W., and Owens, A. D. (1996). An overview of recycling issues for composite materials. *Journal of Thermoplastic Composite Materials*, 9(1):4–20.

[51] ISO 11357 (2013). Plastics – Differential scanning calorimetry (DSC) – Part 2: Determination of glass transition temperature and glass transition step height. Standard, International Organization for Standardization, Geneva.

[52] ISO 527-1 (2012). Plastics – Determination of tensile properties – Part 1: General principles (ISO527-1:2012,IDT). Standard, International Organization for Standardization, Geneva.

[53] ISO 527-2 (2012). Plastics – Determination of tensile properties – Part 2: Test conditions for moulding and extrusion plastics (ISO527-2:2012,IDT). Standard, International Organization for Standardization, Geneva.

[54] Jansen, J. A. (2016). Plastics – it's all about molecular structure. 72(8).

[55] Janssen, M., Zuidema, J., and Wanhill, R. (2006). *Fracture mechanics*. VSSD.

[56] Jia, N., Fraenkel, H. A., and Kagan, V. A. (2004). Effects of moisture conditioning methods on mechanical properties of injection molded nylon 6. *Journal of Reinforced Plastics and Composites*, 23(7):729–737.

[57] Jud, K., Kausch, H. H., and Williams, J. G. (1981). Fracture mechanics studies of crack healing and welding of polymers. *Journal of Materials Science*, 16(1):204–210.

[58] Karatzas, I. and Shreve, S. E. (1988). Brownian motion. In *Brownian Motion and Stochastic Calculus*, pages 47–127. Springer US.

[59] Kemmish, D. (2011). *High Performance Engineering Plastics*. Smithers Rapra Technology.

[60] Kim, E., Shin, Y.-J., and Ahn, S.-H. (2016). The effects of moisture and temperature on the mechanical properties of additive manufacturing components: fused deposition modeling. *Rapid Prototyping Journal*, 22(6):887–894.

[61] Koch, C., Hulle, L. V., and Rudolph, N. (2017). Investigation of mechanical anisotropy of the fused filament fabrication process via customized tool path generation. *Additive Manufacturing*, 16:138–145.

[62] Lederle, F., Meyer, F., Brunotte, G.-P., Kaldun, C., and Hübner, E. G. (2016). Improved mechanical properties of 3d-printed parts by fused deposition modeling processed under the exclusion of oxygen. *Progress in Additive Manufacturing*, 1(1-2):3–7.

[63] Lee, B., Abdullah, J., and Khan, Z. (2005). Optimization of rapid prototyping parameters for production of flexible ABS object. *Journal of Materials Processing Technology*, 169(1):54–61.

[64] Luzanin, O., Movrin, D., and Plancak, M. (2014). Effect of layer thickness, deposition angle, and infill on maximum flexural force in fdm-built specimens. *Journal for Technology of Plasticity*, 39.

[65] Mackay, M. E., Swain, Z. R., Banbury, C. R., Phan, D. D., and Edwards, D. A. (2017). The performance of the hot end in a plasticating 3d printer. *Journal of Rheology*, 61(2):229–236.

[66] Madhukar Somireddy, A. C. (2017). Mechanical characterization of additively manufactured parts by FE modeling of mesostructure. *Journal of Manufacturing and Materials Processing*, 1(2):18.

[67] Mark, J. E., editor (2007). *Physical Properties of Polymers Handbook*. Springer New York.

[68] Martínez, A., León, N., Arencón, D., Rodríguez, J., and Salazar, A. (2013). On the effect of the different notching techniques on the fracture toughness of PETG. *Polymer Testing*, 32(7):1244–1252.

[69] Matterhackers. 3d printer filament comparison guide. https://www.matterhackers.com/3d-printer-filament-compare. Accessed: 22-10-2018.

[70] Matterhackers. Beat moisture before it kills your 3d printing filament. https://www.matterhackers.com/news/filament-and-water. Accessed: 20-11-2018.

[71] McIlroy, C. and Olmsted, P. (2017a). Disentanglement effects on welding behaviour of polymer melts during the fused-filament-fabrication method for additive manufacturing. *Polymer*, 123:376–391.

[72] McIlroy, C. and Olmsted, P. D. (2017b). Deformation of an amorphous polymer during the fused-filament-fabrication method for additive manufacturing. *Journal of Rheology*, 61(2):379–397.

[73] Milde, J., Morovič, L., and Blaha, J. (2017). Influence of the layer thickness in the fused deposition modeling process on the dimensional and shape accuracy of the upper teeth model. *MATEC Web of Conferences*, 137:02006.

[74] Neff, C., Trapuzzano, M., and Crane, N. B. (2018). Impact of vapor polishing on surface quality and mechanical properties of extruded ABS. *Rapid Prototyping Journal*, 24(2):501–508.

[75] Nielsen, M., Jurasek, P., Hayashi, J., and Furimsky, E. (1995). Formation of toxic gases during pyrolysis of polyacrylonitrile and nylons. *Journal of Analytical and Applied Pyrolysis*, 35(1):43–51.

[76] Park, J.-Y., Ha, S., Park, E., Kwon, D., and Kim, N. (2016). Hygroscopic swelling behavior of 3d printed parts due to changes in environmental conditions. In *Volume 1A: 36th Computers and Information in Engineering Conference*. ASME.

[77] Pham, M.-S., Liu, C., Todd, I., and Lertthanasarn, J. (2019). Damage-tolerant architected materials inspired by crystal microstructure. *Nature*, 565(7739):305–311.

[78] Rand, G. and Petrocelli, S. Fundamentals of aquatic toxicology: Methods and applications.

[79] Raz, K. and Zahalka, M. (2017). Tensile strength of various nylon PA6 specimen modes. Author(s).

[80] Righetti, M. (2017). Crystallization of polymers investigated by temperature-modulated DSC. *Materials*, 10(4):442.

[81] Rodríguez, J. F., Thomas, J. P., and Renaud, J. E. (2003). Mechanical behavior of acrylonitrile butadiene styrene fused deposition materials modeling. *Rapid Prototyping Journal*, 9(4):219–230.

[82] Rösler, J., Harders, H., and Baeker, M. (2007). *Mechanical behaviour of engineering materials: metals, ceramics, polymers, and composites*. Springer Science & Business Media.

[83] Rubinstein, M. and Colby, R. H. (2003). *Polymer physics*. Oxford university press New York.

[84] Seppala, J. E., Han, S. H., Hillgartner, K. E., Davis, C. S., and Migler, K. B. (2017). Weld formation during material extrusion additive manufacturing. *Soft Matter*, 13(38):6761–6769.

[85] Seppala, J. E. and Migler, K. D. (2016). Infrared thermography of welding zones produced by polymer extrusion additive manufacturing. *Additive Manufacturing*, 12:71–76.

[86] Somireddy, M., Czekanski, A., and Singh, C. V. (2018). Development of constitutive material model of 3d printed structure via FDM. *Materials Today Communications*, 15:143–152.

[87] Sood, A. K., Ohdar, R., and Mahapatra, S. (2010). Parametric appraisal of mechanical property of fused deposition modelling processed parts. *Materials & Design*, 31(1):287–295.

[88] Stephens, B., Azimi, P., Orch, Z. E., and Ramos, T. (2013). Ultrafine particle emissions from desktop 3d printers. *Atmospheric Environment*, 79:334–339.

[89] Sun, Q., Rizvi, G., Bellehumeur, C., and Gu, P. (2008). Effect of processing conditions on the bonding quality of FDM polymer filaments. *Rapid Prototyping Journal*, 14(2):72–80.

[90] Tanikella, N. G., Wittbrodt, B., and Pearce, J. M. (2017). Tensile strength of commercial polymer materials for fused filament fabrication 3d printing. *Additive Manufacturing*, 15:40–47.

[91] Thomas, L. C. Emissivity table. https://www.thermoworks.com/emissivity_table. Accessed: 8-4-2018.

[92] Thomas, L. C. Interpreting unexpected events and transitions in DSC results. http://www.tainstruments.com/pdf/literature/TA039.pdf. Accessed: 23-01-2018.

[93] Torres, J., Cotelo, J., Karl, J., and Gordon, A. P. (2015). Mechanical property optimization of FDM PLA in shear with multiple objectives. *JOM*, 67(5):1183–1193.

[94] van Veen, D. (2018). Determining and analyzing tensile properties of 3d-printed and conventionally produced (fiber reinforced) nylon samples.

[95] von Übel, M. 3d printing materials guide. https://all3dp.com/1/3d-printing-materials-guide-3d-printer-material/. Accessed: 19-9-2018.

[96] Williams, M. L., Landel, R. F., and Ferry, J. D. (1955). The temperature dependence of relaxation mechanisms in amorphous polymers and other glass-forming liquids. *Journal of the American Chemical Society*, 77(14):3701–3707.

[97] Wool, R., Yuan, B.-L., and McGarel, O. (1989). Welding of polymer interfaces. *Polymer Engineering & Science*, 29(19):1340–1367.

[98] Wouterson, E. M., Boey, F. Y., Hu, X., and Wong, S.-C. (2005). Specific properties and fracture toughness of syntactic foam: Effect of foam microstructures. *Composites Science and Technology*, 65(11-12):1840–1850.

[99] Wu, H., Imad, A., Benseddiq, N., de Castro, J. T. P., and Meggiolaro, M. A. (2010). On the prediction of the residual fatigue life of cracked structures repaired by the stop-hole method. *International Journal of Fatigue*, 32(4):670–677.

[100] Young, R. J. (1981). *Introduction to Polymers*. Springer US.

[101] Ziemian, C., Sharma, M., and Ziemi, S. (2012). Anisotropic mechanical properties of ABS parts fabricated by fused deposition modelling. In *Mechanical Engineering*. InTech.

Appendix A

Print settings used for DCB and Tensile specimens

In this appendix the print settings of DCB samples and Tensile samples are presented in the form of the G-code used for printing the samples. The G-code was generated using the Simplify3D slicer software. Except for the temperature settings as described in section 5.3.6 and 5.3.7 no print settings have been changed for the different sample sets.

DCB sample print settings

; G-Code generated by Simplify3D(R) Version 4.0.1
; Feb 19, 2019 at 9:03:51 AM
; Settings Summary
; processName,DDDROP_PETG_DCB
; applyToModels,DCB_v06
; profileName,DDDROP_PETG_Tensile (modified)
; profileVersion,2019-01-18 13:12:46
; baseProfile,Default
; printMaterial,
; printQuality,
; printExtruders,
; extruderName,Extruder 1,right extruder
; extruderToolheadNumber,0,1
; extruderDiameter,0.4,0.4
; extruderAutoWidth,1,1
; extruderWidth,0.48,0.48
; extrusionMultiplier,1.05,1.5
; extruderUseRetract,1,1
; extruderRetractionDistance,10,10
; extruderExtraRestartDistance,0.2,0.2
; extruderRetractionZLift,0.5,0.5
; extruderRetractionSpeed,2400,2400
; extruderUseCoasting,1,1
; extruderCoastingDistance,0.5,0.5

; extruderUseWipe,0,0
; extruderWipeDistance,5,5
; primaryExtruder,1
; layerHeight,0.1
; topSolidLayers,0
; bottomSolidLayers,9999
; perimeterOutlines,0
; printPerimetersInsideOut,0
; startPointOption,3
; startPointOriginX,0
; startPointOriginY,0
; sequentialIslands,0
; spiralVaseMode,0
; firstLayerHeightPercentage,250
; firstLayerWidthPercentage,110
; firstLayerUnderspeed,0.6
; useRaft,0
; raftExtruder,0
; raftTopLayers,3
; raftBaseLayers,2
; raftOffset,3
; raftSeparationDistance,0.14
; raftTopInfill,100
; aboveRaftSpeedMultiplier,0.3
; useSkirt,1
; skirtExtruder,1
; skirtLayers,4
; skirtOutlines,0
; skirtOffset,0
; usePrimePillar,0
; primePillarExtruder,999
; primePillarWidth,12
; primePillarLocation,7
; primePillarSpeedMultiplier,1
; useOozeShield,0
; oozeShieldExtruder,999
; oozeShieldOffset,2
; oozeShieldOutlines,1
; oozeShieldSidewallShape,1
; oozeShieldSidewallAngle,30
; oozeShieldSpeedMultiplier,1
; infillExtruder,1
; internalInfillPattern,Rectilinear
; externalInfillPattern,Rectilinear
; infillPercentage,100
; outlineOverlapPercentage,50
; infillExtrusionWidthPercentage,150

; minInfillLength,0
; infillLayerInterval,1
; internalInfillAngles,45,-45
; overlapInternalInfillAngles,0
; externalInfillAngles,90
; generateSupport,1
; supportExtruder,1
; supportInfillPercentage,40
; supportExtraInflation,0
; supportBaseLayers,0
; denseSupportExtruder,1
; denseSupportLayers,0
; denseSupportInfillPercentage,90
; supportLayerInterval,1
; supportHorizontalPartOffset,0.5
; supportUpperSeparationLayers,1
; supportLowerSeparationLayers,1
; supportType,0
; supportGridSpacing,1
; maxOverhangAngle,80
; supportAngles,90
; temperatureName,Heated Bed,right extruder
; temperatureNumber,1,1
; temperatureSetpointCount,1,1
; temperatureSetpointLayers,1,1
; temperatureSetpointTemperatures,80,225
; temperatureStabilizeAtStartup,0,1
; temperatureHeatedBed,1,0
; temperatureRelayBetweenLayers,0,0
; temperatureRelayBetweenLoops,0,0
; fanLayers,1,2
; fanSpeeds,0,80
; blipFanToFullPower,0
; adjustSpeedForCooling,1
; minSpeedLayerTime,20
; minCoolingSpeedSlowdown,50
; increaseFanForCooling,0
; minFanLayerTime,45
; maxCoolingFanSpeed,100
; increaseFanForBridging,0
; bridgingFanSpeed,100
; use5D,1
; relativeEdistances,0
; allowEaxisZeroing,1
; independentExtruderAxes,0
; includeM10123,0
; stickySupport,1

; applyToolheadOffsets,0
; gcodeXoffset,0
; gcodeYoffset,0
; gcodeZoffset,-0.05
; overrideMachineDefinition,1
; machineTypeOverride,0
; strokeXoverride,330
; strokeYoverride,310
; strokeZoverride,305
; originOffsetXoverride,0
; originOffsetYoverride,0
; originOffsetZoverride,0
; homeXdirOverride,-1
; homeYdirOverride,1
; homeZdirOverride,-1
; flipXoverride,1
; flipYoverride,-1
; flipZoverride,1
; toolheadOffsets,0,0—0,0—0,0—0,0—0,0—0,0
; overrideFirmwareConfiguration,0
; firmwareTypeOverride,RepRap (Marlin/Repetier/Sprinter)
; GPXconfigOverride,r2
; baudRateOverride,115200
; overridePrinterModels,0
; printerModelsOverride
; startingGcode,G21,G90,T1,M702 H39,M705 P15 I0.0001 ,M706 B4 I120 T29 H180 K255 J255,M703,M104 S0,T0,M104 S0,M140 S0,T1,G28,G1 Z5 F200,M140 S[bed0_temperature],T1,M104 S150,M190 S[bed0_temperature],M109 S[extruder1_temperature],G28,G1 Z1 F1000,G1 X75 Y-25 F8000,G1 X18,T1,G92 E0,G1 E20 F100,G92 E0,M760 t5,G1 X10 F10000,G1 Y-2 F10000,G1 X14 F10000,G1 Y-12 F10000,G1 X18 F10000,G1 Y-2 F10000,G1 X22 F10000,G1 Y-12 F10000,G1 X26 F10000,G1 Y-2 F10000
; layerChangeGcode,
; retractionGcode,
; toolChangeGcode,
; endingGcode,T0,M104 S0,T1,M104 S0,M140 S0,G92 Z10,G1 Z15,G1 Y30 F8000,G1 X75,G1 Y-25 F8000,G1 X18,M714,M760 t10,G1 X10 F10000,G1 Y-2 F10000,G1 X14 F10000,G1 Y-12 F10000,G1 X18 F10000,G1 Y-2 F10000,G1 X22 F10000,G1 Y-12 F10000,G1 X26 F10000,G1 Y-2 F10000,G28 Y0,G28 X0,M704,M702 H60,M705 P1 I0.01,M706 B0 I120 H120 T50 K255 J125,M84,M717
; exportFileFormat,gcode
; celebration,0
; celebrationSong,Random Song
; postProcessing,
; defaultSpeed,3000
; outlineUnderspeed,0.5
; solidInfillUnderspeed,1
; supportUnderspeed,1

; rapidXYspeed,9000
; rapidZspeed,1000
; minBridgingArea,50
; bridgingExtraInflation,0
; bridgingExtrusionMultiplier,1.1
; bridgingSpeedMultiplier,1
; useFixedBridgingAngle,0
; fixedBridgingAngle,0
; applyBridgingToPerimeters,0
; filamentDiameters,1.75—1.75—1.75—1.75—1.75—1.75
; filamentPricesPerKg,29.95—29.95—29.95—29.95—29.95—29.95
; filamentDensities,1.25—1.25—1.25—1.25—1.25—1.25
; useMinPrintHeight,0
; minPrintHeight,0
; useMaxPrintHeight,0
; maxPrintHeight,0
; useDiaphragm,0
; diaphragmLayerInterval,20
; robustSlicing,1
; mergeAllIntoSolid,0
; onlyRetractWhenCrossingOutline,1
; retractBetweenLayers,1
; useRetractionMinTravel,0
; retractionMinTravel,1
; retractWhileWiping,0
; onlyWipeOutlines,0
; avoidCrossingOutline,0
; maxMovementDetourFactor,3
; toolChangeRetractionDistance,0
; toolChangeExtraRestartDistance,0
; toolChangeRetractionSpeed,600
; externalThinWallType,0
; internalThinWallType,2
; thinWallAllowedOverlapPercentage,30
; singleExtrusionMinLength,1
; singleExtrusionMinPrintingWidthPercentage,50
; singleExtrusionMaxPrintingWidthPercentage,200
; singleExtrusionEndpointExtension,0.2
; horizontalSizeCompensation,0

Tensile sample print settings

; G-Code generated by Simplify3D(R) Version 4.0.1
; Feb 4, 2019 at 2:59:49 PM
; Settings Summary
; processName,DDDROP_PETG_Tensile

; applyToModels,ISO_527-2_2x_Zdirection_v10_smallfoot
; profileName,DDDROP_PETG_Tensile
; profileVersion,2019-01-18 13:12:46
; baseProfile,Default
; printMaterial,
; printQuality,
; printExtruders,
; extruderName,Extruder 1,right extruder
; extruderToolheadNumber,0,1
; extruderDiameter,0.4,0.4
; extruderAutoWidth,1,1
; extruderWidth,0.48,0.48
; extrusionMultiplier,1.05,1.1
; extruderUseRetract,1,1
; extruderRetractionDistance,10,10
; extruderExtraRestartDistance,0.2,0.2
; extruderRetractionZLift,0.5,0.5
; extruderRetractionSpeed,2400,2400
; extruderUseCoasting,1,1
; extruderCoastingDistance,0.5,0.5
; extruderUseWipe,0,0
; extruderWipeDistance,5,5
; primaryExtruder,1
; layerHeight,0.1
; topSolidLayers,0
; bottomSolidLayers,9999
; perimeterOutlines,0
; printPerimetersInsideOut,0
; startPointOption,3
; startPointOriginX,0
; startPointOriginY,0
; sequentialIslands,0
; spiralVaseMode,0
; firstLayerHeightPercentage,250
; firstLayerWidthPercentage,110
; firstLayerUnderspeed,0.6
; useRaft,0
; raftExtruder,0
; raftTopLayers,3
; raftBaseLayers,2
; raftOffset,3
; raftSeparationDistance,0.14
; raftTopInfill,100
; aboveRaftSpeedMultiplier,0.3
; useSkirt,1
; skirtExtruder,1
; skirtLayers,4

; skirtOutlines,0
; skirtOffset,0
; usePrimePillar,0
; primePillarExtruder,999
; primePillarWidth,12
; primePillarLocation,7
; primePillarSpeedMultiplier,1
; useOozeShield,0
; oozeShieldExtruder,999
; oozeShieldOffset,2
; oozeShieldOutlines,1
; oozeShieldSidewallShape,1
; oozeShieldSidewallAngle,30
; oozeShieldSpeedMultiplier,1
; infillExtruder,1
; internalInfillPattern,Rectilinear
; externalInfillPattern,Rectilinear
; infillPercentage,100
; outlineOverlapPercentage,50
; infillExtrusionWidthPercentage,150
; minInfillLength,0
; infillLayerInterval,1
; internalInfillAngles,45,-45
; overlapInternalInfillAngles,0
; externalInfillAngles,90
; generateSupport,1
; supportExtruder,1
; supportInfillPercentage,40
; supportExtraInflation,0
; supportBaseLayers,0
; denseSupportExtruder,1
; denseSupportLayers,0
; denseSupportInfillPercentage,90
; supportLayerInterval,1
; supportHorizontalPartOffset,0.5
; supportUpperSeparationLayers,1
; supportLowerSeparationLayers,1
; supportType,0
; supportGridSpacing,1
; maxOverhangAngle,80
; supportAngles,0
; temperatureName,Heated Bed,right extruder
; temperatureNumber,0,1
; temperatureSetpointCount,1,1
; temperatureSetpointLayers,1,1
; temperatureSetpointTemperatures,80,225
; temperatureStabilizeAtStartup,0,1

; temperatureHeatedBed,1,0
; temperatureRelayBetweenLayers,0,0
; temperatureRelayBetweenLoops,0,0
; fanLayers,1,2
; fanSpeeds,0,80
; blipFanToFullPower,0
; adjustSpeedForCooling,1
; minSpeedLayerTime,20
; minCoolingSpeedSlowdown,50
; increaseFanForCooling,0
; minFanLayerTime,45
; maxCoolingFanSpeed,100
; increaseFanForBridging,0
; bridgingFanSpeed,100
; use5D,1
; relativeEdistances,0
; allowEaxisZeroing,1
; independentExtruderAxes,0
; includeM10123,0
; stickySupport,1
; applyToolheadOffsets,0
; gcodeXoffset,0
; gcodeYoffset,0
; gcodeZoffset,-0.05
; overrideMachineDefinition,1
; machineTypeOverride,0
; strokeXoverride,330
; strokeYoverride,310
; strokeZoverride,305
; originOffsetXoverride,0
; originOffsetYoverride,0
; originOffsetZoverride,0
; homeXdirOverride,-1
; homeYdirOverride,1
; homeZdirOverride,-1
; flipXoverride,1
; flipYoverride,-1
; flipZoverride,1
; toolheadOffsets,0,0—0,0—0,0—0,0—0,0—0,0—0,0
; overrideFirmwareConfiguration,0
; firmwareTypeOverride,RepRap (Marlin/Repetier/Sprinter)
; GPXconfigOverride,r2
; baudRateOverride,115200
; overridePrinterModels,0
; printerModelsOverride
; startingGcode,G21,G90,T1,M702 H25,M705 P15 I0.0001 ,M706 B4 I120
T20 H180 K255 J255,M703,M104 S0,T0,M104 S0,M140 S0,T1,G28,G1 Z5 F200,M140 S[bed0_temperature],T1,M104

S150,M190 S[bed0_temperature],M109 S[extruder1_temperature],G28,G1 Z1 F1000,G1 X75 Y-25 F8000,G1 X18,T1,G92

E0,G1 E20 F100,G92 E0,M760 t5,G1 X10 F10000,G1 Y-2 F10000,G1 X14 F10000,G1 Y-12 F10000,G1 X18 F10000,G1 Y-2

F10000,G1 X22 F10000,G1 Y-12 F10000,G1 X26 F10000,G1 Y-2 F10000

; layerChangeGcode,

; retractionGcode,

; toolChangeGcode,

; endingGcode,T0,M104 S0,T1,M104 S0,M140 S0,G92 Z10,G1 Z15,G1 Y30 F8000,G1 X75,G1 Y-25 F8000,G1

X18,M714,M760 t10,G1 X10 F10000,G1 Y-2 F10000,G1 X14 F10000,G1 Y-12 F10000,G1 X18 F10000,G1 Y-2 F10000,G1 X22

F10000,G1 Y-12 F10000,G1 X26 F10000,G1 Y-2 F10000,G28 Y0,G28 X0,M704,M702 H60,M705 P1 I0.01,M706 B0 I120 H120

T50 K255 J125,M84,M717

; exportFileFormat,gcode

; celebration,0

; celebrationSong,Random Song

; postProcessing,

; defaultSpeed,3600

; outlineUnderspeed,0.5

; solidInfillUnderspeed,1

; supportUnderspeed,1

; rapidXYspeed,9000

; rapidZspeed,1000

; minBridgingArea,50

; bridgingExtraInflation,0

; bridgingExtrusionMultiplier,1.1

; bridgingSpeedMultiplier,1

; useFixedBridgingAngle,0

; fixedBridgingAngle,0

; applyBridgingToPerimeters,0

; filamentDiameters,1.75—1.75—1.75—1.75—1.75—1.75

; filamentPricesPerKg,29.95—29.95—29.95—29.95—29.95—29.95

; filamentDensities,1.25—1.25—1.25—1.25—1.25—1.25

; useMinPrintHeight,0

; minPrintHeight,0

; useMaxPrintHeight,0

; maxPrintHeight,0

; useDiaphragm,0

; diaphragmLayerInterval,20

; robustSlicing,1

; mergeAllIntoSolid,0

; onlyRetractWhenCrossingOutline,1

; retractBetweenLayers,1

; useRetractionMinTravel,0

; retractionMinTravel,1

; retractWhileWiping,0
; onlyWipeOutlines,0
; avoidCrossingOutline,0
; maxMovementDetourFactor,3
; toolChangeRetractionDistance,0
; toolChangeExtraRestartDistance,0
; toolChangeRetractionSpeed,600
; externalThinWallType,0
; internalThinWallType,2
; thinWallAllowedOverlapPercentage,30
; singleExtrusionMinLength,1
; singleExtrusionMinPrintingWidthPercentage,50
; singleExtrusionMaxPrintingWidthPercentage,200
; singleExtrusionEndpointExtension,0.2
; horizontalSizeCompensation,0

Appendix B

DSC measurements of candidate filament materials

This appendix shows the results obtained by the DSC. This was used to confirm information obtained in literature and to consequently decide upon which material best to use during tests. Also temperatures used during the printing process were determined based upon data obtained from these graphs. For more information on how this, and other aspects, were used to choose the appropriate materials and printing temperature settings to be used during this research the reader is referred to section 6.1.

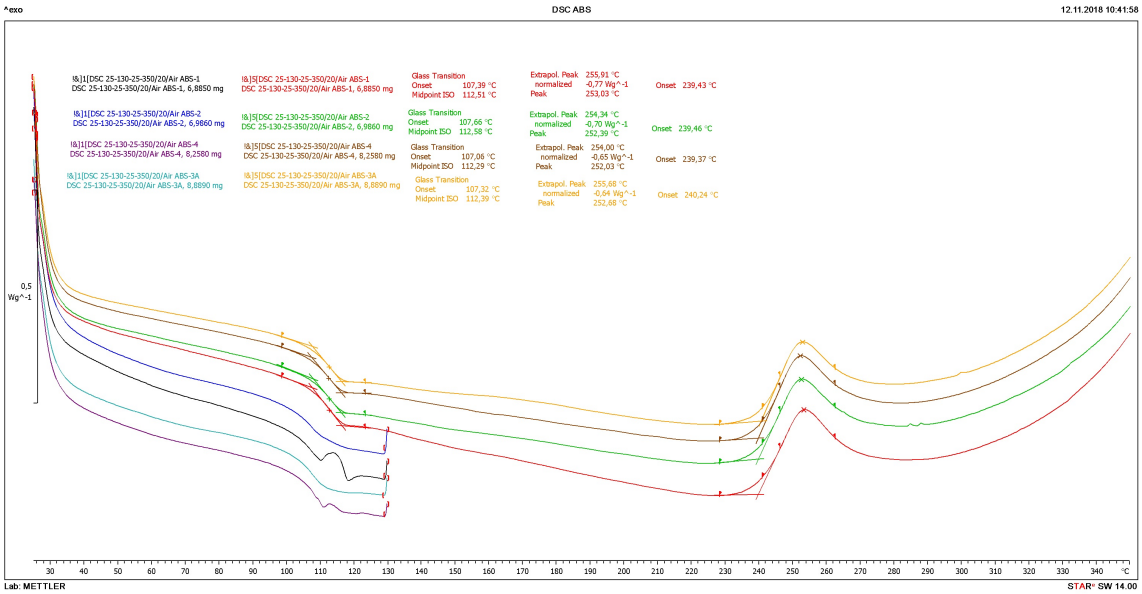

Figure B.1: DSC measurement of ABS showing T_g at $\approx 112°C$ and a presumable endothermic crystallization peak with onset at $\approx 240°C$.

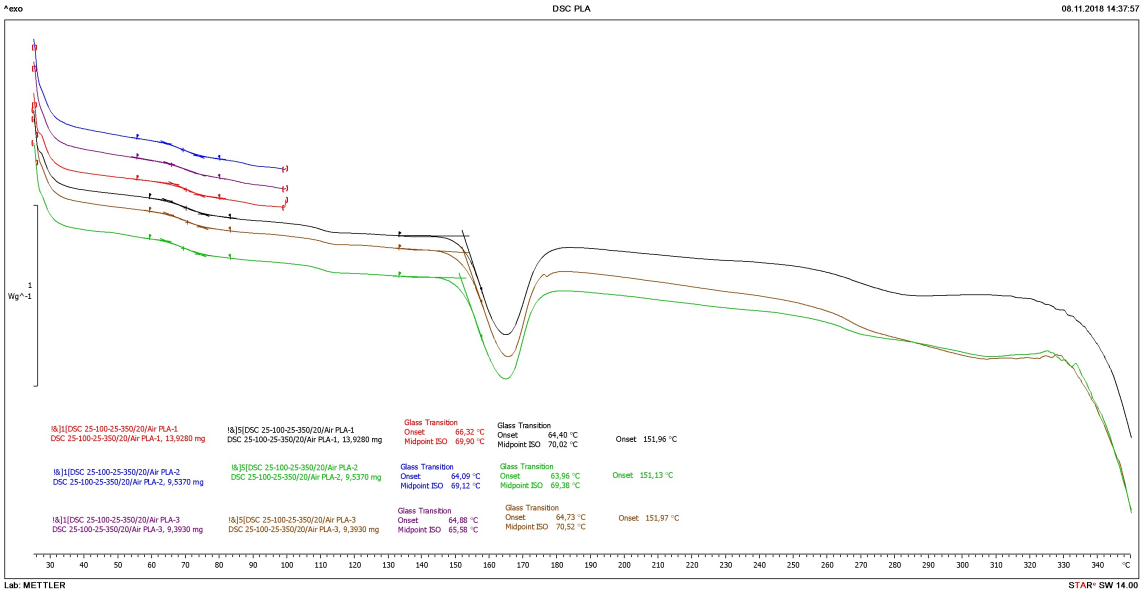

Figure B.2: DSC measurement of PLA showing T_g at $\approx 70°C$ and a exothermic well with onset at $\approx 152°C$ which indicates melting of the PLA. At temperatures above $\approx 320°C$ PLA starts to decompose which is indicated by the quickly downwards sloping curve.

Figure B.3: DSC measurement of Nylon 12 (STYX) showing T_g at $\approx 134°C$, an endothermic crystallization peak with onset at $\approx 172°C$ and exothermic melting well with onset at $\approx 230°C$.